UNIVERSITÀ DEGLI STUDI DI NAPOLI “FEDERICO II”

SCUOLA POLITECNICA E DELLE SCIENZE DI BASE

AREA DIDATTICA DI SCIENZE MATEMATICHE, FISICHE E NATURALI

Monitoring and stability of the banks of the large dams

XXXV CYCLE

TUTOR

PROF. GIACOMO RUSSO

CO-TUTOR

PROF. DIEGO DI MARTIRE

PHD CANDIDATE

RITA DE STEFANO

COORDINATOR

PROF. ROSA DI MAIO

ANNO ACCADEMICO 2022/2023

ABSTRACT

Monitoring is an essential tool for ensuring safety of large civil engineering works during their construction and service life in terms of maintenance and prevention. Large dams are critical for safety since the catastrophic human and socio-economic consequences in case of failure. Displacement measurements characterize the static response of the dam embankment and its interaction with the soil mass and are traditionally performed by means of assestimeters and inclinometers (dam body displacements) and optical precision levelling and GNSS (surface displacements). The integration of ground-based measurements with remote sensing techniques can largely improve the efficiency of monitoring systems. Among the remote sensing techniques, the Synthetic Aperture Radar Differential Interferometry (DInSAR) has been proved its versatility and efficiency for mapping and monitoring deformations of the Earth's surface (Di Martire et al., 2016, Confuorto et al., 2017), subsidence and sinkhole phenomena (Tessitore et al., 2018), as well as infrastructures (Albano et al., 2016; Infante et al., 2018). DInSAR technique can implement wide range analysis that exploits the medium and high resolutions (20m × 4 m and 3m × 3m) and short revision time (6-8 days) of the Sentinel-1 and COSMO-SkyMed constellations. Due to the availability of a large historical set of data, measured displacements on targets can reliably improve and enlarge the dataset achievable with conventional methods. In the thesis the suitability of developing an integrated monitoring system, based on the complementary use of remote sensing and traditional techniques, has been verified with reference to the case study of a rockfill dam. Menta embankment Dam is located in Southern Italy and was built between 1987 and 2000 as the main reservoir of the new aqueduct system serving the city of Reggio Calabria. The dam

was monitored from 2011 to 2022, during the experimental and operational reservoir period. Particular attention was paid to the experimental reservoir period (2011 to 2018) by performing a multi-band satellite analysis (X and C band) in ascending and descending geometry. The satellite data were compared with the inclinometric data in order to validate the technique and for a better understanding of the dam behaviour. In addition, inclinometric and satellite data were compared with the main acting cause, the reservoir level. The inclinometer data show displacements over time, consistent with the stress-strain picture of the structure of the maximum order of approximately 1.5cm, as do the satellite data. furthermore, the displacements obtained from the satellite data are consistent with the dam's reservoir and reservoir levels.

Table of contents

Chapter 1

Introduction

Throughout history, barriers were built across rivers to create water reservoirs intended for several human related activities and purposes, for example water supply, irrigation, navigation and power generation. The construction techniques have been improved, evolving from the rudimental walls made of stone bricks of the Ancient Egypt to the modern dams (Yang et al., 1999). Given the growth of the human population and the consequent needs of water and power, the socio-economic importance of these engineering structures has been increased globally in the last few decades, with apex in the 50’s and 60’s (Altinbilek, 2002; Bosshard, 2010). The issue of climate change provides also a reason for protecting water resources (Brown et al., 2009) and dams have hence had a big role in the regulation of the distribution of fresh water and in the keeping of an equilibrium while meeting the demands. In addition to the issues mentioned above, some concerns are related to the maintenance and the safety management of the infrastructures. Indeed, if from one side dams give benefits to the society, from another represent potential risk hazard to the environment and to the community if safety issues are in danger. Episodes of dam collapsing and consequent water release have already happened in the past triggered by earthquakes, erosion, aging and heavy rainfall, causing several damages downstream (Milillo et al., 2016; Roque et al., 2015). As consequence, continuous monitoring and analysis for the detection of instabilities are demanded, aiming at accurately estimating and minimizing their socio-economic risks impact. Different procedures have been practiced for the observation and prediction of dam behaviour and the monitoring of factors which might trigger failure, for instance ground water pressure, stresses within the structure and surface displacements (Stewart & Tsakiri, 1993). Deformation in turn can be due to changes of ground water levels, tectonic phenomena, and construction parameters (Emadali et al., 2017; Erol et al., 2004).

Monitoring, now of great importance in all disciplines, both technical and social, makes it possible to observe the evolution of time-varying quantities through the use of techniques and methods aimed at the constant control of processes.

The concept of monitoring, applied to large civil engineering works, has been increasingly affirming itself in recent years as a useful and essential tool for the purposes of prevention and territorial planning. The numerous 'stories' in the news increasingly confirm that the environment and structures are subject to wear and tear due to natural and anthropic causes, so the use of monitoring makes it possible to increase efficiency, guarantee safety and reduce operating costs.

The predisposition of a monitoring system allows during the entire life cycle of the work, to have documented elements that allow to know the evolution of the processes through the reading and processing of the detected parameters. For a better interpretation of the phenomena and reliability of the results, it is necessary to make use of several data sources acquired simultaneously. This results in a time series of data that gives fidelity to the technical-scientific model. The objectives underlying monitoring lie not only in understanding the phenomena, but also in adopting warning and alert systems for risk mitigation. Among existing infrastructures, dams are among the largest and most critical from a safety point of view, and for this reason they require continuous monitoring during both construction and operation (Ramondini et al., 2013).

By using an efficient control system of the dam’s behaviour, analysing all environmental and physical factors involved in the deformation process, it might be possible to ensure their stability and efficiency over time. Statistical methods and different approaches are used to analyse the correlation between the deformations of dams, made of concrete or embankment dams, and the environmental variables, such as water levels, air temperature, wind speed. Also, the instrumentations involved could be various, depending on the parameters to be monitored and the time frequency, thus the choice of suitable sensors to be involved during the monitoring process become the most important to detect the displacements of a dam, establishing the short or long term deformation process of the structure (Scaioni et al., 2018).

Despite conventional methods are usually reliable and accurate, they can provide measurements only for specific points, where special instrumentation has been placed (J. J. Sousa et al., 2016); moreover, monitoring could be time consuming and requiring field work (Roque et al., 2015).

One approach to derive structure deformation information emerging in the last three decades is related to Interferometric Synthetic Aperture Radar (InSAR) data, a form of radar system used for fine resolution mapping (Rosen et al., 2000). The sensor emits microwave radiations and it records the reflected signals; by measuring the time taken between transmission and reception of a pulse, the distance between the radar and the target can be exploited to produce an image of the ground.

The InSAR technique is very powerful for deformation monitoring but still it encounters challenges due to availability of the images, image resolution, poor quality of the results in some cases due to, for example, low signal strength (in the event of highly vegetated areas or if there are very steep slopes) and systematic errors (i.e. errors associated with faulty equipment).

This thesis work shows the reliability of the DInSAR technique for dam monitoring, validating it by comparing it with inclinometer data.

Chapter 2

Dam monitoring

2.1 Historical background on dams

A dam is a structure built across a stream or river to hold water back. Dams can be used to store water, control flooding, and generate electric energy.

The importance of dams in a community and in a country is fundamental because without dams it would not be possible to irrigate fields or supply water to urban centres, or at least it would not be possible for these activities to be carried out on a large scale and in a planned manner. Already 4000 years ago the Egyptians (but similar constructions were in Mesopotamia, China and India) built dams, both to derive water and to protect land from flooding. Historical and archaeological research confirms that the oldest dam in the world dates back to around 3000 A.D. in Jordan. The dams closed and raised the level of several small natural reservoirs serving the city of Jawa. The Jawathis Dam was 4.6 m high, 24.4 m long with a base of 4.6 m and a reservoir of over 3000 m^3. The dam was so well designed and built that the ancient structure remained standing until a few years ago, when it was partially ruined due to human intervention (Tata et al., 2016). The structure of the embankment consisted of two drystone walls with earth mixed and loose stones in between. The earth was entrusted with the sealing function. The dam was held downstream by an embankment with a moderate slope. A small permeable embankment was then built at the upstream foot to facilitate the drainage of the dam during the emptying of the reservoir. The first large dam in history was built in Egypt between 2700 and 2600 BC and is represented by the Sadd el-Kafara Dam, which dammed a normally dry watercourse, except in the rainy season, and formed a reservoir of about 570,000m3. Its length at the crest was 107 metres, height about 14 metres, thickness 98 metres at the base and 56 metres at the top (Schnitter, 1994). The body of the dam consisted of a core of rubble, river stones and earth, contained upstream and downstream by two boulder cliffs. Shortly after construction, the central part of the dam collapsed due to overflowing of the crest and rapid erosion of the embankment by water. The presence of the surface outlet remains undisputed. (https://dgdighe.mit.gov.it/)

Over the course of the years, the construction of dams in various parts of the world increased, and subsequently so did their failures, mainly due to the lack or closure of a bottom outlet (South Fork dam in Pennsylvania, ASCE 1891) or to faulty design with regard to the calculation of buoyancy and water stress. In fact, one of the problems that was sometimes underestimated was the seepage in the dam, foundations and abutments that added to the water thrust led to the collapse of the dam. This is the case of the Alcantarilla dam, built by the Romans in the 1st-2nd century A.D. in Spain, whose upstream overturning is due to the upstream face not being able to withstand the water thrust (Arenillas Parra 2002).

2.2 Classification of the dam

In the phase of planning the dam construction, the selection of its type depends on several factors, including the topography, the geology and the hydrological characteristics of the selected site, the socio-economic impacts of the project and the availability of the materials (U.S. Bureau Of Reclamation, 1987). In addition, the environmental conditions for a dam must be considered, mainly represented by the geometric and geological characteristics of the narrows destined to house it and the availability of materials with which to build it, as well as economic and social factors.

The Ministerial Decree of 26 June 2014 “'Technical standards for the design and construction of dams ", classifies dams as follows:

- Concrete dams: sealing is generally ensured by the dam body itself or in other cases by special devices on the upstream face. They can be divided according to their static behaviour: their particular curved shape allows them to oppose thrust thanks to the arch effect, discharging hydrostatic pressure onto the banks of the sides embedded in the rock of the valley to be dammed. They are slimmer and are formed of segments blocked by joints. These dams can be: arch, gravity arch and dome.

- Loose material dams: these are dams built by means of an embankment made of material obtained from natural deposits or by breaking down rock formations of different granulometry that have been suitably compacted. Sealing is ensured either by an internal core of materials with suitable permeability characteristics or by waterproofing membranes placed on the upstream face. They are subdivided according to the type of construction, the type of material used, and the type of waterproofing. According to the classification by construction materials, dams can be divided in concrete dams, made of mass concrete, and embankment dams, constructed of earth and/or rock fill (Mays, 2010).

Rockfill dams are characterised by rock blocks of maximum 0.5-1m, dense and resistant. The embankment must be permeable even after compaction.

On the other hand, clay, sandy clay, silty sand, grit with well-graded mixes are used for earth dam. In this case, the embankment must be impermeable with more than 15% of the 0.0075mm passing.

The dam body must provide two main functions to be carried out by the same or separate elements. In detail, they must guarantee:

- stability with respect to water buoyancy

- impermeability

For rockfill dams, impermeability is always assigned to a separate element from the embankment, which is permeable and can be built upstream or in the rock embankment body.

For earthfill dams, the embankment must guarantee both stability and impermeability through a single material (homogeneous dam) or with different materials (zoned dam) that guarantee the two different functions.

Law no. 584 of 21st October 1994 classifies dams into two categories, large and small, in relation to height and reservoir volume. Large dams are dams with a height of more than 15m and a volume of more than 1,000,000m^3 and are the responsibility of the state. Small dams, on the other hand, are characterised by a height of less than or equal to 15m and a reservoir volume of less than or equal to 1,000,000m^3, and their management is entrusted to the individual regions.

2.3 Dam issues: risk and safety

The number of all dams in the world has exceeded 800,000 dams in 2007, out of this about 40,000 were large dams (International Rivers Organization (2020). Damming Statistics). The register of the International Commission on Large Dams (ICOLD) indicates today a dramatic increase within the past seventy years to about 60,000 large dams, Figure 2.1 (Deutsches Talsperren Komitee, 2020).

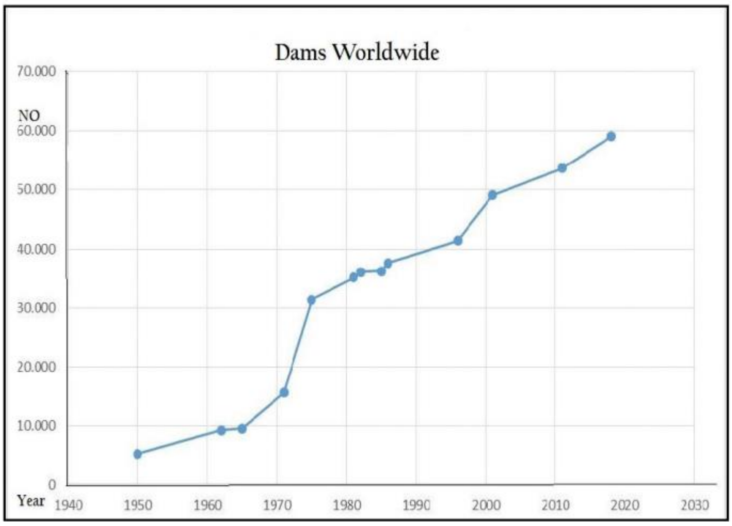

Figure 2.1: growth of number of dams in the world 1950-2020 (Deutsches Talsperren Komitee,2020)

The great number of dams already built in the world today and the ones that will be built in the future have been the subject of particular emphasis on the issue of dam safety and risks (Nasrat et al., 2020). Italy is a country with an ancient tradition in the construction of water dams, starting in the late 1800s two periods of intense construction can be identified, between 1920-1935 and 1950-1970. According to data from the Istituto Superiore per la Protezione e la Ricerca Ambientale (ISPRA https.isprambiente.it/), the total number of large dams in Italy in September 2019 is 531, localized as shown in Figure 2.2a, while about 3660 of small dams. About 60 % of the use of dams is for hydroelectric power generation, the remainder for irrigation, drinking water use, lamination and other purposes (Fig. 2.2b).

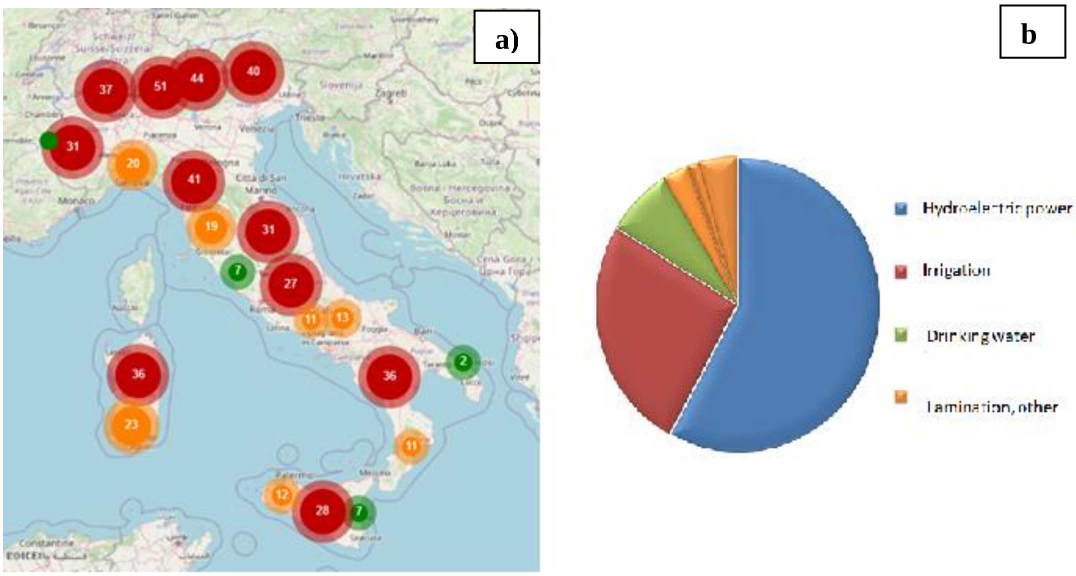

Figure 2.2: a) Distribution of large dams in Italy (https://dgdighe.mit.gov.it/); b) Main uses of large dams in Italy.

Italy is a country characterised by high seismicity and hydrogeological risk, therefore ISPRA has identified the artificial reservoirs, in a state of operation, that fall in seismic areas in relation to the seismic classification. (Prime Ministerial Decree no. 3274 of 20 March 2003) (Fig. 2.3). Approximately 6.4% of the large dams and 8% of the small dams fall within seismic zone 1, i.e. the highest hazard, affecting the regions of Friuli-Venezia Giulia, Marche, Lazio Abruzzo and Calabria.

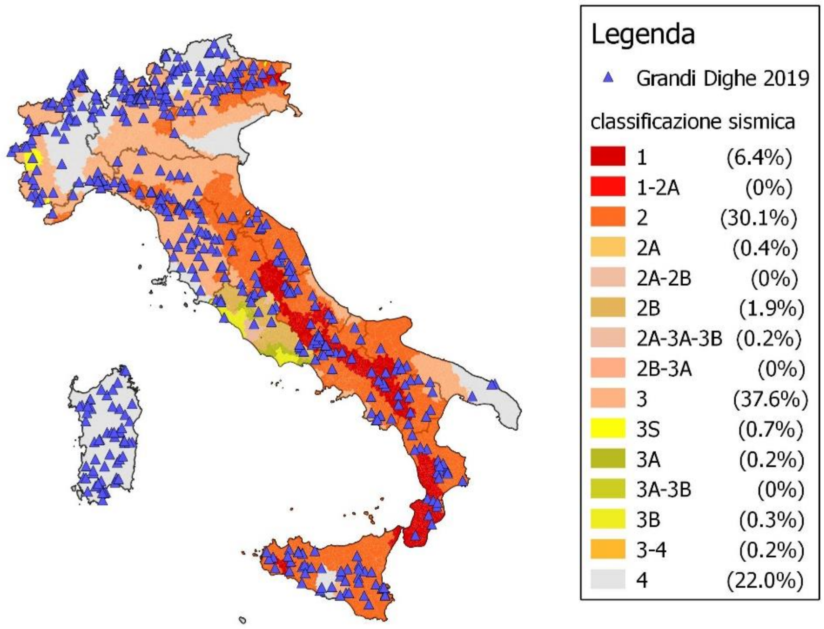

Figure 2.3: Distribution of large dams in relation to Italian seismic areas

The safety of dams is a topic of special attention in the world community, as many times it has been compromised due to insufficient hydrogeological data, poor spillway design, misinterpretation of the seismic conditions in the area, an increase in population with consequent land use in the areas downstream of the dams, and finally poor management.

The failure of a dam and the risks involved could assume the dimensions of a national catastrophe.

In summary, the objectives of all this, according to ICOLD, are as follows:

- ✓ Control the release of harmful discharges downstream of the dam,
- ✓ Limit the likelihood of events that could lead to loss of control of the stored volume and spillway. and other discharges,
- ✓ Mitigate, through on-site incident management and/or emergency planning, the consequences of such events if emergency the consequences of such events, should they occur (Bowels et al., 2007).

These fundamental objectives and principles of dam safety and risk mitigation for dam safety must be applied to all dams and associated reservoirs throughout their life cycle, both during the construction phase and throughout their life cycle, both during the planning, design and construction phase and during commissioning and operation, with the aim of minimising loss or damage downstream in the event of an accident or uncontrolled failure.

In fact, the control system, both during construction and operation, must ensure that the structure behaves according to the design specifications. As long as this occurs, the work has the degree of safety defined by the designer and approved by the competent supervisory bodies at the time of design. If, during construction or operation, a significant deviation from the behaviour predicted at the time of design appears, it is the task of the control system to highlight the phenomenon and correlate it with all the quantities that may influence the behaviour of the dam.

2.4 Dam monitoring

Embankment dams are exposed to internal and external stresses that can produce deformations that could lead to further deterioration and eventually failure (Emadali et al., 2017). It is therefore important to analyse the behaviour of the dam in order to detect early warning signs of impending failure by establishing a monitoring plan (Michalis et al., 2016), thereby carrying out a dam safety assessment and improving design procedures for both existing and future dams (Mizuno & Hirose, 2009). Conventional control measurements can differ according to the type of dam and the parameters required (e.g. displacement, leakage, pore water pressure and seepage flows) (Milillo, et al., 2016; Stewart & Tsakiri, 1993). Control surveys must be designed to determine the number and density of monitored points and the frequency of measurements (Szostak-Chrzanowski & Massiéra, 2006). Usually, information is collected at individual points and then a network is created to represent conditions over larger areas (Johansson & Watley, 2005).

Dams could be deformed by vertical subsidence due to weight of the structure and also horizontal movements, perpendicular to the centerline of the dam, due to the hydrostatic pressure cause by the water (Wang et al., 2011; Gökalp & Taşçı, 2009). Deformation could be also associated with settlements provoked by internal erosion, a process which happens when soil particles from the body of the dam are being detached and carried away by the seepage (Sjödahl, 2006). Vertical and horizontal displacements are considered by International Commission of Large Dams (ICOLD) among the most critical parameters to be measured during construction, reservoir filling and after the first impoundment, and are one of the fundamental indicators of dam deterioration (ICOLD, 1989). Several factors are involved in the deformation, such as for example the water load and pressure, construction settings, temperature changes and the geological characteristics at the foundation (Emadali et al., 2017) In embankment dams, deformation starts to occur during construction and it develops during the first reservoir fillings, but then the rate decreases in the long-term (Michalis et al., 2016). Intensity, rate and direction of the displacement vary in a determined point of the crest or the dam body during the several phases of the dam life, reflecting the variations of stresses due to differential settlements in the dam (Szostak-Chrzanowski & Massiéra, 2006).
Therefore, the behaviour of a dam must be monitored consider two important variables:
- cause or environmental quantities (which with their variations induce changes in the structure);
- effect quantities (which are the structure's response to variations in the cause quantities).

The main cause quantities acting on the structure are:
- water level reservoir;
- air, water and concrete temperature;
- precipitation (rain and snow);

- atmospheric conditions (humidity, pressure, wind);
- ice thickness;
- basin bathymetry;
- seismic events;
- flood discharge;
- independent foundation and bank movements.

While the main effect quantities are:

- internal stresses and strains;
- local deformations;
- horizontal and vertical displacements (absolute and relative);
- rotations;
- joint and crack movements;
- leaks and their turbidity;
- underpressures and interstitial pressures;
- changes in the physical-mechanical characteristics of materials.

Both quantities, cause and effect, undergo continuous variations over time and must be measured in order to assess their mutual correlations associated with the response modes of the structure. Since these measurements must be systematically repeated a large number of times during the life of the structure, the only feasible solution is to equip the structure with permanent monitoring systems. Monitoring models usually consider environmental variables as independent variables and effect variables as dependent variables to establish the interactive relationship between the variables.

The purpose of dam safety monitoring is to analyse these trends and variations and determine whether they are normal or not. (Li et al., 2019).

The research on the methods of dam monitoring data analysis is important for real-time monitoring and intelligent monitoring and is of great significance for manteinance operations of dams (Pereira et al., 2018). Predicting the variation of effect variables is often done by establishing a monitoring model. According to different theories and methods, monitoring model can be divided into statistical models, machine learning based model, time series model, deterministic and mixed model. (Wu,2003; Salzar et al., 2015; Cheng et al., 2018).

Time-series analysis refers to a range of tasks that aim to extract meaningful knowledge from time-ordered data; the extracted knowledge can be used not only to diagnose the past behavior but also to predict the future. Widely-known examples of time-series analysis include classification, clustering, forecasting, and anomaly detection (Bonelli et al., 2003).

2.4.1 Monitoring techniques

The definition and implementation of a monitoring system depends on the type of dam and its the life cycle, as well as on the size of the dam, the capacity of the reservoir and the human risk associated with the population density downstream of the structure. A monitoring system for a dam and its foundation consists of the use of several instruments and equipment to measure physical quantities and in particular to define the elements that condition the safety of the dam-foundation system and the quantities that highlight safety behaviour.

Monitoring of the embankment dams may be divided into following groups:
environmental, geotechnical, geodetic, and visual inspection. The measurements of environmental effects causing the deformations and changes in the structure may be in the area of: hydrology (rainfall and snowfall), meteorology (temperatures of air and water, and external pressure), earthquake (seismic activity, natural and induced), and temperature within dam mass (Szostak-Chrzanowski, & Massiéra, 2004)

The instruments to be used for measuring the selected quantities must ensure their reliability

- the density and distribution of the instruments inside and outside the dam-foundation assembly;
- the frequency of observations.

For dams in rockfill, the observation must be extended to the embankment-foundation complex, highlighting the safety of the structure also to the following elements:

- foundation subsoil;
- contact zone between foundation subsoil and dam body;
- dam body;
- sealing structures at the level of foundation;
- impermeable cover upstream;
- impermeable core;
- masonry structures inserted in the foundation subsoil or in the dam body (burrows, drainage organs, etc.);
- drainage works and filters.

The types of measurements and the most widespread techniques for the earthdam monitoring are related to loadings and the response of the work.

Monitoring techniques can be divided into two macro areas:

- conventional
- innovative

Their individual use, but above all their integration, makes it possible to obtain a reliable and efficient monitoring system aimed at a greater understanding of the behaviour of a structure.

All installed instruments require, however, constant attention to ensure a good operativity, preventing malfunctioning and false alarms. Traditional instruments are used for checking certain areas of concern or performance aspects which generally include the following (Adamo et al., 2021):

- ✓ Seepage flows.
- ✓ Seepage water turbidity, its salt content and temperature.
- ✓ Piezometric levels.

- ✓ Water levels.
- ✓ Deformations or movements.
- ✓ Pressures.
- ✓ Loading conditions.
- ✓ Temperature variations within dams' body;
- ✓ Accelerations experienced by the dam during an earthquake.

Table 2.1 summarises the instruments to be used to assess common problems in dams.

Table 2.1. Conventional instruments to be used for dams in relation to the problem (Adamo et al., 2021)

Problem/Concern	Typical Follow Up Method
Seepage or leakage	Visual observation, weirs, flowmeters, flumes, calibrated containers, observation wells, piezometers
Boils or piping	Visual observation, piezometers, weirs
Uplift pressure, pore pressure, or phreatic surface	Visual observation, porewater pressure cells, observation wells, piezometers
Drain function or adequacy	Visual observation, pressure and flow measurements, piezometers
Erosion, scour or sedimentation	Visual observation, sounding, underwater inspection, photogrammetric survey
Dissolution of foundation strata	Water Quality test
Total or surface movement (translation, rotation)	Visual observation, precise position and level surveys, plum measurements, tiltmeters
Internal movement or deformation in embankments	Settlement plates, cross- arm devices, fluid leveling devices, pneumatic settlement sensors, vibrating wire settlement sensors, mechanical and electrical sounding devices, inclinometers, extensometers, shear strips
Internal movement or deformation in concrete structures	Plumb lines, tiltmeters, inclinometers, extensometers, joint meters, calibrated tapes
Foundation or abutment movement	Visual observation, precise surveys, inclinometers, extensometers, piezometers
Poor quality rock foundation or abutment	Visual observation, pressure and flow measurements, piezometers, precise surveys, extensometers, inclinometers
Slope Stability	Visual observation, precise surveys, inclinometers, observation wells, piezometers, shear strips
Joint or crack movement	Crack meters, reference points, plaster, or grout patches
Stresses or strains	Earth pressure cells, stress meters, strain meters, over coring
Seismic loading	Accelerographs
Relaxation of post- tension anchors	Jacking tests, load cells, extensometers, fiber-optic cable
Concrete deterioration	Visual observation, loss of section surveys, laboratory, and petrographic analyses
Concrete growth	Visual observation, precise position survey, plumb measurements, tiltmeters, plumb lines, inclinometers, extensometers, joint meters, calibrated tapes, petrographic analyses
Steel deterioration	Visual observation, sonic thickness measurements, tests coupons

In strong development in the engineering field are some innovative techniques for surveying ground displacements both from satellite and from the ground that allow the analysis of the evolution of entire areas over time, not limiting measurements to a few points as is the case with conventional geotechnical or topographical techniques.

A traditional monitoring system consists of installing instruments, sensors and/or staking posts directly on the area (shallow or deep) to be investigated. In this way, point-type information on the measured quantities are obtained in order to establish strategies for maintenance .

The monitoring of a dam usually involves the installation of instruments on the dam body in order to monitor deep and superficial displacements. Displacement measurements can be of three types: - surface displacements, measured by topographic measurements -levelling and planimetry- settlements, upstream/downstream and left bank/right bank movements; these measurements need specialized aptitudes once or twice each year;

- in-depth displacements, measured by instruments which are generally installed during construction (pendulum, inclinometer, extensometer, settlements gages);

- relative displacements, along a joint or of a crack, quantified by instruments generally installed when needed (crack meter, 3D crack meter) (Bonelli et al., 2003).

The inclinometer monitors deformation normal to the axis of the casing and the depth detected for the shear movement is the depth of the failure surface. The acquisitions of the deformation are executed periodically using an inclinometric probe. Nowadays real-time transmission of measurement data to data loggers is much more widespread. (Fig. 2.4).

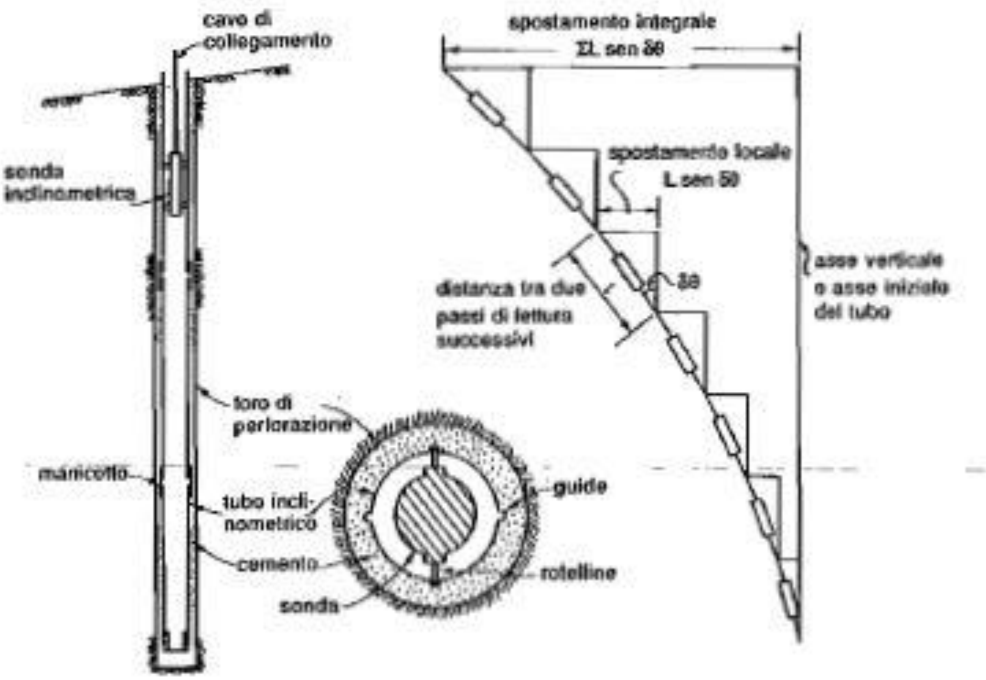

Figure 2.4: Schematic diagram of inclinometer.

Inclinometers allow horizontal displacements to be measured with high accuracy and a high degree of reliability. Measurements can be monitored with a removable probe or with a fixed probe, and in both cases it is necessary to install the inclinometers tubes in boreholes. The frequency of the measurements is conditioned by the accessibility of the pipes in particular atmospheric conditions and by the movements (both horizontal and vertical) of the ground that can damage the pipes, limiting the possibility of taking measurements. The latter limitation is overcome by the installation of fixed probes inside the pipe.

2.4.2 DInSAR dam monitoring

In this information era, the trend is of remote sensing is to use new technologies for automation of monitoring important engineering undertakings or natural hazard such as dams, reservoir water level fluctuations and landslides (Casagli et al., 2018).

Dams and reservoirs site selection may be done in various ways, but most of the traditional methods are costly and time consuming

During the last three decades, DInSAR technique has been used for structure deformation monitoring, since the monitoring is essentially remote and a direct contact with the structure is not required. The accuracy of the technique is also comparable with other traditional techniques (subcentimetre to millimetre accuracy) and the results are able to show unexpected changes in the operational life of the structure. Satellite Remote Sensing provides imaging technology for updating of available maps and information in real time frame as well as collecting data of land use. The use of this technology has been reported in the literature and some case studies are given below.

A relevant study conducted by Wang et al., 2011, involved the monitoring of the Three Gorges Dam in China, which represents the largest hydroelectric project in the world, through time series using the DInSAR technique. In particular, deformation from the 2003-2008 period was measured and analysed for the first time. The results obtained showed temporal deformations over time on the left side of the dam, mainly due to temperature variation. The data obtained with this technique confirm the behaviour obtained from previous studies using conventional techniques (Yang et al., 2002, Yan et al., 2002, Li et al., 2002). Furthermore, due to the advantage of monitoring large areas, a subsidence zone near the dam has emerged.

An interesting Spanish research project ReMoDams is dedicated to monitoring the deformation of several dams using advanced time series DInSAR techniques. One of these dams is the Arenoso Dam, located in the province of Cordoba (southern Spain) (Ruiz-Armenteros et al., 2021). This dam was monitored with Sentinel-1 SAR data from the beginning of the mission in 2014 in both ascending and descending directions until March 2019 showing that main displacement of the dam in this period is in the vertical direction with a rate of the order of -1 cm/year in the central part of the dam body due to a lack of available datasets, a comparison with geodetic data was not possible.
A comparison of the results obtained with in-situ monitoring systems and the DInSAR technique for the La Pedrera dam in Spain demonstrated the latter's ability to provide a complementary method for evaluating displacements (Tomas et al., 2013). Using a Coherent Pixel Technique (CPT), the method was able to detect both linear and non-linear components of the dam.
The same technique (CPT) was conveniently used for the Conza della Campania dam monitoring, Italy (Di Martire et al., 2014). Also, in this case, the use of existing monitoring system was useful to compare the results and validate the use of the DInSAR for precise monitoring of infrastructures and structures, especially dams. The comparison between the results obtained from extensometers located on the dam and those from DInSAR technique revealed a strong agreement. Also in this case, the largest deformations occur in the central section of the structure, because this is the mainly stressed section.
Other dams in Southern Italy were monitored using the DInSAR technique. the Campolattaro dam located in Benevento and Campotosto with the aim of validating the DInSAR results of the Sentinel-1 data wit in situ measurements to demonstrate the feasibility of integrated approaches that can improve the monitoring process of dams and surrounding areas. of dams and surrounding areas, especially in terms of the number and location of observed measurement points. In order to validate the proposed approach, the method was applied to the case study of the Campolattaro dam to the case study of the Campolattaro

dam, for which comparisons were made with in-situ measurements, acquired by means of high-precision levelling and settling.

The comparison between satellite data and in situ measurements highlights the reliability of the interferometric procedure developed, as the results reflect the general trend observed from ground-based instrument acquisitions (Ullo et al. 2019).

A study involved the analysis of C-band images, as ERS, Envisat and recently Sentinel-1 images, demonstrated the capability of these data for continuous dam deformations monitoring (Sousa et al., 2016). In this study, six dams (both made up of concrete and loose materials) have been monitored using multi-temporal DInSAR techniques (point-like and distributed). For each case study, the techniques were able to detect the deformation trend of the structures with changing number of images involved. The behaviour of the analysed dam is obviously different and depends on the materials of the dam and the loads acting on it. However, the use of X-band images allows determining high-intensity stable points (PS) on the structure highly coherent.

Chapter 3

Remote sensing

3.1 Remote sensing

Observation of the Earth from space is one of the keys to a better understanding of the Earth as a system, and so vital in achieving a comprehensive assessment of the influence of man's activities on his environment (Goldsmith & de Villiers, 1990). Various definitions have been provided since the origin of the appropriate instruments for the Earth observation; one of the most interesting and concise is by Barrett and Curtis (1976) which define Remote Sensing as "the observation of a target by a device separated from it by some distance".

Remote sensing groups together techniques that study objects or phenomena from a certain distance from them, exploiting the interaction between the electromagnetic wave sent by a sensor and the earth's surface (Campbell, 2002; Jensen, 2007). The objective is to collect quantitative and qualitative information from surfaces that are generally located far away from the observer: far away means at a distance that can vary from a few metres (proximal sensing) up to thousands of kilometres (remote sensing) as in the case of observations made by satellites.

3.1.1 Background on the origin of remote sensing

Remote sensing originated with the invention of the analogic camera. During the Second World War, aerial photography was used in land reconnaissance for bombing operations. Satellites began their development during the years of the Cold War between the United States of America and the Soviet Union with the launch of the Russian satellite Sputnik-1 in October 1957 and the American satellite Explorer 1 in January 1958. In 1964, the RADAR systems used since the 1930s for military purposes were made public and usable for civil purposes. But it was in the 1970s that satellite remote sensing began to expand: the launch of the LandSat-1 satellite in 1972 by NASA marked the beginning of the space age for Earth observation and land surveying, while SEASAT, launched in 1978 by NASA, was the first satellite with synthetic aperture radar (SAR). Currently, satellites used for Earth observation and monitoring are owned by both space agencies, such as ESA (European Space Agency) and ASI (Italian Space Agency), JERS (Japaneese Space Agency), SAOCOM (Argentinian Space Agency): ERS and ENVISAT, COSMO-SkyMed, SENTNEL-1, ALOS-PALSAR. In Italy, the COSMO-SkyMed satellite constellation, launched between 2007 and 2010, represents Italy's largest investment in space systems for Earth observation, and its construction was commissioned and financed by the ASI (Italian Space Agency) and the Ministry of Defence for both civil and military purposes.

Remote sensing sensors are devices for recording the electromagnetic energy that the surface of the observed object radiates into surrounding space.

Sensors used in remote sensing fall into two broad groups: active and passive (Figure 3.1).

Active sensors produce the energy required to illuminate the scene being imaged, in addition to recording the electromagnetic energy from surfaces. Typical active earth observation systems are radar and lidar, which send out a beam of radiation and record the return signal after it has interacted, and thus been modified, by the surface to be investigated. The most widely used active sensors are RADARs (Radio Detection and Raging), which use electromagnetic waves with wavelengths λ ranging from microwaves ($\lambda \approx 1$ mm) to radio waves ($\lambda \approx 1$ m), capable of effectively penetrating clouds and fog and capture images even at night. An electromagnetic signal is characterized by the wavelength, which is the distance from one wave crest to the next, the frequency, consisting in the number of crests in a given period of time and from a certain point, and the amplitude, equivalent to the height of each peak.

Passive sensors, on the other hand, detect electromagnetic radiation reflected or emitted by natural sources (the Sun). The Sun's reflected energy can only be measured during the day when the object is illuminated (optical system); while emitted energy, such as thermal infrared, can be measured both during the day and at night (infrared system).

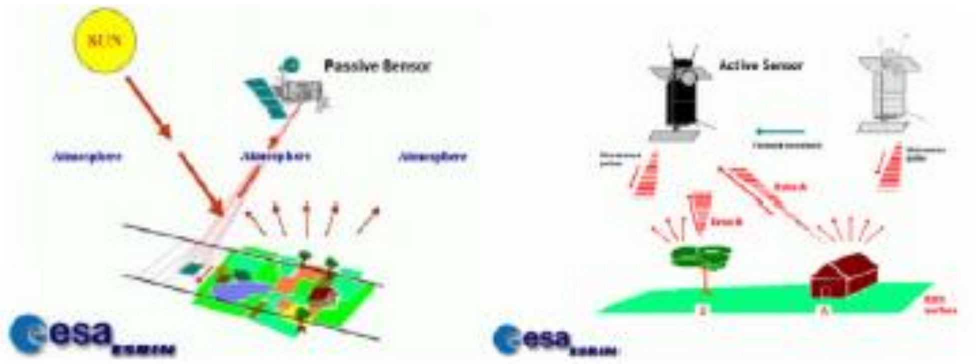

Figure 3.1: Comparison of active sensors (right) and passive sensors (left) (source: ESA).

3.2 Space platform

Space platforms are artificial satellites, orbiting the Earth at a distance of between 200 km and 36,000 km depending on the type of orbit they travel. Orbit depending on whether they acquire data by travelling from north to south (descending orbit, descending), or from south to north (ascending orbit, (descending orbit, descending), or from south to north (ascending orbit, ascending).

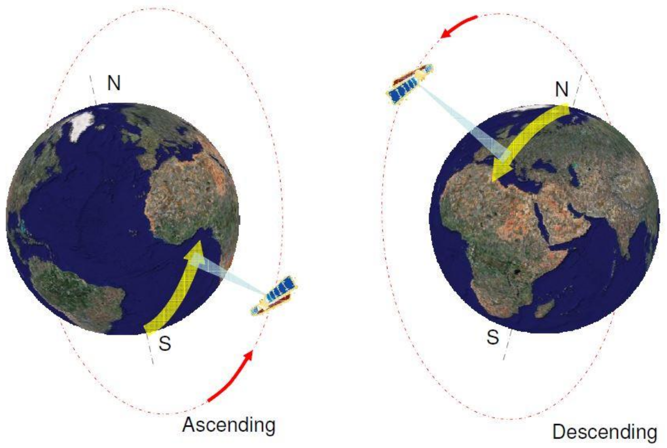

Figure 3.2: Ascending and descending acquisition modes (Tele – Rilevamento Europa, 2008).

The remote sensors can measure radiation in the visible or infrared wavelengths (700 nm – 1 mm), but also in the larger wavelengths as microwave (1 mm – 1 m) (Fig. 3.3).

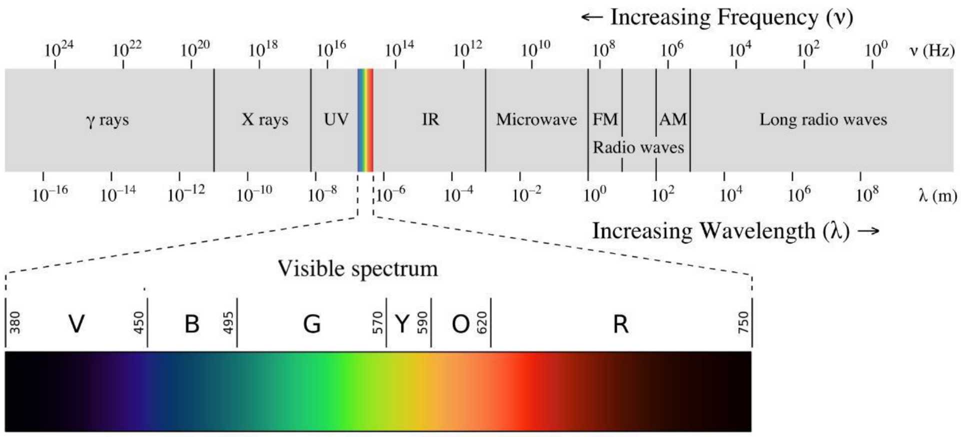

Figure 3.3. Electromagnetic spectrum with different frequencies (Hz) and wavelength (m).

Major divisions of the electromagnetic spectrum can be done on the basis of the wavelength. For remote sensing applications, every wavelength has a very important application: Ultraviolet spectrum can be useful to induce fluorescence in some materials, but it is not generally used for remote sensing. The visible spectrum is obviously significant for Earth observation, being the spectrum for optical imagery meanwhile the infrared, also used for optical sensors, in particular the infrared radiation, consists of heat or thermal energy. Microwave spectrum is the spectrum for RADAR (RAdio Detection And Ranging) applications.

Higher frequency sensors, such as C- and X-band enable higher spatial resolutions, while lower frequencies (L-Band), are less influenced by vegetation (Bamler & Hartl, 1998; Barbieri & Lichtenegger, 2005). Commonly used sensors use X-band satellites characterised by a wavelength of about 3 cm (with the COSMO-SkyMed, TerraSAR-X satellites), C-band with a wavelength of about 5.6 cm (ERS, ENVISAT and RADARSAT) and L-band with a longer wavelength of about 23.6 cm provided by the ALOS, SAOCOM and PALSAR systems (Fig. 3.4). The importance of the wavelength of the sensors lies mainly in the different resolution of the images and the interaction of the radar waves with the objects on the surface, so the choice of a wavelength to be used is a function of the characteristics of the surface of interest, for example longer wavelengths are able to interact where there is vegetation, dry soil or ice.

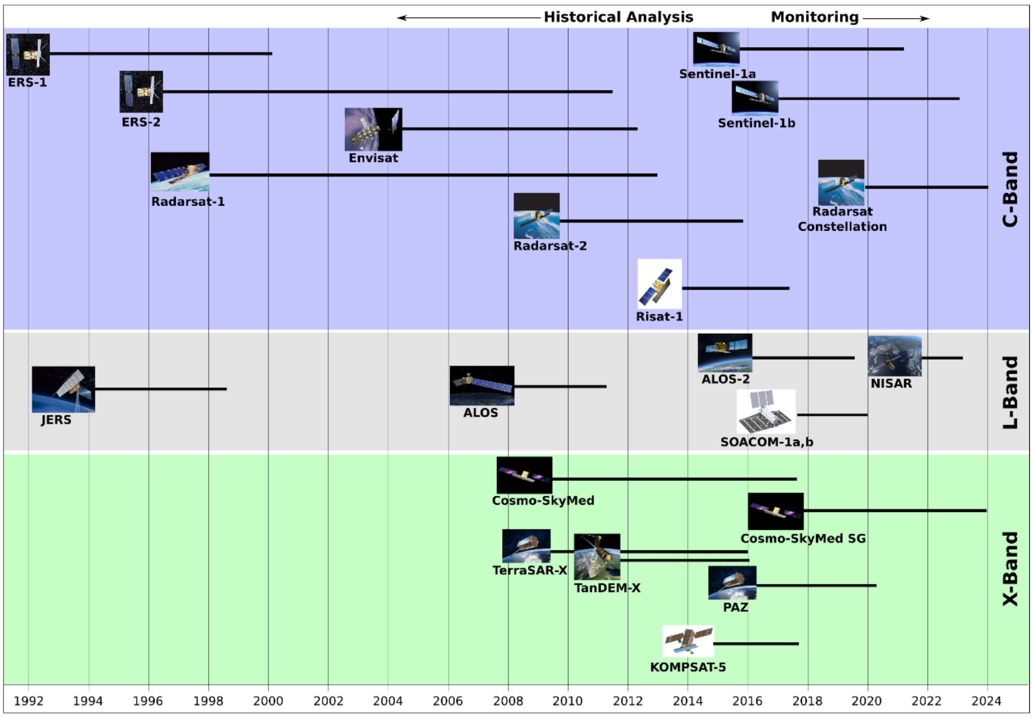

Figure 3.4. Satellites and missions categorised by band.

Many authors describe details related to spaceborne SAR missions and their applications: Schmullius et al., 1997, Musa et al., 2015, McNairn et al., 2016, Zakhvatkina et al., 2019, Baek et al., 2019, El Kamali et al., 2020, Ho Tong Minh et al., 2020. The main features of the platforms are summarised above.

C-band SAR data use the signal frequency between 4 and 8 GHz and, consequently, the wavelength varies between 7.5 and 3.75 cm respectively.

ESA's ERS (European Remote Sensing) satellites were equipped with C-band SAR radar sensors (5.3 GHz frequency, wavelength λ = 5.66 cm). Their orbits are helio-synchronous and slightly inclined to the meridians (8.5°) and illuminate, from an altitude of 785 km, a strip of land (swath) approximately

100 km wide. The direction of the sensor-target junction (LOS) is perpendicular to the orbit of the satellite and is inclined at an average angle of 23° (λ, off-nadir) to the vertical. The resolution obtained is approximately 4 metres in azimuth and 8 metres in range direction (resolution in ground range is approximately 20 m). The same nominal orbit is retraced every 35 days in a time of approximately 100 minutes.

The ERS-1 satellite acquired data from the end of 1991 to March 2000. The ERS-2 satellite, on the other hand, has been operational since the beginning of 1995 and, until the end of the ERS-1 mission, scanned the same scene but from a slightly different vantage point and one day after the passage of ERS-1. Thanks to this characteristic, ESA ensured the availability of Tandem pairs from March 1995 to March 2000, through which it was possible to generate high-resolution DEMs by exploiting the spatial baseline of the image pairs. Thanks to ESA's decision to continuously acquire data since 1992, historical datasets covering an interval of about ten years are now available for large areas, consisting of a radar image every 35 days. The Italian territory is covered by 113 ascending SAR images and 117 descending images.

Each zone has on average about 40 images acquired in ascending geometry and 70 in descending geometry.

ESA's ENVISAT (ENVIronmental SATellite) satellite, launched in November 2002, replaced and extended the functions of the ERS-1 and ERS-2 satellites. It is equipped with an Advanced Synthetic Aperture Radar sensor, which is an evolution of SAR and uses a series of antennas that can work with different polarisations and 7 different angles of incidence (between 15° and 45°) resulting in a change in the size of the scene observed in a single image. The satellite traverses a heliosynchronous orbit with a revisit time equal to that of ERS satellites (35 days), but with a delay of 30 minutes.

RADARSAT-1, on the other hand, is the Canadian Space Agency's satellite SAR mission. The instrument on board is a synthetic aperture radar with nominal characteristics slightly different from those of the ERS and ENVISAT missions. The acquisition modes are multiple, while the orbits guarantee, as in the case of the European satellites, coverage of the entire planet, according to both descending and ascending geometries. The acquisition strategy adopted by RADARSAT is 'on demand', so although the mission has been operational since 1996, the historical archives that characterise ERS data have not been created. The observation geometry is very flexible, in fact, the angles of incidence vary from approximately 10° to 60°, the radar wave beam can be oriented and the width of the image formation bands can be varied from 45 to 510 km, with resolutions ranging from 8 to 100 metres respectively. Although the orbit repetition cycle of the satellite is 24 days The RADARSAT programme is continuing with the RADARSAT-2 satellite platform launched in 2007. Such mission is characterised by higher resolution imaging, flexibility in the selection of polarisation, left and right-looking imaging options, shortened programming, processing and delivery timelines, superior data storage and more precise measurements of spacecraft position and attitude.

The most recent SAR mission started in 2014 with the program Copernicus by ESA. Sentinel-1 satellites provide all-weather condition, day and night radar imaging for land and ocean monitoring as well as glaciers extension, oil-spill monitoring, mapping of the forest, water bodies and flooding and to facilitate the land cover change detection that can be related to natural phenomena (i.e., landslides) or anthropic activities (land use, urbanization, wildfires).

As mentioned above, considering the first SAR mission launched by the European Space Agency (ESA) in 1992, 30 years of satellite images are now available for geoscientists, enabling historical analysis and monitoring of deformation phenomena on the Earth's surface.

The signal frequency used in the X-band is in the range of 8 to 12.5 GHz and, consequently, the wavelength varies between 3.75 and 2.4 cm respectively. SAR images acquired in the X-band have, in contrast to those in the L-band, greater acquisition difficulties in vegetated areas compared to C-band, due to the shorter wavelength used (2.4-3.75 cm for X-band, compared to 3.75-7.5 cm for C-band). However, systems operating in the X-band are designed to acquire images over the same area with a shorter revisit time, thus decreasing temporal decorrelation phenomena and allowing for the control of phenomena characterised by higher velocities. The shorter wavelength also allows for greater accuracy in strain estimation.

The use of a shorter wavelength accentuates the problems related to phase ambiguity, in fact, since the value of the half-wavelength relative to the X-band is smaller than that of the C-band (λ = 1.55 cm, instead of 2.83 cm), the probability that the deformations occurring in the time interval between acquisitions exceed this value is greater.

The main civil X-band SAR sensor satellites are: TERRASAR-X (DLR) and COSMO-SkyMed (ASI)

The German Aerospace Centre (DLR), in cooperation with the British National Space Centre (BNSC) and other British partners, put into orbit in June 2007 the TerraSAR-X satellite (http://www.infoterra.de/terrasar-x.html), equipped with an X-band SAR sensor, with λ= 3.1 cm and a frequency of 9.6 GHz. The sensor can work with different polarisations and has a repeat cycle of 11 days. The satellite provides high-resolution images, has the ability to vary the observation angle between 15° and 60°, and can return to the same area with a time of 2 days or less, a very useful feature for observing phenomena characterised by rapid rates of movement.

The Italian Space Agency (ASI), in collaboration with the Ministry of Defence, is carrying out the COSMO-SkyMed programme, COnstellation of small Satellites for the Mediterranean basin Observation (http://www.asi.it/it/attivita/osservazione_terra/cosmoskymed). This is a constellation of four Earth observation satellites for civil and military applications. Each of the four satellites will be equipped with X-band SAR sensors and 16-day repeat cycles. The main goal of the COSMO-SkyMed programme is to provide high-resolution images (3x3m) for natural hazards

monitoring and environmental management thanks also to dual-pol sensors mounted on satellites.
Finally, L-band sensors, which have been used since January 2006 thanks to the ALOS (Advanced Land Observation Satellite) satellites of the Japanese Aerospace Agency, have the advantage of monitoring and obtaining precise, high-resolution information even in areas without natural reflectors, which is a fundamental aspect of data acquisition with C- and X-band sensors. Numerous scientific studies, in fact, have dimostrated the high reliability of L-band sensors for mapping and moving sea ice, for monitoring in areas rich in vegetation, volcanoes, etc., such contexts necessarily require higher quality. In addition, data obtained from L-band satellites are not affected by atmospheric conditions and there is no loss of temporal coherence, as can be seen in images obtained from other SAR sensors where sometimes poor coherence affects the quality of the data. L-band sensors are characterised by a longer wavelength of around 23.6cm provided by the ALOS, SAOCOM and PALSAR systems. The limitation in the use of such L-band sensors is due to the orbit revisit times, which occur approximately every 46 days, compared to the considerably shorter times of other sensors (6-8 days). In addition, the reduced number of descending phase data available since 2006 provides a far smaller archive of images than the other C-band and X-band satellites.

3.3 Synthethic Aperture Radar (SAR)

Since the beginning of its application, SAR demonstrated to be a valuable tool to acquire information about the physical properties of the Earth surface, and to have a large range of applications, over land, ice and sea surfaces. Synthetic Aperture Radar (SAR) is a microwave imaging system, which sensors consist of an antenna, mounted on a moving platform, airborne or satellite device, which transmits a radiation reflected by the target and acquired again. The azimuth direction represents the direction of travel, meanwhile the distance from the radar track represents the range direction. The range (or across track) is the measure of the "line of sight" (LoS) distance from the radar to the target; the azimuth direction (or along track) is perpendicular to range and parallel to the flight path of the antenna. The angle between the radar beam and a line perpendicular to the surface is referred to as the off-nadir, or incidence angle (θ), named also look angle, and it changes from near-range, the value at the shortest path of radar beam, to far-range, the value at the longest path of radar beam. The distance between antenna and objects on the Earth's surface is defined as slant range, the horizontal distance along the ground is called ground range (Fig. 3.5)

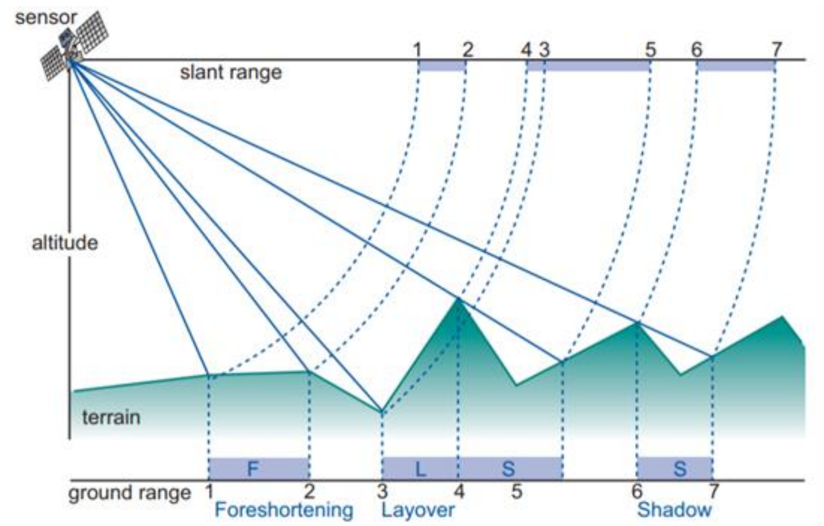

Figure 3.5. Geometric distortions in SAR imagery due to topography (Tempfli et al., 2009).

The acquisition mode, not perpendicular to the ground but according to a view angle θ, described above, gives rise in the focused images to perspective deformations due to the topography of the ground (Fig. 3.5).

Depending on the slope of the terrain, three different types can be distinguished: *foreshortening:* this occurs when the slope of the terrain tends to be perpendicular to the sensor-target junction (positive slope equal to the off-nadir angle θ); in these cases, the contribution of several points is concentrated in a few cells, producing very bright pixels in the amplitude image

layover: occurs when the slope of the terrain is greater than the angle θ; this produces a strong distortion of the image that prevents the correct interpretation of the signal and any quantitative analysis;
shadowing: occurs when some areas cannot be illuminated by the radar pulse because they are shadowed by other objects, thus producing very dark (shadowed) areas in the amplitude images.

3.4 Interferometric SAR (InSAR)

SAR Interferometry (InSAR) is a technique based on the analysis of signal phase differences between two SAR images acquired over the same area at different times (Gabriel et al., 1989; Massonet et al., 1993; Feigl 1998, Ferretti et al., 2001, Berardino et al., 2002). The first application of SAR Interferometry is dated back to the 1970s, providing information about the topography of the Earth surface (Zebker and Goldstein, 1986; Prati et al., 1989).
The Interferometric Synthetic Aperture Radar (InSAR – Gabriel et al., 1989) is a method largely used to study deformations caused by earthquakes, volcanic eruptions, glacier movements, landslides, and subsidence to a precision of a few centimeters or less (Massonnet et al.,1998; Franceschetti et al., 1999; Bürgmann et al., 2000; Madsen et al., 2000; Sansosti et al., 2006; Bozzano et al., 2011; Carlà et al., 2019; Meng et al., 2020).

Radar images are matrices of complex numbers defined by the magnitudes of *amplitude* and *phase*. The *amplitude* identifies the amount of electromagnetic field backscattered towards the satellite, while the *phase* depends on several factors, including the sensor-target distance.
The *phase* constitutes the key information for interferometric applications aimed at identifying areas subject to surface motion phenomena.
The phase values are the basic information for all interferometric techniques, summarised in the following equation:

$$\Phi = \psi + \frac{4\pi}{\lambda} r + \alpha + n$$

Where ψ represents the target reflectivity, λ is the radar wavelength used, α is the atmospheric factor, r is the distance between the sensor and the target, n is the noise due to Earth's curvature, the signal-to-noise ratio (SNR) and the instrument noise.
The processed phase difference is correlated with the topography of the ground, resulting in high-resolution digital terrain elevation models (DEM) and surface deformation maps at the millimetre scale.

3.4.1 Differential interferometry SAR (DInSAR)

The conventional technique for studying SAR data is differential interferometry (DInSAR), which is based on analysing phase value variations between two distinct acquisitions in order to reveal any differences attributable to deformation phenomena, topography or atmospheric disturbances (Massonnet and Feigl, 1998, Rosen et al., 2000).

The DInSAR is the combining the phase using multi-temporal SAR images where the phase shift related to topography is removed from the interferograms and the difference between the resulting products will show surface deformation patterns that occurred between the different acquisition dates. Through the development of more advanced techniques, the deformation velocity is calculated as a weighted average computed from the single interferograms, allowing then to retrieve the mean deformation rate of the investigated area. There are three processing approaches grouped into categories: Persistent Scatterers (PS) (Ferretti et al., 2000; Costantini et al., 2000; Werner et al., 2003; Crosetto et al., 2008), Small Baselines Subset (SBAS) (Berardino et al., 2002; Mora et al., 2003; Samsonov & d'Oreye, 2012) and methods that combine PS and SBAS as SqueeSAR (Ferretti et al., 2011). The first so-called Permanent Scatterers Interferometry SAR (PSInSAR, Ferretti, et al., 2001) is one of the basic algorithms belonging to the PS category. Phase and amplitude are the main parameters exploited by the PSInSAR method: amplitude gives information about the reflectivity of the target, while the phase indicates the sensor-target distance; therefore, amplitude allows to individuate PS and phase to estimate the movement of the PS. Persistent Scatterers (PS) are targets that keep stable the electromagnetic signal (hence, their reflectivity property) during the period of acquisition of the image. Usually, PSs correspond to man-made structures (i.e. buildings, dams, infrastructures, etc.) or to rocky outcrops, while vegetated areas, due to the frequent variation of their electromagnetic properties, cannot be considered as good scatterers. The PS detection is based on the amplitude dispersion, which is calculated by dividing the temporal standard deviation of the amplitude by the temporal mean of the amplitude of a certain pixel in a stack of SAR images. The concept is that a pixel characterized by a high and more or less constant amplitude value is assumed to show a low phase dispersion (Ferretti et al., 2001). The result is a precise measurement of the movements along the SAR Line of Sight (LoS velocities) of each PS, concerning an assumed reference point (regard as stable), in the time interval. While the SBAS approach is an algorithm capable of retrieving temporal series of deformation exploiting interferograms characterized by small temporal and spatial baseline. This algorithm aims to limit the spatial decorrelation taking into account the spatial and the temporal information from the SAR data (Berardino et al., 2002). These interferograms are used as inputs to calculate the unwrapping stage, from which the estimation of the topographic contribution and the extraction of the Low Pass (LP) temporal deformation, which will be subtracted from the wrapped interferogram module 2π, is done. Therefore, the interferograms will be considered as residual phase and be unwrapped. Therefore, the spatial and temporal filters are applied to unwrapping the temporal deformation and the topographic phase residual. Finally, the inversion of the stack of interferograms is guaranteed using the singular value decomposition (SVD) method. The advantage of the SBAS technique is represented by the high coherence and the high spatial density of the final product, and the reduction of the errors due to the redundancy of the information (more interferograms for every image), although disadvantages are due to the high computational requests. The third approach is a hybrid methodology that uses the process PS and retrieving phase from many small targets with similar scattering, called distributed scatterers (DS).

DS is mainly over natural land covers and is affected by temporal and geometrical decorrelation. The mixed approach increases the spatial density of measurement points over areas characterized by DS, preserving the quality information obtained using the PS technique. SqueeSAR™ is the algorithm, mixed PS and DS process-based, that provides significantly increase coverage points, mainly in non-urban areas. In particular, starting to spatially average the data over statistically homogeneous areas, it is possible to increase the signal-to-noise ratio (SNR), obtain a high coherent of the point scatterers without the need to perform a time-consuming phase unwrapping procedures on hundreds of interferograms. The SqueeSAR advantages are an increase of the spatial density of valid pixels, and an achieve a larger coverage of the measurement. In addition, the mixed approach provides a high quality of the displacement time-series of the DS.

The advantages of this technique are many. Firstly, as previously reported, it allows atmospheric disturbances to be overcome. Furthermore, it allows very large areas to be studied and monitored with millimetre displacement resolution. Displacement is measured in two dimensions, vertical and horizontal, thanks to the availability of displacement data in both ascending and descending geometry. The possibility of having displacement information over a ten-year period makes it possible to define the degree of activity of phenomena with greater accuracy, which is especially useful for slow-moving phenomena. On the other hand, the disadvantages lie mainly in the absence of measurements where there is a lack of radar targets, the high revisit times of the satellites, which is a limitation for movements characterised by centimetric annual velocities, and finally the lack of information in the N-S direction.

Chapter 4

Case study: the Menta dam

This chapter is dedicated to the presentation of the case study. A brief description of the construction history and the characteristics of the dam will firstly be described. Finally, a brief summary of the operational monitoring system and the reservoir level is described.

4.1 Brief history of the dam's construction

The origin of the project dates from the 1970s when the Cassa del Mezzogiorno carried out a series of studies and analyses as part of Special Project 26, to quantify the available water resources and identify projects capable of responding to Calabria's growing water deficit, which in turn developed from the outline forecasts of the General Plan for Aqueducts approved by national law in 1963. In order to supply drinking water to the population of southern Calabria (from Scilla to Melito di Porto Salvo), the Fund for the South (Cassa per il Mezzogiorno), planned the construction of a dam and in the period 1979-1980 began to define the position and type of a dam along the 'Menta' stream, based on lithological and structural considerations. Considering the location and seismic assessment of the area, a rockfill dam with bituminous lining was chosen.

To this end, surveys were conducted to define the characteristics of the granular materials to be used for the dam body, and a quarry was identified approximately 600 metres upstream of the dam site. Several tests were carried out to confirm the conformity of the material to be used. This had a high unit weight by volume and was easily compacted with vibrating tools but had a very high degree of crushing due to the flattening of the edges caused by the elongated and rectangular shape of the grains.

Therefore, laboratory tests were carried out for the grain size distribution of the material and showed that it was suitable for the construction of the dam.

Based on the deformability and strength values determined from the tests, some limit equilibrium stability analyses were performed to assess the static and seismic safety of the embankment, taking into account the regulations of the time.

The construction of the dam body began in 1989 but, during 1992, it was observed that the materials produced by the quarry were compatible with the grain size distributions required by the project, but not in the same quantities as those required by the project. In fact, the production lacked the larger aggregates needed for the volumes of parts 4 and 5 of the dam. As a result, the finer fraction exceeded the quantity needed for the other materials. To solve these problems, the volumes of zones 4 and 5 were reduced; for the material in zone 1, the finer particle size distribution was judged to be suitable for the function of that zone (foundation for the bituminous lining), and the excess finer material from zone 1 was mixed with the material from zone 3, producing a finer particle size distribution than the design foresaw. The dam body was completed at the end of 1996, while the bituminous lining was constructed until 2000. During construction, a series of particle size and triaxial tests were performed on the bituminous lining in order to check the perfect execution of each layer. After a break of several years, backfill tests began in 2010 to 2019. From 2019 the dam goes into operation period.

4.2 Characteristic of the dam

4.2.1 Dam geometry

The embankment has a maximum height, from the foundation level of 85.75 m (at approx. 1431.75 m a.s.l.) upstream and 89.75 m downstream; the width of the crown was set at 10.00 m, therefore greater than 1/10 of the maximum height, as required by the standards. The slope of the upstream face is 1:1.8, which allows for easy laying of the bituminous layer for the entire height of the weir in question. The slope of the valley face, which also has a slope ratio of 1:1.8, is interrupted by two 3.00 m wide embankments located at 1404.50 and 1377.50 m above sea level; the average slope of the embankments in the highest section is slightly greater than 1:1.8, a value compatible with the intrinsic characteristics of the compacted material. The maximum width of the standard section at the base reaches approximately 350 m. The normal retention level was set, in relation to the volumetric requirements of the utilisation, at 1424.5 m above sea level, while the maximum flood level was set at 1426.0 m above sea level, where the overflow works are located. The height of the crest is set at 1431.75 m a.s.l., taking into account 5.00 m of net free space plus 0.75 m of half-wave in relation to the height of the dam and the width of the reservoir. In plan, the dam has a rectilinear course in the section that closes the main valley, while it has a curved-straight course at the right side saddle (Fig. 4.1).

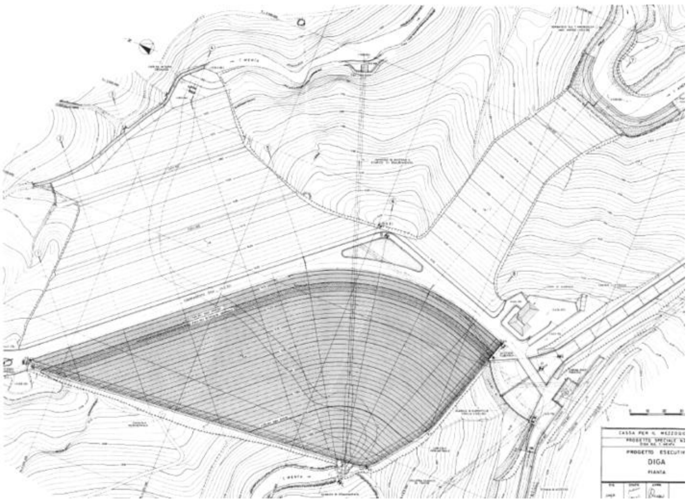

Figure 4.1: Plan of the Menta Dam.

The straight section of the main weir has a length of 325 m; that of the secondary weir is 125 m; the curved section, in the crowning section, has a radius of 179 m and an angle of approximately 59°. The upstream face is flat with a slope of 1/1.8 at the main valley and has a curved surface in the saddle area. The curved part of the face is composed of a conical surface with a constant slope and variable radius. The upstream foot of the dam is contained over its entire length by a concrete wall structure that rises along the banks to the crowning level. Inside the wall structure, for the entire development, an inspection and collection trench are incorporated for the mantle drainage; the trench is of such dimensions as to be able to carry out the waterproofing and seaming injections with the base rock and to carry out the foundation drainage. At the lowest point of the culvert, the interception devices of the exhaustion drain are housed.

In correspondence with the crowning level, the structure is joined into two head blocks in which the accesses to the perimeter tunnel are located, which can also be accessed from the outside by means of the tunnel underneath the dam and containing the exhaustion channel. (Fig. 4.2).

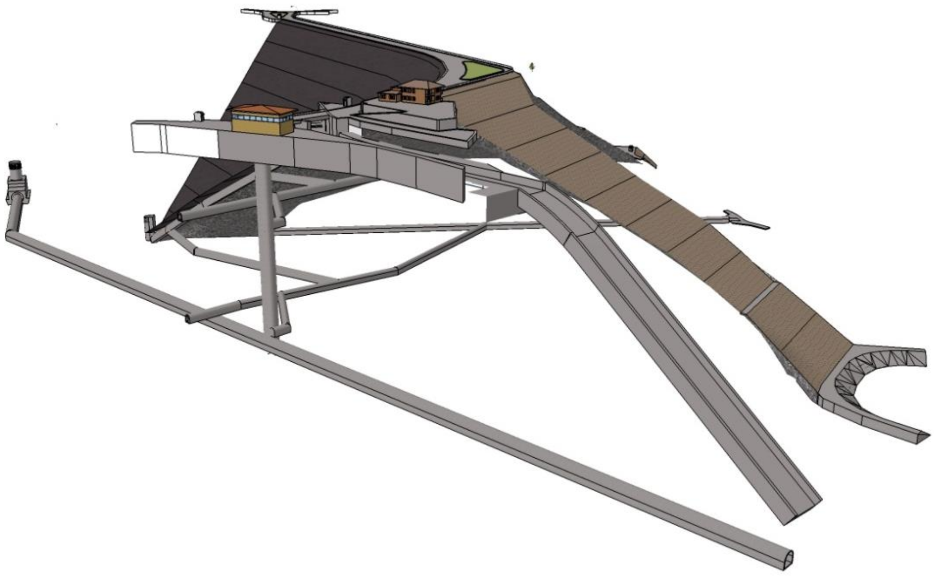

Figure 4.2: 3D model of the dam body with tunnels.

4.2.2 Dam zoning and material

The dam is built using artificially compacted loose quarry materials. The cross-section was defined on the basis of the material pieces obtained from the caving tests, the characteristics of which were determined by tests carried out on site and in the laboratory. The typical section of the embankment therefore consists of several zones as shown in Figure 4.3.

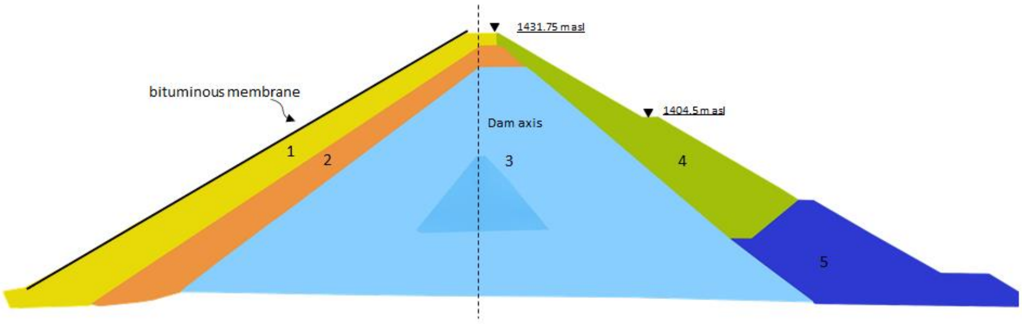

Figure 4.3: Typical section of the dam; 1) dam's supporting material and transition; 2) transition and filter material; 3) dam body; 4) protection of the downstream face; 5) embankment reef.

Five different zones can be recognised in the standard section. The grain-size characteristics of the constituent materials, as well as the paving and compaction methods, are summarised below.

Zone 1 material: Immediately below the bituminous concrete pavement, it serves as drainage and transition, in terms of grain size and permeability, between the pavement and the materials of zones 2, 3 etc., which are located further downstream. This material was obtained by crushing quarry rock, corrected with regard to grain size by the addition of sand and gravel possibly imported from coastal quarries. The maximum diameter of the crusher elements is approximately 25 mm. The fraction passing through the 5 mm screen is more than 20 per cent. The permeability coefficient is in the order of K = 1 cm/s.

Zone 2 material: it serves as a transition in grain size and permeability between the zone 1 material and the zone 3 material, which forms the dam body. This material consists of fine elements obtained by screening the quarry tout-venant. The maximum diameter of the pebbles of zone 2 material is 100 mm and the fraction passing 10 mm is at least 10%.

Zone 3 material: this is used to form the dam body, i.e. the zone with the largest cubic capacity among those envisaged. The material consists of tout-venant elements from quarries or excavations, with the exclusion of blocks larger than 500 mm, which may not be placed in the thickness of the single layer.

Zone 4 material: it serves as protection of the valley face from erosive action induced by atmospheric agents. It consists of a reef poor in fine elements with mechanically compacted material obtained from the natural segregation that occurs on the quarry face. The material consists of the fraction greater than 100 mm, which is the result of the production of Zone 3 material. As with zone 3 material, the maximum size will be approximately 500 mm.

Zone 5 material: it forms the valley foot of the dam with elements of a size that ensures the stability of the dam body. The material consists of selected rock blocks with a minimum size of approximately 300 to a maximum of 800 mm.

4.2.3 Bituminous facing

The bituminous facing placed on the upstream face of the dam is of the controlled drainage ("sandwich") type and consists of the following layers (from bottom to top) (Fig. 4.4)

- Attachment layer of bituminous emulsion in the minimum quantity of 2 kg/m^2 to ensure efficient anchorage of the blanket to the dam body;
- Bituminous conglomerate layer (binder) with a minimum thickness of 6 cm to level the upstream face and form the load-bearing element of the sealing structure;
- Bituminous conglomerate layer at least 5 cm thick with waterproofing function;

- A layer of bituminous conglomerate at least 8 cm thick with a draining function; the function of this layer is that of a draining bed, capable of conveying any filtering water to the foot through the actual waterproof covering. In order to make it possible to identify the source areas of any seepage, the draining layer will be divided into seven fields delimited by waterproof bituminous conglomerate kerbs arranged along lines of maximum slope; each field will be connected, by means of a drainage pipe, to the perimeter trench for measuring any seepage.
- Two overlapping layers of bituminous conglomerate at least 6 cm thick each, with waterproofing function;
- Surface sealing.

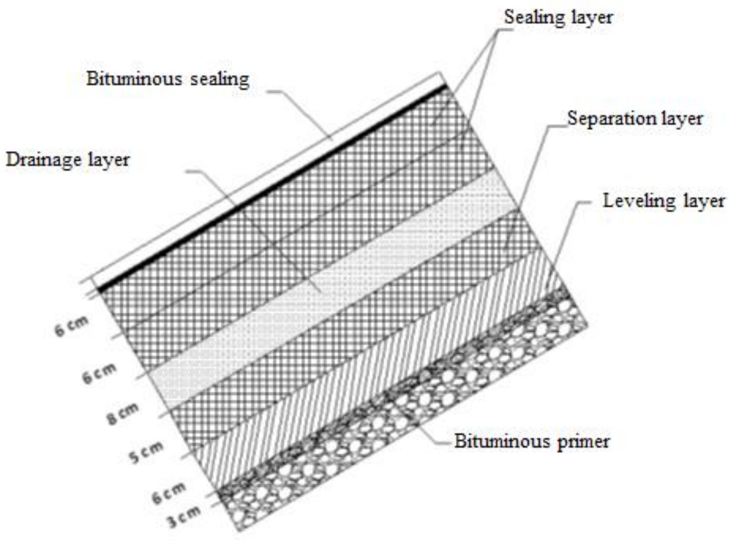

Figure 4.4: Characteristic section of the bituminous facing.

4.3 Geological setting

The Menta dam is located in the centre of Aspromonte massif, in the Roccaforte del Greco (RC) area at an altitude of about 1400 m above sea level. (Fig. 4.5).

Figure 4.5: Geographical setting of the Menta dam.

The Aspromonte massif is located in the southernmost sector of Calabria (Fig. 4.5); it rises to elevations of about 2000 m a.s.l. (1955 m a.s.l, at Montalto) in a territory which is one of the most geodynamically active sectors in the central Mediterranean area, where complex crustal deformation is occurring due to the Africa-Europe collision (Amodio-Morelli et al., 1976; Tortorici, 1982; Parise et al., 1997). The geology of Calabria is very complex and from a structural geological point of view can be divided into two main segments chain: the Calabro-Lucano Apennines to the north and the Calabrian Arc to the south. The former, in Calabria, includes the Pollino Mountains and the northern part of the Coastal Chain and consists of different tectonic units, mainly of sedimentary origin and of Mesozoic-Cenozoic age. The Calabrian Arc, in turn, is represented by the Sila, Serre, Poro and Aspromonte massifs and also includes the southern portion of the Coastal Chain (Calcaterra et al., 2010).

The Aspromonte Massif represents, together with the Peloritani Mountains belt, the southern termination of the Calabria-Peloritani Orogen (Cirrincione et al., 2015), an arcuate orogenic segment located in the Western Mediterranean area (e.g. Faccenna et al., 2001). The evolution of the Peloritanian basement (CPO) is the result of an evolution is the result of Palaeozoic orogenic processes, reworked during the Alpine and Apennine orogenic cycle. The CPO can therefore be considered today as a composite terrane consisting of basement rocks derived from a multi-stage poly-orogenic history, currently merged into several sub-terrane, formed mainly during the Variscan orogeny (Pezzino, 1982; Atzori et al., 1984; Bonardi et al., 2004; Cirrincione et al., 2015). In this scenario, the CPO can be separated into several orographic domains known as the Coastal Chain and Sila Massif in northern Calabria, the Serre and Aspromonte massifs in southern Calabria and the Peloritani Mountains in Sicily (Fig. 4.6)

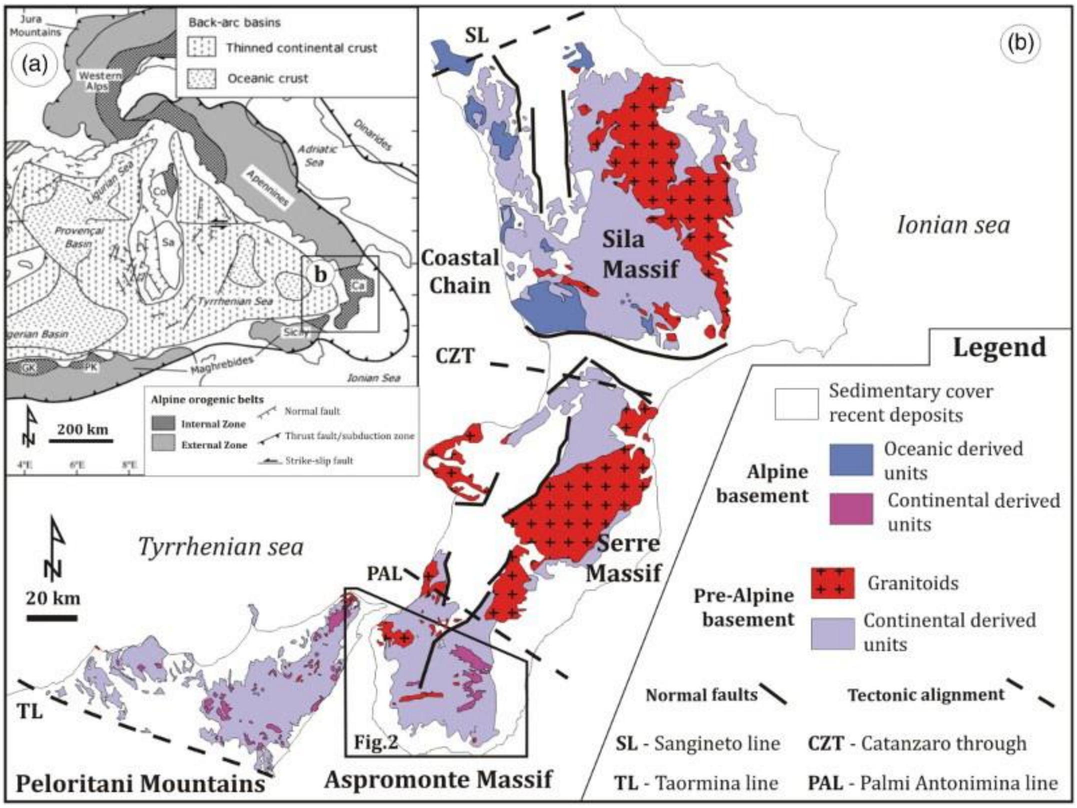

Figure 4.6: Tectonic map of Southern Italy, showing the location of the area of interest; b) geological map of the Aspromonte Massif and schematic column of the metamorphic units (Fazio et al., 2015).

In this context, the Aspromonte Massif is a nappe edifice cropping out in the southern Apennine chain, straddling the African-European plate boundary and originated during the Mesozoic-Cenozoic (Carminati et al., 1998).

During Plio-Quaternary, it has been involved in the subduction of the Ionian Sea lithosphere under the continental crust of the Ionian area and in the extensional and uplifting processes making this area one of the most seismically active of the whole Mediterranean basin (Presti et al., 2013).

Calabria-Peloritani area is composed by metamorphic and crystalline tectonic units dated back to Paleozoic era, and pre-Neocene (e.g. Atzori et al. 1994). The Aspromonte Massif region is composed by three main tectono-metamorphic units (Fazio et al. 2015, Fig. 4.7):

- the Stilo Unit (Hercynian low-greenschist to amphibolite facies metapelites);
- the Aspromonte-Peloritani Unit (Hercynian amphibolite-facies metamorphic rocks, intruded by late – Hercynian granitoid bodies, re-equilibrated during the Alpine orogenesis)
- the Madonna di Polsi Unit. (greenschist-facies metapelites - essentially garnet-micaschists and phyllites, surfacing into three main tectonic windows named ‘Polsi’, ‘Samo-Africo’, and ‘Cardeto’ from the most important localities occurring nearby).

A sedimentary clastic succession, the Stilo-Capo d’Orlando Formation (lower Miocene - Pleistocene), covers the different metamorphic units showing locally typical erosional shapes like domes and pinnacles.

During the last extensional tectonics phases, uplift of the southern Calabria region resulted in horst-graben systems formed by NE-SW normal faults combined with NW-SE trans-tensional fault system.

The Aspromonte Massif (Ortolano et al., 2013), can be interpreted as a south-east verging nappe edifice (Ortolano et al., 2015), where the two uppermost tectonic slices are composed of middle-upper crustbasement rocks (i.e. the Stilo unit - SU and Aspromonte unit - AU). These two units are characterized by a multi-stage Variscan metamorphism, locally involving only the deeper unit during the latest stages of the Alpine metamorphic cycle (Ortolano et al., 2005; Pezzino et al., 2008). The deepest tectonic unit, separated by the intermediate Aspromonte unit by a thick mylonitic horizon, formed during the Oligocene. This unit is characterized by medium grade metapelites, exclusively registered a complete Alpine metamorphic cycle, known in literature as Madonna di Polsi unit (MPU) (Pezzino et al., 1990; 2008; Ortolano et al., 2005; Cirrincione et al., 2008; Fazio et al., 2008) (Fig. 4.7)

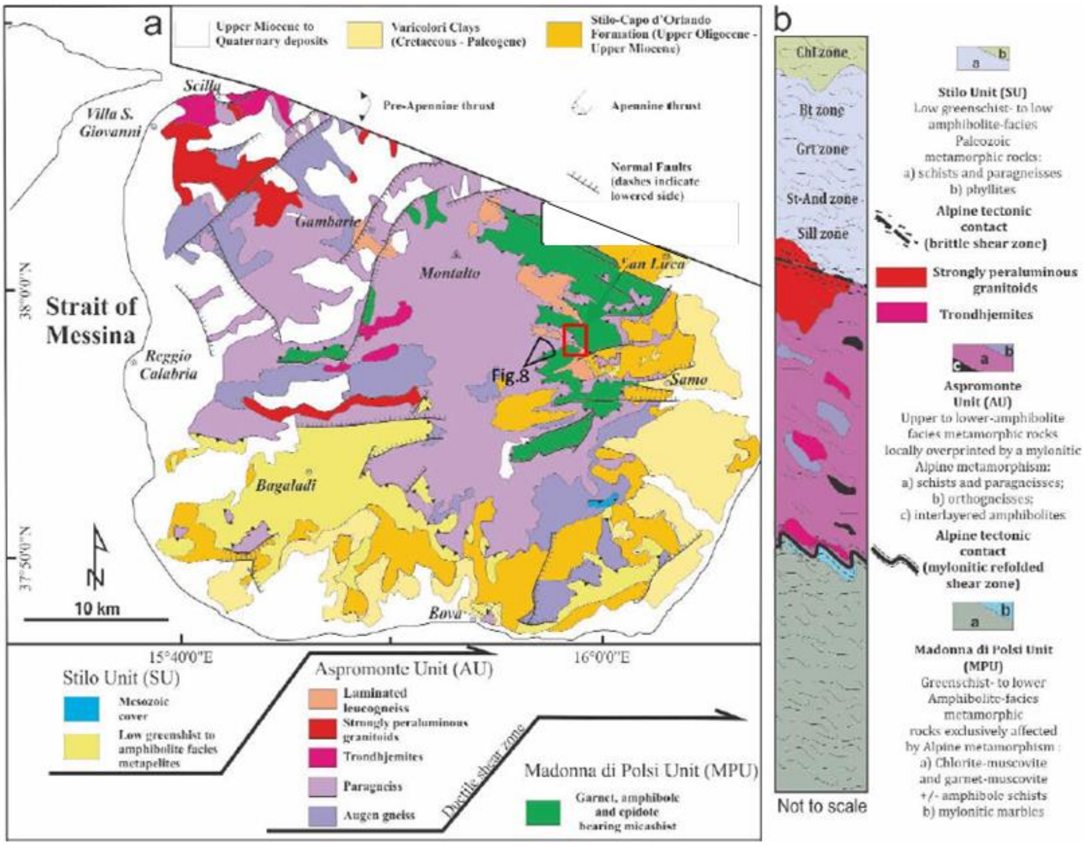

Figure 4.7: a) Geological sketch map of the Aspromonte Massif nappe-like edifice. B) schematic tectono-stratigraphic column of the tectono-metamorphic units (Ortolano et al., 2015 and Fazio et al., 2015).

4.3.1 Surface fault study

In order to gain a better understanding of the area and considering that the area falls within one of the Mediterranean's most seismically active zones, a surface faulting study was conducted with the objective of excluding active and capable faults (FAC).The three main areas investigated to characterise surface faulting are located on the right bank of the Menta Lake (Area 1) on the left bank (Area 2) and downstream of the dam (Area 3) (Fig. 4.8).

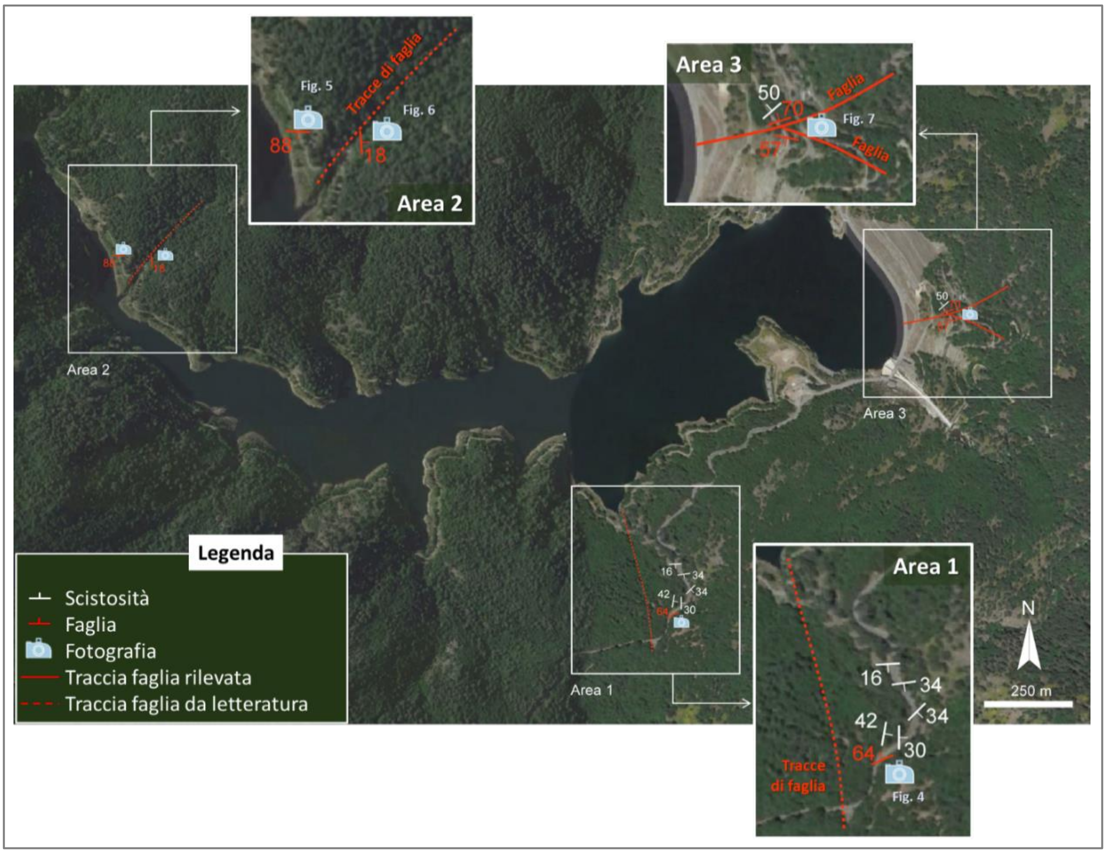

Figure 4.8: Identification of the Menta basin survey areas.

The metamorphic rocks outcropping in area 1 (Fig. 4.9) are characterised by a schistosity that changes immersion going from north to south along the road to the dam. In the northern part of the area the schistosity dips weakly towards the S, further south it dips towards the SE and, near a fault with an NNW dipping plane and a medium-high dipping angle (64°), it dips towards the E. The identified surface fault has a deformation zone of multi-meter amplitude that does not deform the vegetation cover and Quaternary debris sediments (Fig. 4.9 on the left). This zone includes two main sub-parallel slip surfaces bordering a belt of fault rocks of decimetre power, as well as numerous secondary slip surfaces branching off from the main ones (Fig. 4.9 on the right).

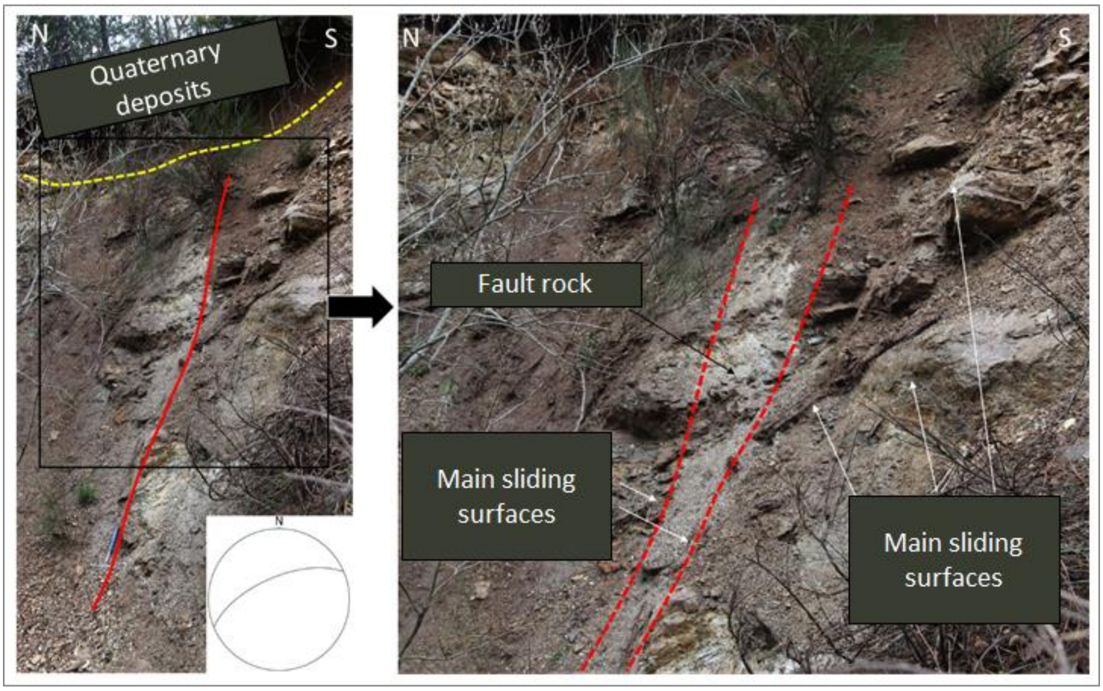

Figure 4.9: Fault identified in area 1. The lower hemisphere of the stereogram shows the projection of one of the identified fault planes.

Two surface faults were identified in Area 2 (Fig. 4.10): the first, directed about E-W and sub-vertical (dip angle of 88°) and the second, weakly dipping towards E (dip angle of 18°). In addition, the first fault is characterised by a deformation zone of metric power bordered by two faults with a lenticular band of fault rocks inside (Fig. 4.10). The bedding and roof rocks of the deformation zone are intensely fractured, while, as already observed for area 1, the faults appear to be sealed by Quaternary sediments and vegetation cover (Fig. 4.10).

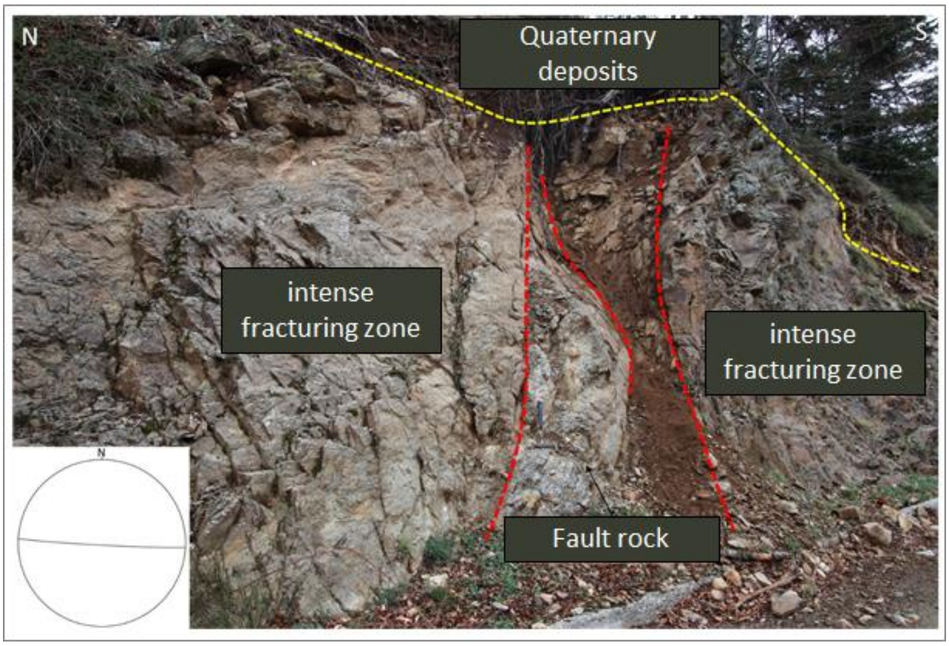

Figure 4.10: First fault identified in area 2. The lower hemisphere of the stereogram shows the projection of one of the identified fault planes.

Lastly, the second identified fault is associated with a fault plane that forks to the N, giving rise to two fault segments bordering a lens of fault rocks (Fig. 4.11).

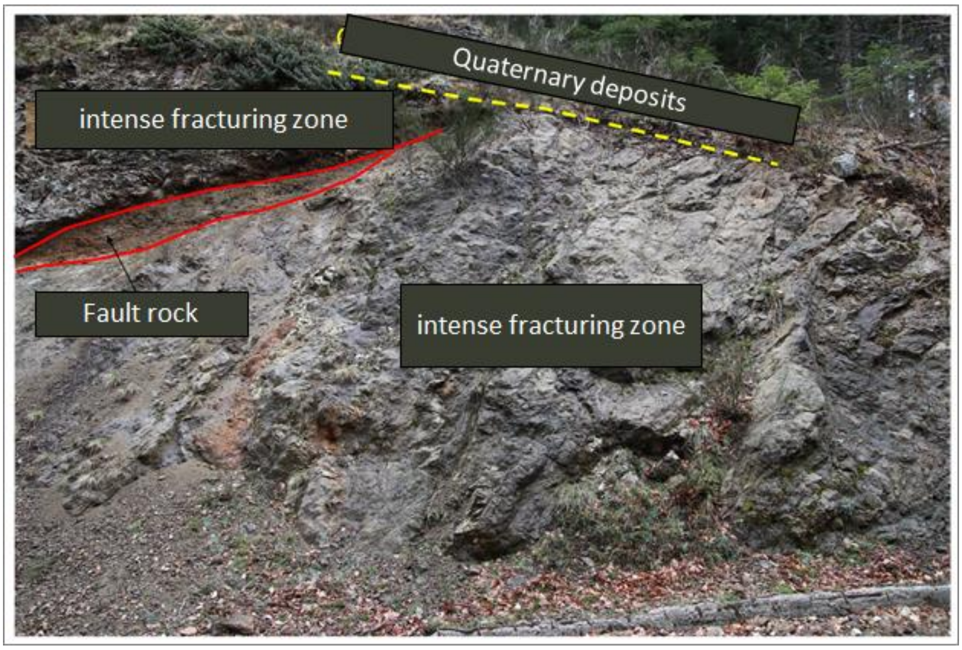

Figure 4.11: Second fault identified in area 2.

The rocks outcropping in area 3 constitute a large deformation zone characterised by two main slip surfaces plunging towards the NNW and approximately towards the SSW. The deformed zone is characterised by a plurimetrical base thickness and the convergence of the main faults in the summit part (Fig. 4.112). Along the fluttering surface bordering the S side of the deformed zone, streaks were found indicating predominantly direct movement along the dip direction (Fig. 4.13a). Despite the occurrence of these indicators, however, it was not possible to identify the direction of movement (direct or reverse). The central part of the deformed zone consists of fine-grained fault rock, which can be defined as fault gouge (Fig. 4.13b). As already observed in the previous areas, the vegetation cover and debris sediments of Quaternary age are not crossed by faults in this third area.

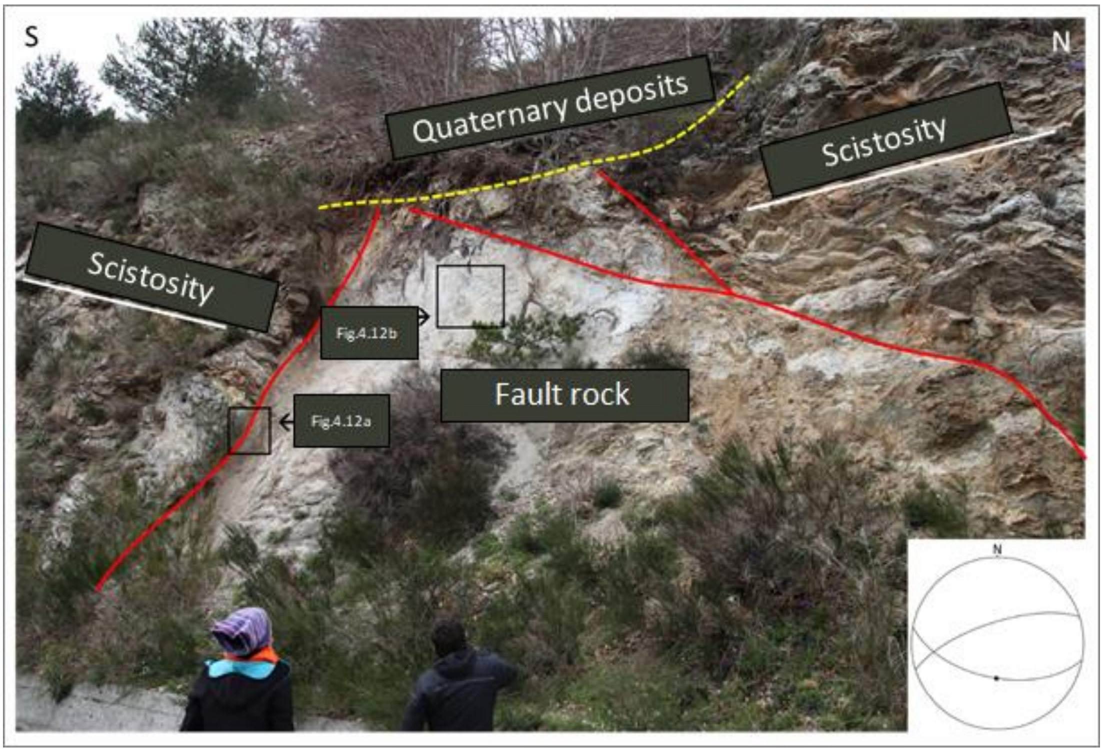

Figure 4.12: Fault zone identified in area 3. The projections of the fault planes are shown in the lower hemisphere of the stereogram.

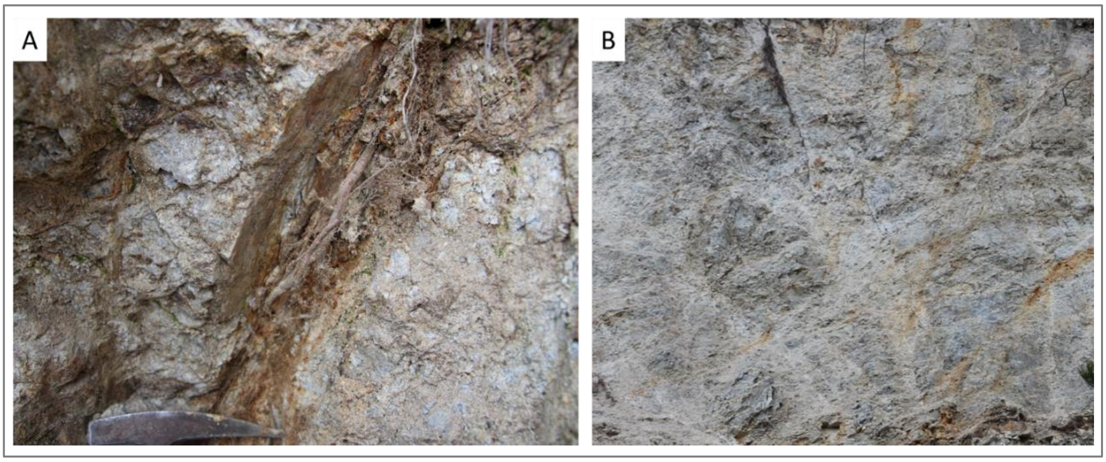

Figure 4.13: Details of the identified fault in area 3. A: slip streaks; B: fault rock (gouge).

This study reveals several similarities regarding surface faulting:

1) the faults identified do not correspond to single discrete surfaces, but are associated with complex and powerful zones of deformation that sometimes reach plurimetrical thicknesses;

2) these deformation zones, or 'fault zones', are often bordered by two main slip surfaces and include fault rocks within them;

3) in some cases, deformation also extends outside the fault zones with the formation of areas of intense fracturing; deformation may also cause the development of secondary slip surfaces and the rotation of schistosity

4) vegetation cover and debris sediments of Quaternary age are not cut by the identified fault surfaces.

In summary, the geometry of the identified fault systems, the interaction between fault zones and undamaged rocks, the large volumes, the chaotic appearance and the classes (damaged rocks, breccias, cataclasites, gouges) of the faulted rocks observed along the outcrops are attributable to past tectonic activity due to long-term geological processes acting on a large scale.

Therefore, the set of observations collected allow us to associate the fault system outcropping on the surface in the area of the Menta dam with a complex architecture, not ascribable to local and recent movements, but rather to ancient geological processes. The faults that acted in geological times have since been exhumed and probably accommodated multi-decametric rejections. These structures also appear sealed by the Quaternary surface blanket and this evidence excludes their re-activation in recent times. Consequently, all the considerations made rule out the presence of active and capable faults (FAC) in the area in the immediate vicinity of the Menta dam. This result also confirms the reliability of the ITHACA database (Capable Fault Catalogue), which does not indicate FAC in correspondence with the summit part of Aspromonte and in correspondence with the area of the dam.

4.4 Monitoring system

The complex monitoring system of the Menta Dam provides data acquired mainly automatically to form a large database available to the managing authority. This monitoring system makes it possible to record the measurements of interest relating to the main cause and effect quantities, with the appropriate frequencies, highlighting the trends and being able to identify and analyse the evolutionary characteristics of the main phenomena concerning both the deformation aspects of the structure and the hydraulic and filtration aspects through the foundations of the dam structure.

The monitoring system includes the measurement of:

- flow rates in the drainage system
- interstitial pressures at the piezometers
- plano-altimetric displacements and deformations by means of inclinometers, settlement meters and precision levelling.

Finally, a weather station allows the monitoring of relevant atmospheric parameters.

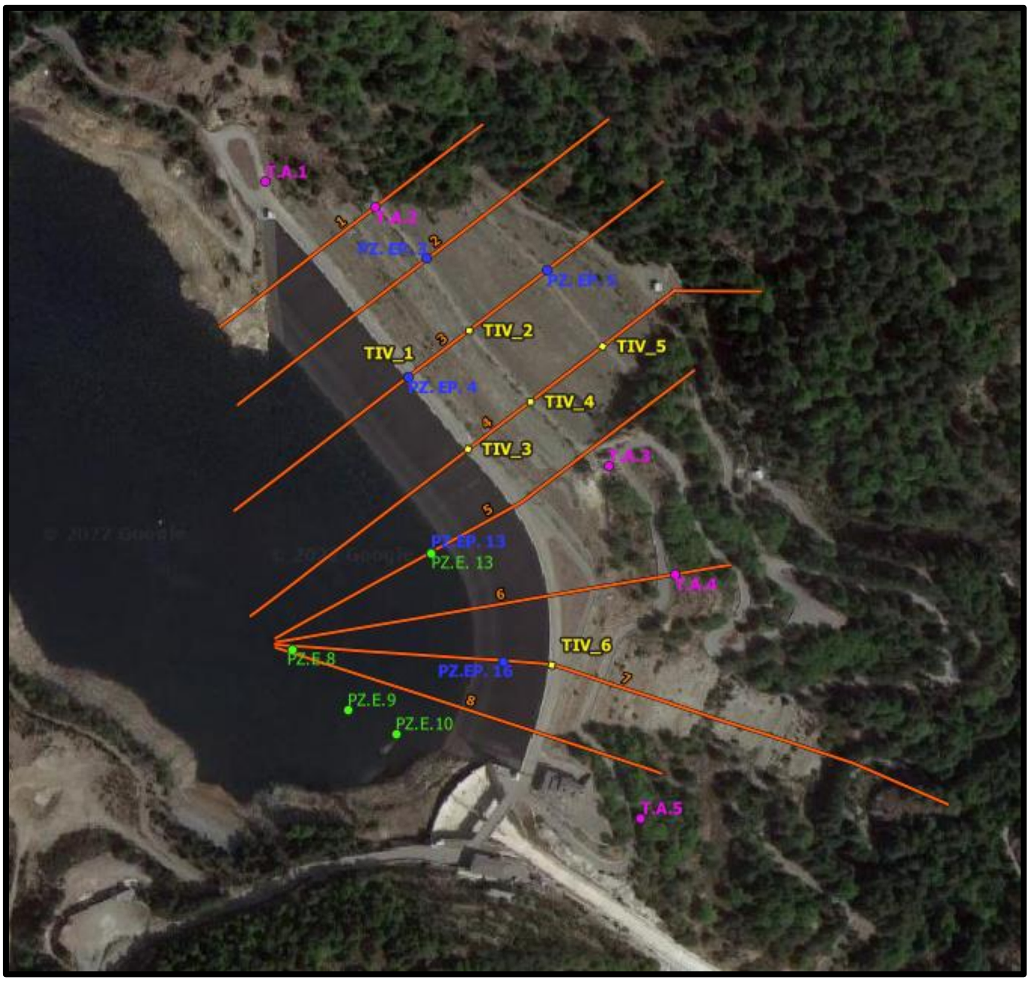

Figure 4.14: monitoring system and location of inclinometers and piezometers

The piezometers are placed at points inside the dam body, on the backs and in the foundations, as shown in Figure 4.14.

Five electropneumatic piezometers are installed in the foundation rock formation; of these, only three are still in operation (PZE4, PZE13 and PZE16, in blu colour); five electric piezometers are located in the bedrock formation along the perimeter trench at the foot of the upstream face of the dam; of these, four are currently in operation (PZE7p, PZE8p, PZE9p PZE10p, in green colous). Finally, open-tube piezometers located on the backs of the dam body, on the crest and on the downstream face of the dam at depths that reach the bedrock formation (in magenta colour).

Instead, biaxial inclinometer tubes are installed along sections 3, 4 and 7 on the top embankment and valley banks (in yellow).

In particular:

- TIV 1 and TIV 3 inclinometers are located on the crest along sections 3 and 4 respectively;

- TIV 2 and TIV 4 inclinometers are located on the second valley berm along sections 3 and 4 respectively;

- TIV 5 inclinometers are located on the third valley berm along section 4;

- Finally, inclinometer TIV 6 is located on the crest on the right bank along section 7.

The monitoring system involves measuring the plano-altimetric displacements of the 16 fixed points (8 on the crowning, 3 on the first bank of the valley, 2 on the second bank of the valley and 3). Figure 4.15 shows the triangulation network.

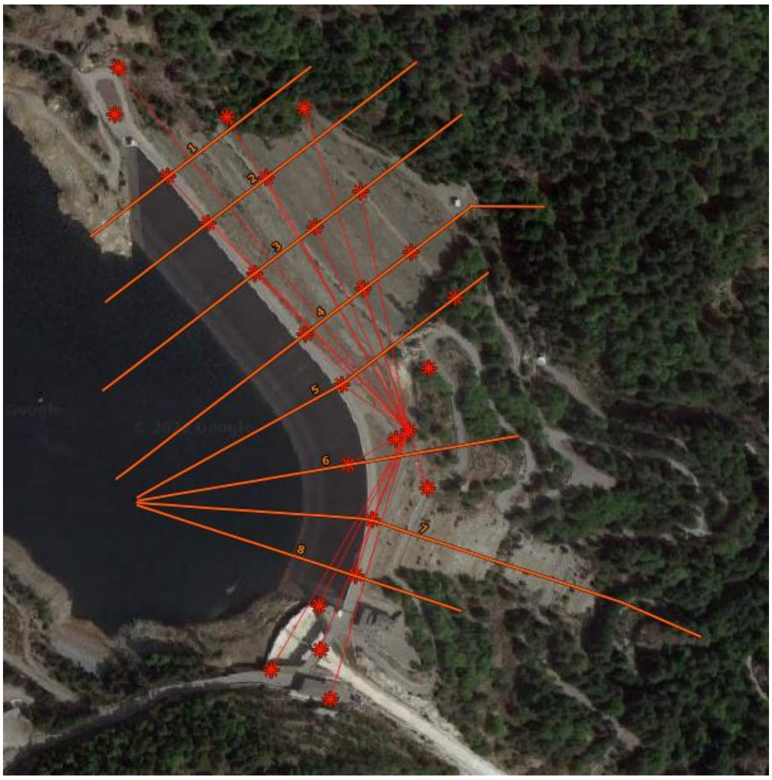

Figure 4.15: Triangulation network for plano-altimetric measurement.

4.5 Impoundment Period

The reservoir level represents a 'cause' quantity of the Menta dam.

The experimental reservoir period begins in 2010 until 2018, during which the behaviour of the dam at different variations of the reservoir level was observed.

From the end of 2018, however, the dam's operational period begins.

Figure 4.16 shows the reservoir level from the end of 2011 until November 2022.

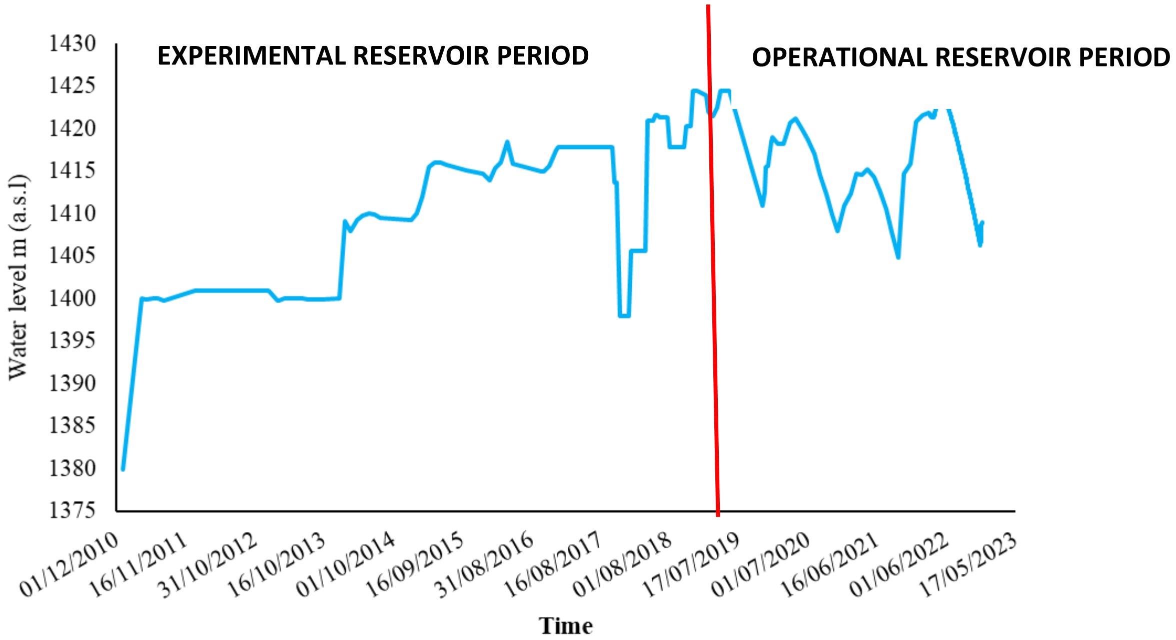

Figure 4.16: water level from experimental period to operational period.

It can be seen that until 2014 the reservoir levels are more or less constant at around 1400 m a.s.l. From January 2014 - December 2018, they have oscillated

in the range between the minimum altitude 1399.00 m.a.s.l, recorded in October/November 2017, and the maximum altitude 1424.50 m.a.s.l, corresponding to the height of the overflow threshold of the surface drain. It noted that throughout the year 2014 and until mid-February 2015 the water level in the reservoir was in fact kept constant at 1410.00 m.a.s.l.
Between mid-February and the end of March 2015, the reservoir level to 1418.00 m.a.s.l., then remained constant until the end of October, when October, at which point a rapid rise was observed up to the altitude of 1422.00 m.a.s.l., probably caused by a flood event associated to a rainfall event of considerable intensity and persistence. In the following days the reservoir level returned to its previous elevation of 1418.00 m.a.s.l. and then remained more or less constant until the end of 2016. Since mid January 2017, the level began to rise, reaching an altitude of 1421.00 m.a.s.l. at the end of February and then remaining more or altitude until around the end of August, at which point it began a at the end of September, reaching the lowest altitude recorded in the five five-year reference period of 1399.00. From the beginning of October to the end of December of 2017, the reservoir level remained more or less constant at 1399.00/1400.00 m a.s.l. From the beginning of January 2018, the reservoir level began to rise almost constantly until the end of April 2018 reaching an altitude of 1423.00 m a.s.l. From the beginning of May until 10th October of 2018, the level dropped until it reached 1418.00 m a.s.l. From approximately mid-October 2018, the level rose again until it reached the maximum regulation altitude of 1424.50 m a.s.l. Since the end of 2109, is observed cyclical phases of emptying and flooding occurring during the dam's operational period. In fact, the draining takes place during the second half of the year and the flooding during the first half. During June 2022, the maximum reservoir height of 1424 m a.s.l. is reached, while the second half of the year is characterised by a reservoir period at a height of approximately 1405 m a.s.l.

Chapter 5

Displacement of the dam embankment: inclinometric measurement

In this chapter, the data analysis carried out for the inclinometer measurements will be described. The results of the inclinometer measurements will then be shown by dividing them into two time periods: from 2011 to 2018, which is the experimental reservoir period, and from 2019 to 2022, which is the operational period of the dam, referring to the sections of the dam indicated in Chapter 4. The inclinometer measurements will then be compared with the reservoir level in order to better interpret the physical behaviour of the dam.

5.1 Inclinometer characteristics

As previously described in Chapter 4, the dam has an efficient and effective monitoring system consisting of piezometers, inclinometers and topographic levelling, located largely along the eight sections identified on the dam body. The deformation of the dam is controlled by inclinometer holes with a vertical axis, located along the crown of the dam and on the two berms of the downstream face as shown in Figure 5.1.

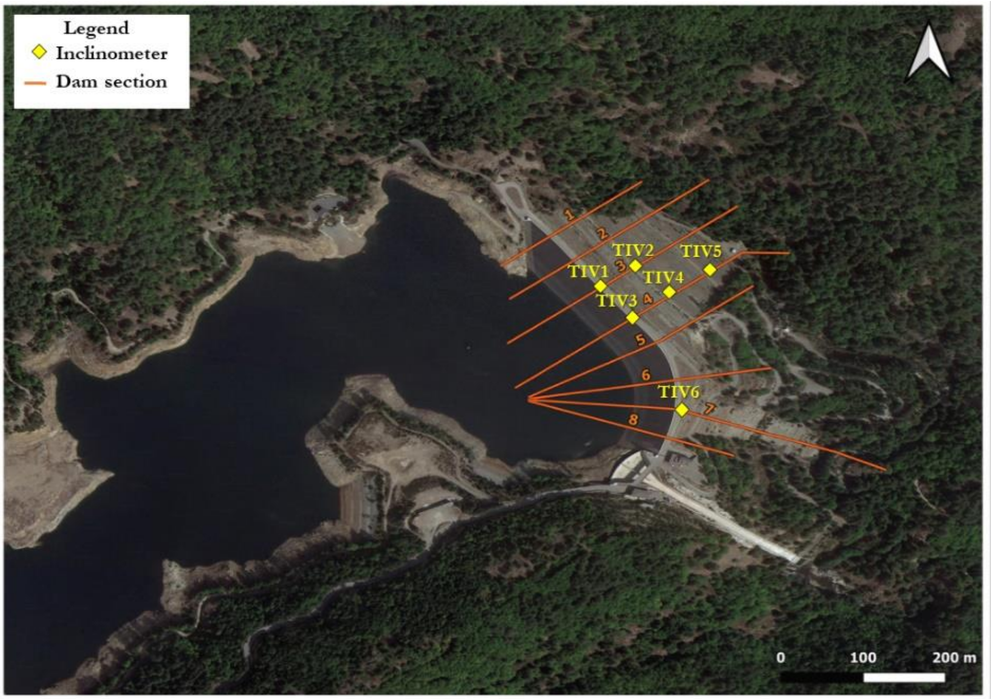

Figure 5.1: Location of vertical biaxial inclinometers.

In detail, along section 3, inclinometers TIV 1 and TIV 2 are installed, with depths of 85m and 69m respectively, positioned at an altitude of 1431m and 1404 m a.s.l.; along section 4, on the other hand, the inclinometers TIV 3, TIV 4 and TIV 5 are installed, with depths of 68m, 47m and 34.0m respectively at an altitude of 1431.75m, 14045.50m and 1377.50m a.s.l. On the crown of section 7, the TIV 6 inclinometer is installed at a depth of 25 metres at an elevation of approximately 1400m a.s.l. Table 5.1 provides a summary of the characteristics of inclinometers.

Table 5.1: Characteristics of inclinometers.

	T I V 1	**T I V 2**	**T I V 3**	**T I V 4**	**T I V 5**	**T I V 6**
Depth (m)	85	69	68	47	34	25
Section	3	3	4	4	4	6
Altitude (m a.s.l.)	1431.75	1404.50	1431.75	1404.50	1377.60	1404.50

5.2 Data analysis: inclinometric measurements

5.2.1 Available inclinometer data

The inclinometers installed on the have a very large dataset of manual readings, from January 2011 to November 2022, with monthly frequency. The readings consist of measuring the angle between the sensor axis and the vertical axis at constant depth intervals (1 meter), every meter along the vertical. For each measurement, four readings were taken corresponding to the two guides A and B in both positive and negative directions. By convention, the two A and B guides are placed orthogonally, i.e. the B guide is at 90° clockwise following the positive direction of the sensor. In detail, guide A corresponds to the reference guide and corresponds to geographic North while guide B corresponds to East.

- *Data processing*

The readings were taken manually using an inclinometer probe along the 4 inclinometer guides. The values obtained represent the inclinations of the tubes, which were subsequently converted into lateral deviations and displacements at each depth according to the following formula:

$$A = P \sin(\alpha_A)$$
$$B = P \sin(\alpha_B)$$

Where P is the measurement step.

Then the incremental displacement of the tube (D) and the azimuth angle θ was determined at each borehole depth was calculated.

$$D = \sqrt{(A^2 + B^2)}$$

$$\theta = arctg\,\frac{A}{B}$$

- *Cumulated displacement*

The total or cumulated displacement of the inclinometer at a given distance from the edge, at a certain time, compared to the initial reference profile, results from the summation of the displacements for the already measured length. The total displacement is obtained by summing up the incremental displacement along both guide A and B as follows:

$$D_{Ai} = DA_{\,i-1} + \delta A_i$$

$$D_{Bi} = DB_{\,i-1} + \delta B_i$$

$$Di = \sqrt{(DAi^2 + DBi^2)}$$

Where *i* depends on the number of measurements along the pipe.

Total displacement - depth graphs were therefore obtained for each reading and for each inclinometer pipe. All measurements refer to the “zero reading” dated 13/04/2011, as shown as an example in Figure 5.2. The graphs obtained show in which height and zone of the dam there is a greater displacement.

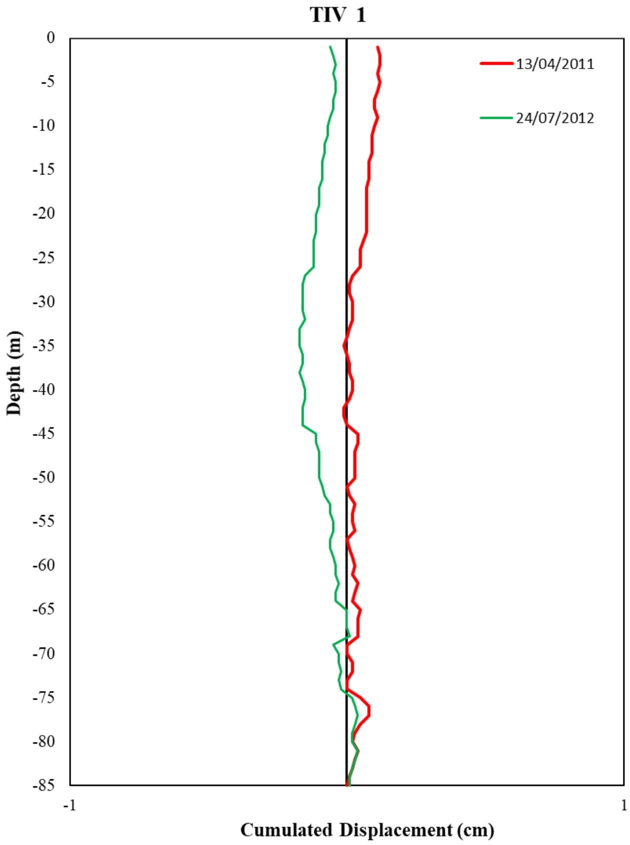

Figure 5.2: Cumulated displacement - depth graph for inclinometer TIV 1. In red is the zero reading (13/04/2011).

- *Displacement direction*

The azimuth of the resulting displacement vector was defined for each reading interval, along the length of the inclinometer vertical. To define the azimuth (Fig. 5.3), a relative cartesian axis system is adopted in which the X-axis coincides with the transverse plane, in this case the B^+ and B^- guides, and the Y-axis coincides with the A^+ and A^- guides. The four guides, oriented clockwise, identify the angular values of a cartesian reference, as shown in Figure 5.3. The direction of displacement along the vertical, i.e. the azimuth, was also calculated, taking into account the orientation of the A+ rail with respect to geographic north for all inclinometers.

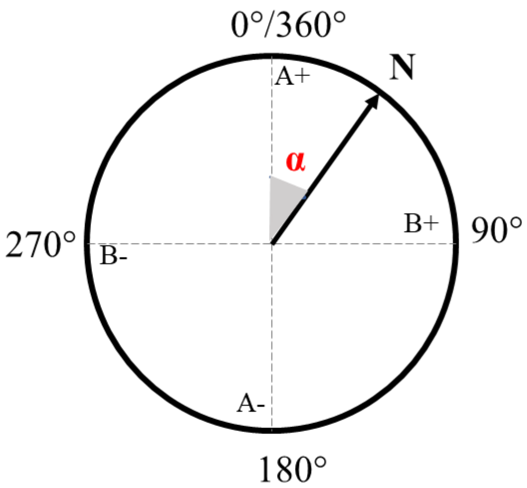

Figure 5.3: Representative scheme of the guides and the displacement vector.

In the case study, Guide A^+ represents the reference guide, but it does not coincide with geographic north, i.e. it is oriented by an angle α with respect to North. Therefore, the following four cases were used to define the azimuth θ along the vertical

Case 1:

if A > 0 - B > 0

$\Theta = (arctg \frac{A}{B}) + \alpha$

- **Case 2:**

if A > 0 – B < 0

$\Theta = (arctg \frac{A}{B} + 180°) + \alpha$

- **Case 3:**

if A < 0 – B < 0

$\Theta = (arctg \frac{A}{B} + 180°) + \alpha$

- **Case 4:**

if A < 0 – B > 0

$\Theta = (arctg \frac{A}{B} + 360°) + \alpha$

Where α is the orientation of guide A with reference to geographic North.

Graphs recording the azimuthal displacement trend along the vertical were then obtained for each reading and for each inclinometer. Figure 5.4 shows the graph of the zero reading of the TIV1 inclinometer as an example.

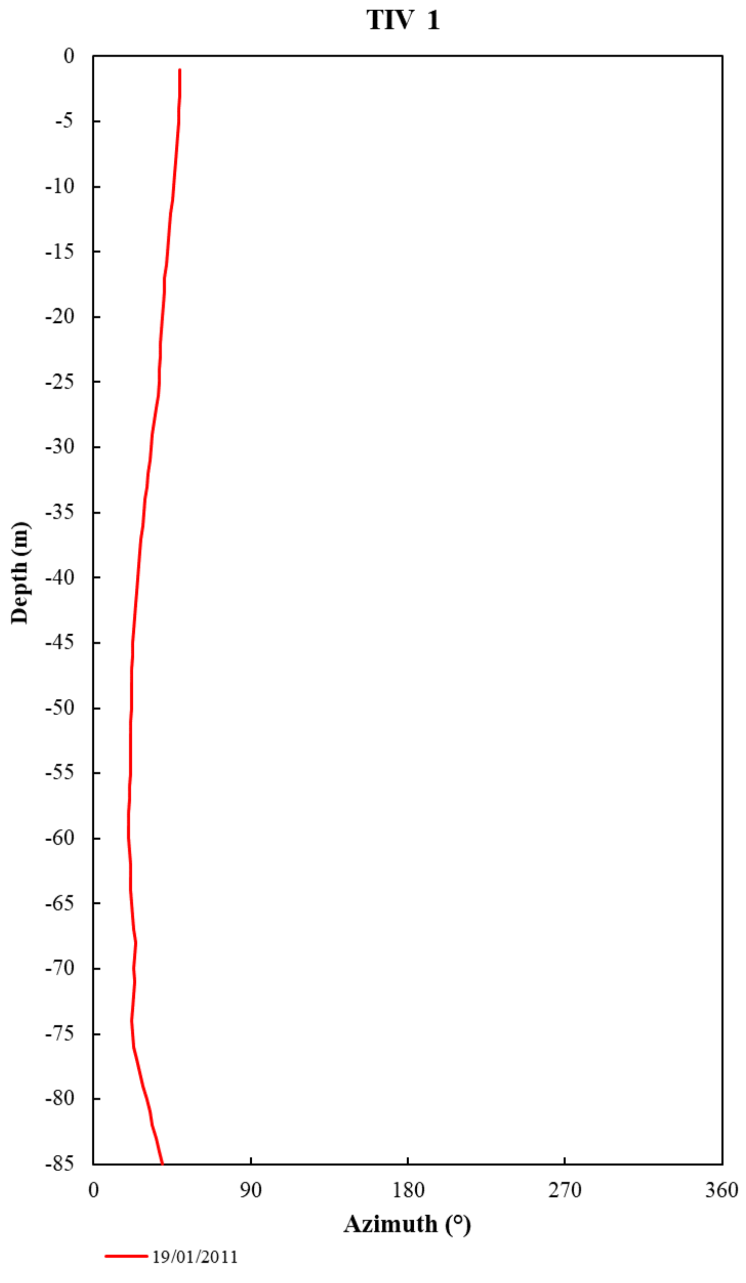

Figure 5.4: Example of the azimuth-depth diagram of the zero reading of the TIV 1 inclinometer.

5.2.2 Water level

One of the main 'cause' quantities of the dam is the reservoir level. As previously mentioned, we will refer to two time periods of analysis:

1) Experimental reservoir period: from January 2011 to December 2018 (Figura 5.5)
2) Operational period: from January 2019 to November 2022.

- *Analysis of reservoir level during the experimental period* (forse non è necessario ripetere questa descrizione già fatta nel paragrafo 4.5)

During the period of the experimental reservoir (Fig. 5.5), it can be seen that from 2011 to January 2014 the reservoir level has been held constant at approximately 1400 m a.s.l., which corresponds to the maximum height allowed during the first years of the experimental reservoir. The level measurements acquired during the observation period January 2014 - December 2018, fluctuated in the range between the minimum altitude 1399.00 m a.s.l, recorded in October/November 2017, and the maximum altitude 1424.50 m a.s.l, corresponding to the height of the overflow threshold of the superficial drain. It is observed that throughout the year 2014 and until mid-February 2015, the water level in the reservoir was constant at 1410.00 m a.s.l. Between mid-February and the end of March 2015, the reservoir level rose to an altitude of 1418.00 m a.s.l., and then remained constant until the end of October, when a rapid rise to an altitude of 1422.00 m .a.s.l. was observed, probably caused by a flood event associated with a rainfall event of considerable intensity and persistence. In the following days, the reservoir level dropped back to the previous altitude of 1418.00 m a.s.l. and remained steady until the end of 2016. From mid-January 2017, the level began to rise, reaching an altitude of 1421.00 m a.s.l. at the end of February and then remaining constant until the end of August. From this point on, a decrease began, reaching the lowest altitude of 1399.00 m a.s.l. at the end of September. From the beginning of October to the end of December 2017, the reservoir level remained approximately constant and equal to 1399.00/1400.00m sl. From the beginning of January 2018, the reservoir level began to rise almost constantly until the end of April 2018 reaching 1423.00 m a.s.l. From the beginning of May until 10th October 2018, the level dropped until it reached 1418.00 m a.s.l. From approximately mid-October 2018, the level rose again until it reached the maximum regulation altitude of 1424.50 m a.s.l.

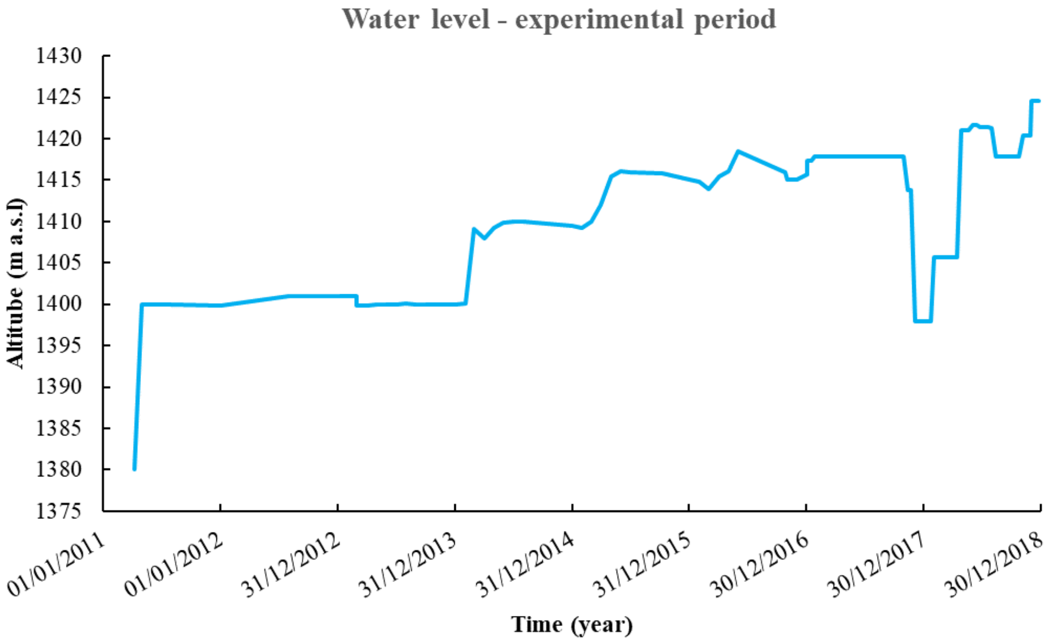

Figure 5.5: Variation of the reservoir level during the experimental reservoir period.

- *Analysis of reservoir level during the operational period*

In 2019, the beginning of the dam's operational phase (Fig. 5.6), the reservoir level is around 1424.50 m a.s.l. until mid-August of the same year. Subsequently, an ascent begins at an altitude of 1419 m a.s.l. until it reaches 1421 m in the first half of 2020. In the second half of the year, the level reaches an altitude of 1408 m a.s.l. to rise again in January 2021 and settle at around 1415 m a.s.l. As in previous years, the trend shows a descent from June 2021, and reach the lowest reservoir altitude, i.e. 1405 m a.s.l. In contrast to previous years, in October 2021 a steady ascent begins until reaching 1424 m a.s.l. in

May 2022. From June 2022, a descent begins until it reaches 1406 m in November 2022. It can be seen that the reservoir level during the operation phase of the dam shows a cyclic trend, decreasing from the second half of the year and reaching a highest peak in May, more or less for all the years examined.

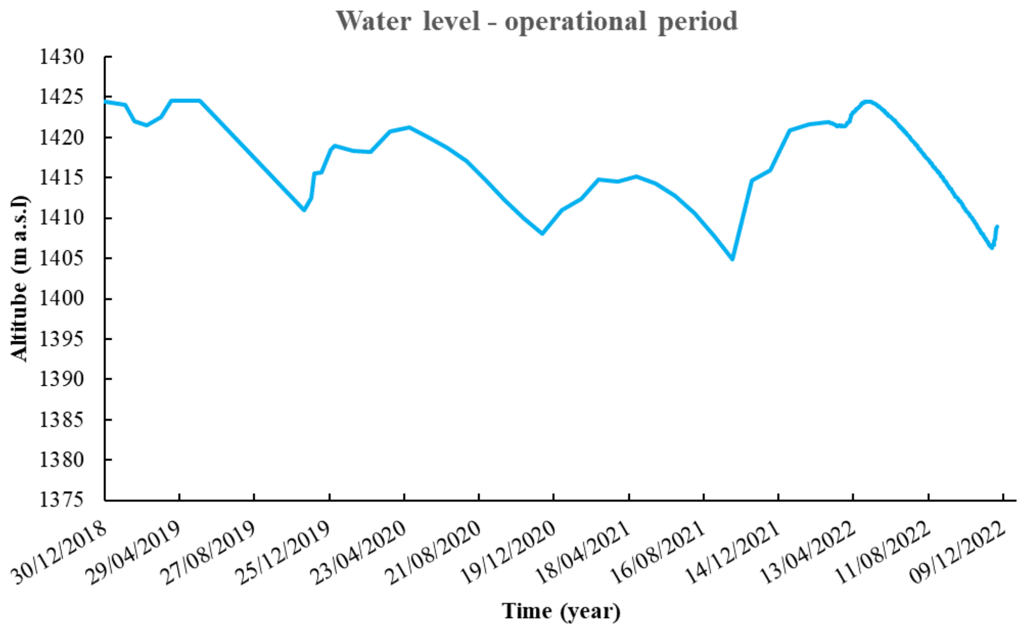

Figure 5.6: Variation of the reservoir level during the operational reservoir period.

5.3 Results

In the following, the results obtained from inclinometer processing will be shown and described, divided into the two previously described phases, relating to the period of experimental reservoir and dam operation. Given the large quantity of data, a limited number of datasets, mostly significant, will be represented in order to make reading and interpretation clearer. The curves for each year for each inclinometer are attached in Appendix 1

5.3.1 Experimental Reservoir Period

- *Section 3*

Along section 3 of the dam, inclinometers TIV 1 on the crest and TIV 2 on the second downstream berm are located. Figure 5.7 shows the plan and section location of the inclinometers.

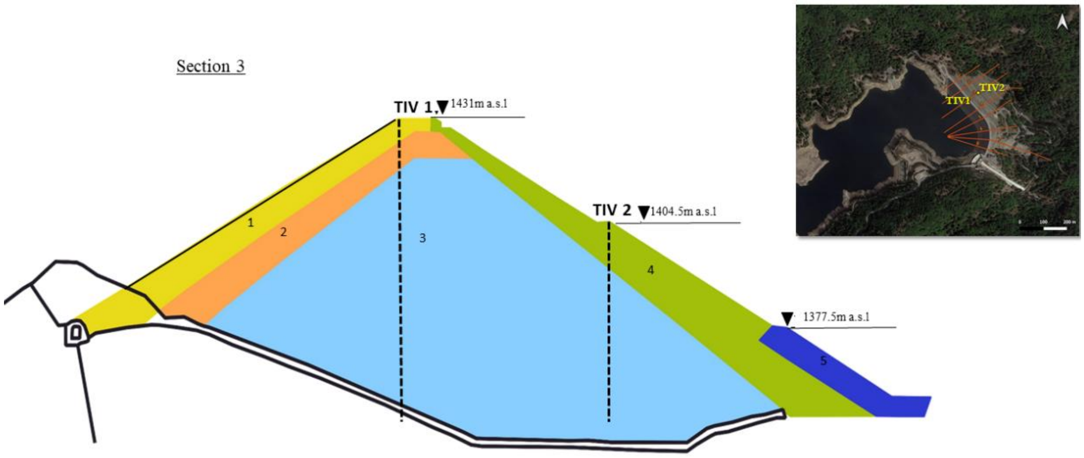

Figure 5.7: location of TIV 1 and TIV2 inclinometers in plan and section.

The cumulative displacement graphs of inclinometer TIV 1 and TIV2 from 2011 to 2018 are shown in Figures 5.8 and 5.9, one per year, with July chosen as the reference month.

The cumulative displacement graph of the TIV1 inclinometer shows that 2011 measurement reflects the imperfect verticality of the inclinometer tube in the first 25 metres. Starting in 2012, there is an increase in horizontal displacement of about 1 mm at a depth of 25 m to a depth of about 45 m, showing no significant displacement at shallower depths. This trend appears to be constant for following 3 years, in fact in 2015 there is an increase in the borehole head displacement of about 1 mm, which increases until 2018 reaching a maximum displacement of about 3 mm up to a depth of about 25 m, and then decreases as the depth increases. The diagrams show that, as the displacement increases, the direction does not change over time, showing itself to be consistent throughout the time interval examined. In fact, a perfect overlap of the curves can be seen. The direction of the displacement also varies slightly along the vertical in an interval between 50°N at the head of the tube and approximately 37°N at the bottom of the borehole, both thus showing a downward movement.

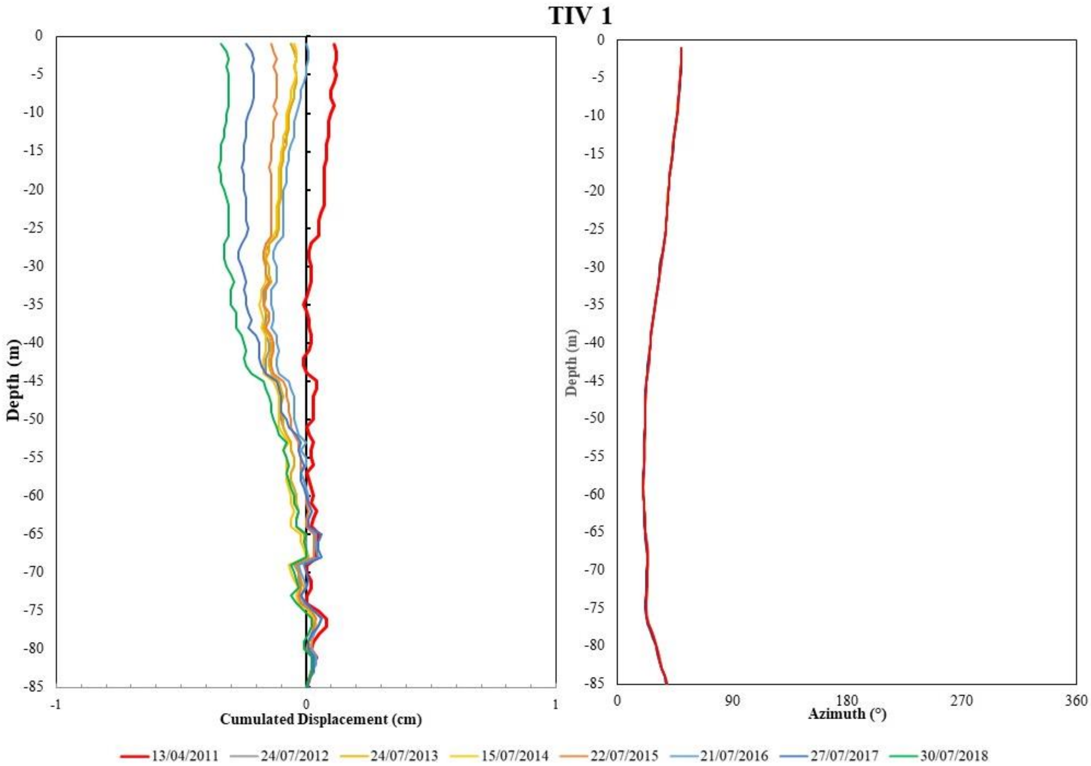

Figure 5.8 Diagram of the cumulative displacement (on the left) and azimuth curves (on the right) of the TIV1 inclinometer.

Whereas on the crowning (TIV1) there is a slight movement, downstream the situation appears different. Figure 5.9, represents the cumulative displacements and the relative direction of the inclinometer TIV2, located along the second valley berm. The cumulative-displacement graph shows displacements below mm in the first 24 m of depth, where there is a slight discontinuity, most likely due to the non-vertical nature of the instrument. Again, the direction of the displacement is consistent with the expected movement, i.e. downstream. In fact, the azimuth varies from 53°N at the head of the pipe to 36°N at the bottom of the borehole. We can see that at about 50m to 60m the direction is 17°N.

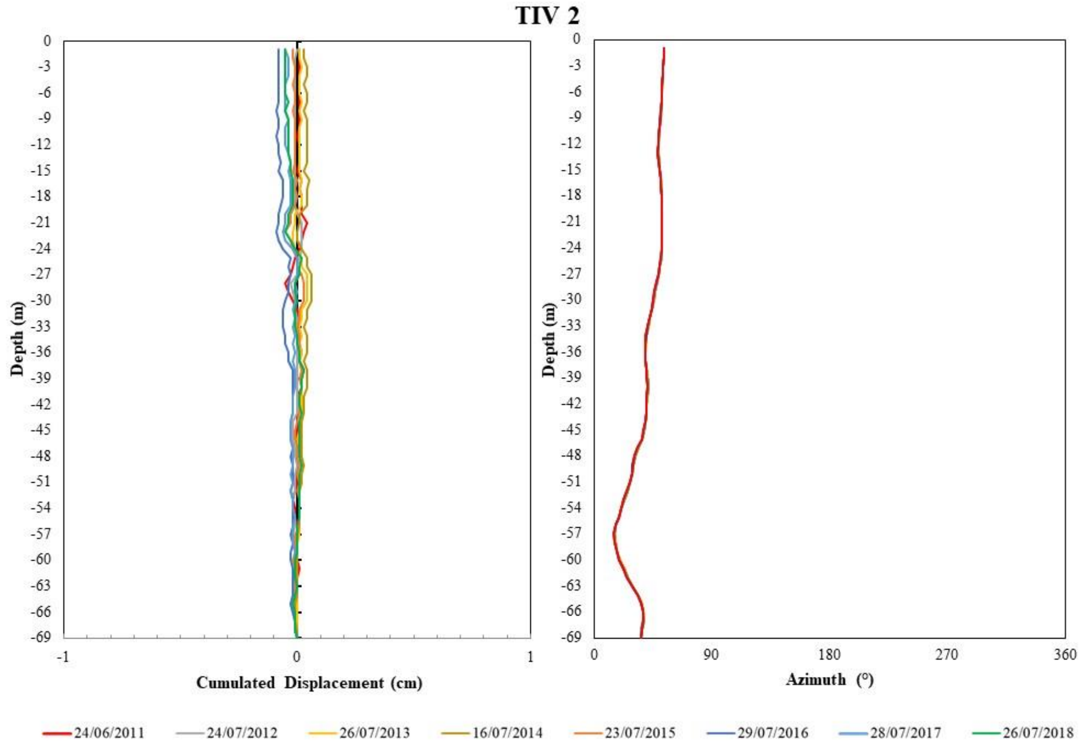

Figure 5.9: Diagram of the cumulative displacement (on the left) and azimuth curves (on the right) of the TIV 2 inclinometer.

By plotting the displacement graphs according to their orientation along section 3 (Fig.5.10), it can be noted that the displacements recorded in the TIV 1 inclinometer are mainly located in zone 3 of the dam and their direction is towards W, i.e. downstream. It can therefore be seen that, over time, there is an increase in displacement, although slight, from the crest to zone 3 of the dam. No significant displacement is recorded in the TIV 2 inclinometer.

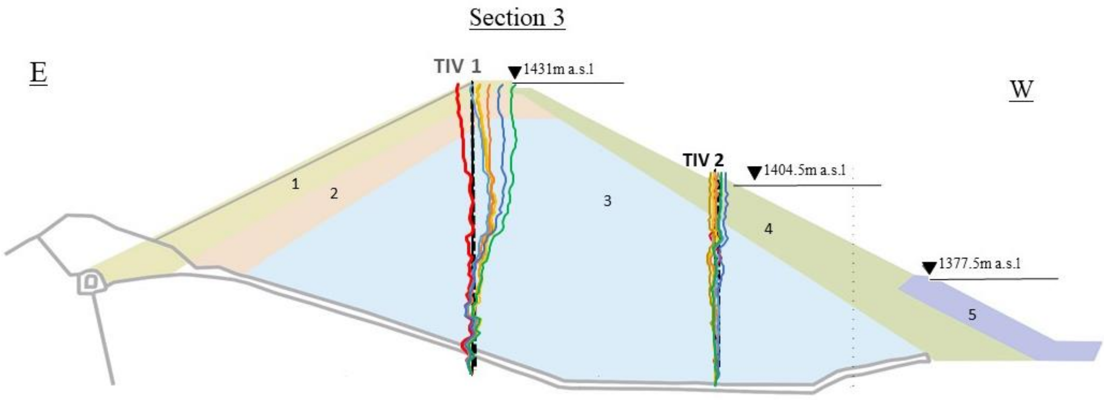

Figure 5.10: Graphical representation of the displacements of inclinometers TIV 1 and TIV 2 along section 3, according to their direction.

- *Section 4*

Along section 4 of the dam, inclinometers TIV3 on the crest and TIV 4 and TIV 5 on the second and third downstream berm are located. Figure 5.11 shows the plan and section location of the inclinometers.

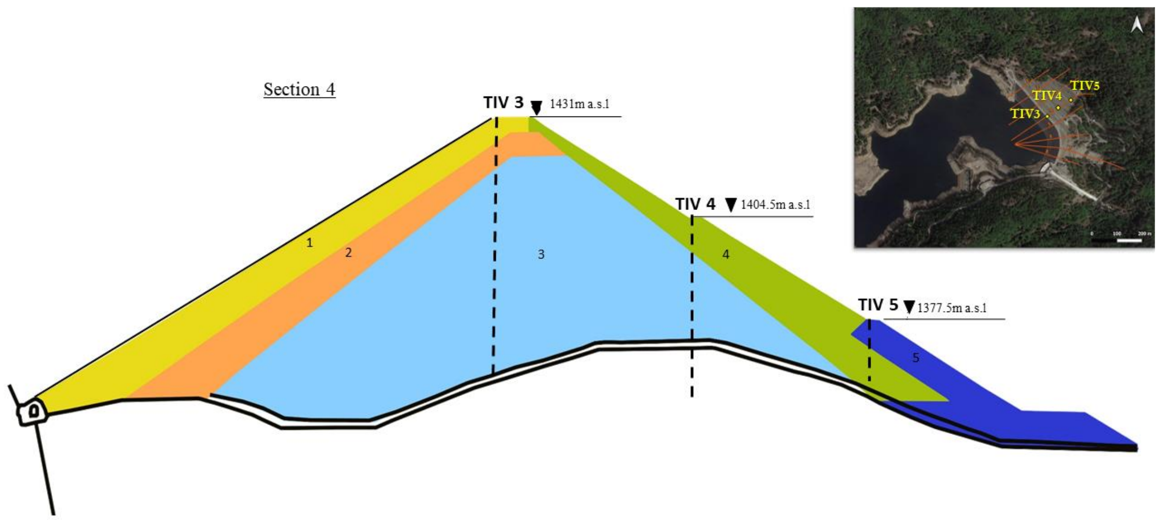

Figure 5.11: Location of TIV 3, TIV 4 and TIV 5 inclinometers in plan and section.

Along section 4, as well as along section 3, there is a considerable difference in the displacements occurring on the crown and downstream. In the TIV 3 and

TIV 4 inclinometers, discontinuities in the displacement profile are observed in bands of 2/3 meters at certain depths. In detail, along the vertical of the TIV 3 inclinometer (Fig. 5.12), a discontinuity is observed between 15 and 20 m depth. This discontinuity is observed for the whole interval examined. It can also be seen that, in the area above up to ground level, the displacements show a tendency to increase over time, at a maximum order of 2.5 mm. the data thus show a displacement in the horizontal direction with respect to the underlying portion of the embankment. From the graph of the azimuth along the vertical, it can be seen that the displacement in the first 40 m is about 80°N, i.e. towards the downstream, from 40 m onwards, a strong discontinuity of the azimuth is noted, showing that the displacement varies from 220°N to about 160° at the bottom of the hole. Both graphs show a consistency of displacement over time.

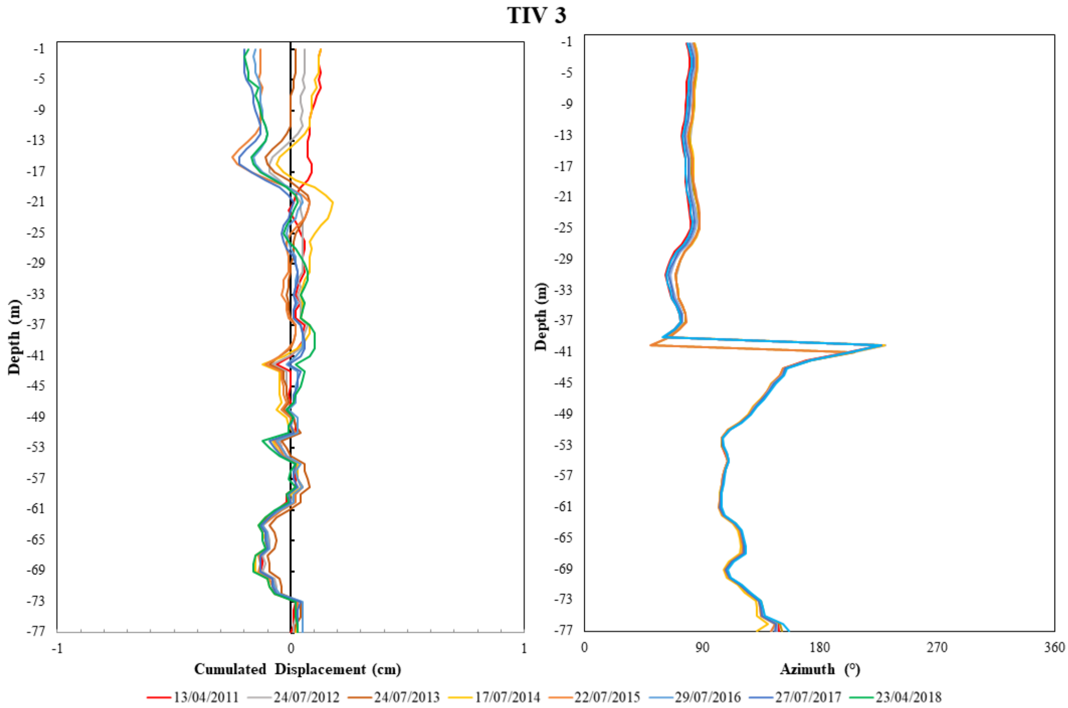

Figure 5.12: Diagram of the cumulative displacement (on the left) and azimuth curves (on the right) of the TIV 3 inclinometer.

The TIV 4 inclinometer, located on the second valley berm, also shows a discontinuity between 18 and 20 m from the head elevation of the inclinometer pipe (Fig. 5.13). Over the observation period, no displacement trends are recorded, so this discontinuity is due to the local distortion of the inclinometer pipe during the construction or installation phase. The displacement trend, on the other hand, shows a change in azimuth from approximately 45°N at the head of the pipe, i.e. movement downstream, to perfectly northwards at the bottom of the borehole.

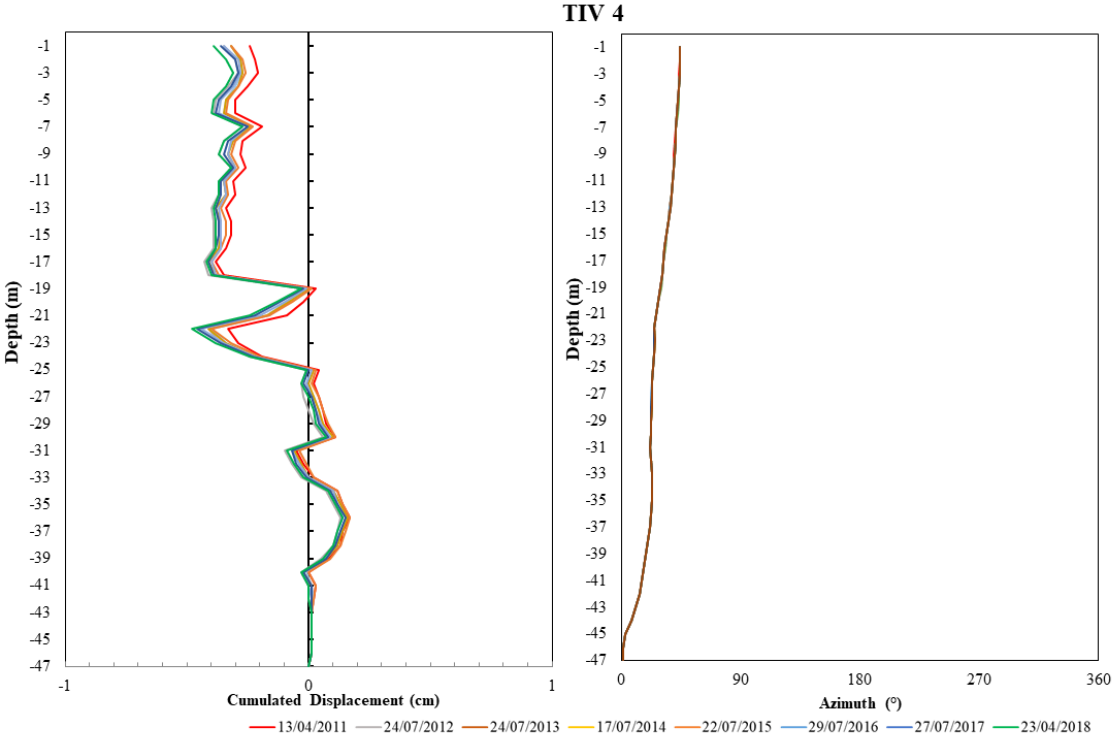

Figure 5.13: Diagram of the cumulative displacement (on the left) and azimuth curves (on the right) of the TIV 4 inclinometer.

Finally, inclinometer TIV 5, located on the third valley berm, shows a slight increase in displacements over time below mm. The direction of the displacement, also in this case, appears linear along the vertical significant displacements over time of about 73°N at the pipe head to about 30°N at the bottom of the borehole. Again, the displacements are horizontal and in a downward direction. (Fig. 5.14).

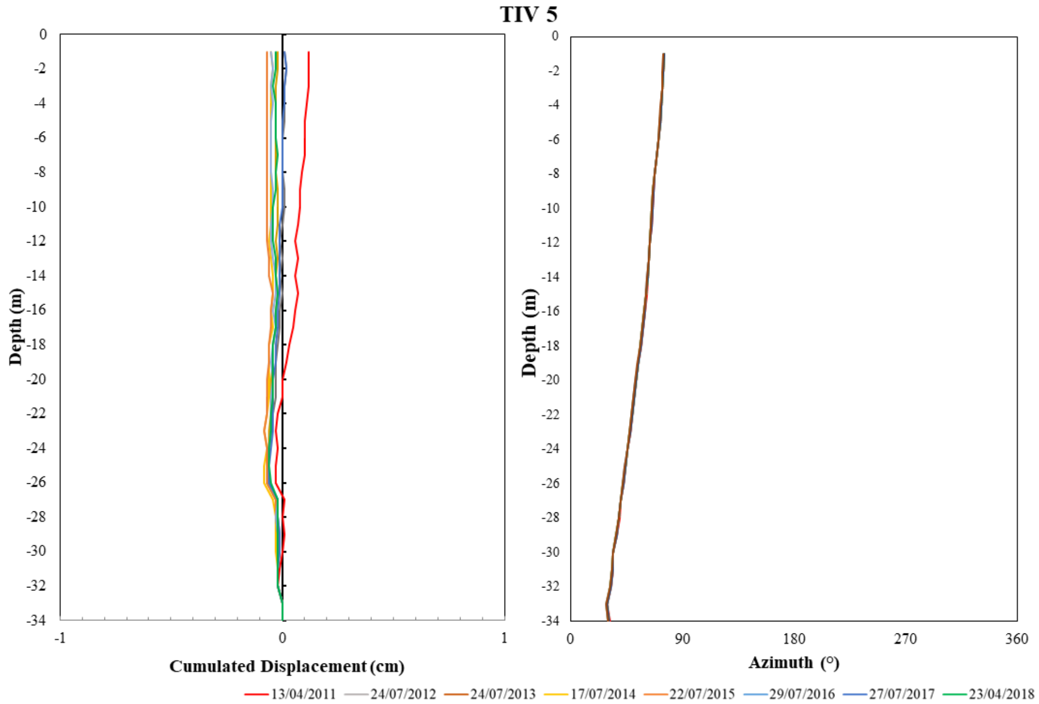

Figure 5.14: Diagram of the cumulative displacement (on the left) and azimuth curves (on the right) of the TIV 5 inclinometer.

By plotting the displacement graphs according to their orientation along section 3 (Fig.5.15), it can be noted that the displacements recorded in the TIV 3 inclinometer are mainly located in transition zone 2 and 3 of the dam and their direction is towards W, i.e. downstream. It can therefore be seen that, over time, there is an increase in displacement, although slight, from the crest to zone 3 of the dam. In contrast, the discontinuity recorded along the TIV 4 inclinometer occurs in zone 3 of the dam, although this is probably due to an inclinometer installation problem. No significant displacement is recorded in the TIV 5 inclinometer.

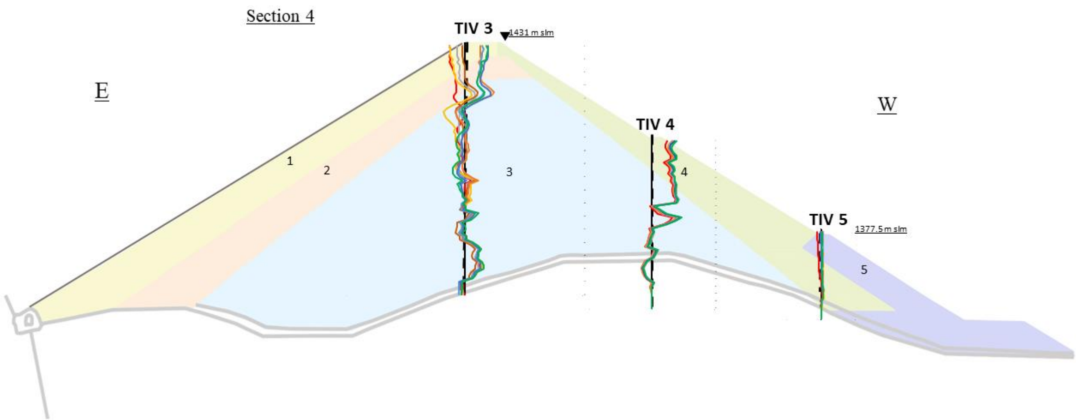

Figure 5.15: Graphical representation of the displacements of inclinometers TIV 3, TIV 4 and TIV 5 along section 4, according to their direction**.**

5.3.1 Operational Reservoir Period

The results of the cumulated displacements during the operational period of the dam, from 2019 to 2022, are herein reported. For each inclinometer, the graphs of the cumulative displacement taking into account the zero reading of 2011 and the readings related to 2019 will be shown, then considering the first reading of 2019 as the new zero reading, in order to better understand the behaviour during the operational phase.

- *Section 3*

Figures 5.16 and 5.17 show the cumulative displacement graphs comparing the readings taken during the dam's operational period with both the zero reading of 2011 (Figures 5.16a) and 5.17a) and 2019 (Figures 5.16b) and 5.17b).

The TIV 1 inclinometer confirms the trend of an increased displacement reaching approximately 4.5 mm in 2022, compared to 2011, in the first 45 m of depth. Comparing the same readings, taking the year 2019 as a reference, it can be seen that there is a slight variation in the trend, submillimetric and constant along the vertical. In Figure 5.16c, the direction of the displacement along the vertical is represented, and it is noted that there are no variations with the experimental impoundment period, confirming the azimuth of 50°N at the tube head.

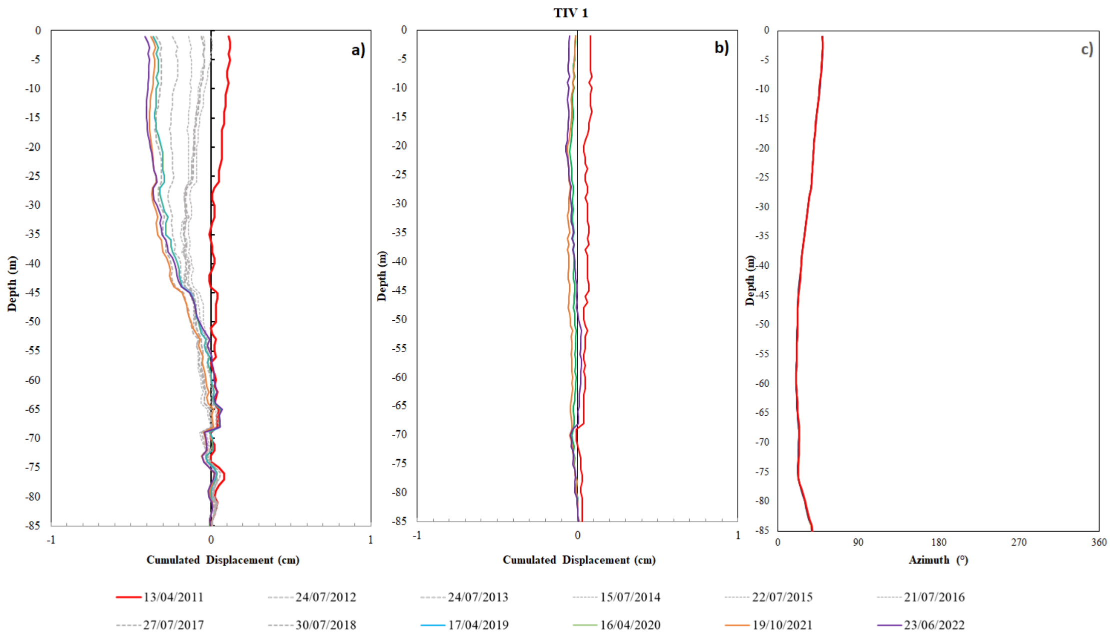

Figure 5.16: a) Graphical representation of the displacements of inclinometers TIV 1 compared to 2011; b) readings compared to 2019; c) displacement-azimuth graph.

The TIV 2 inclinometer also shows no particular shifts over time at this stage, confirming what was verified during the previous monitoring period.

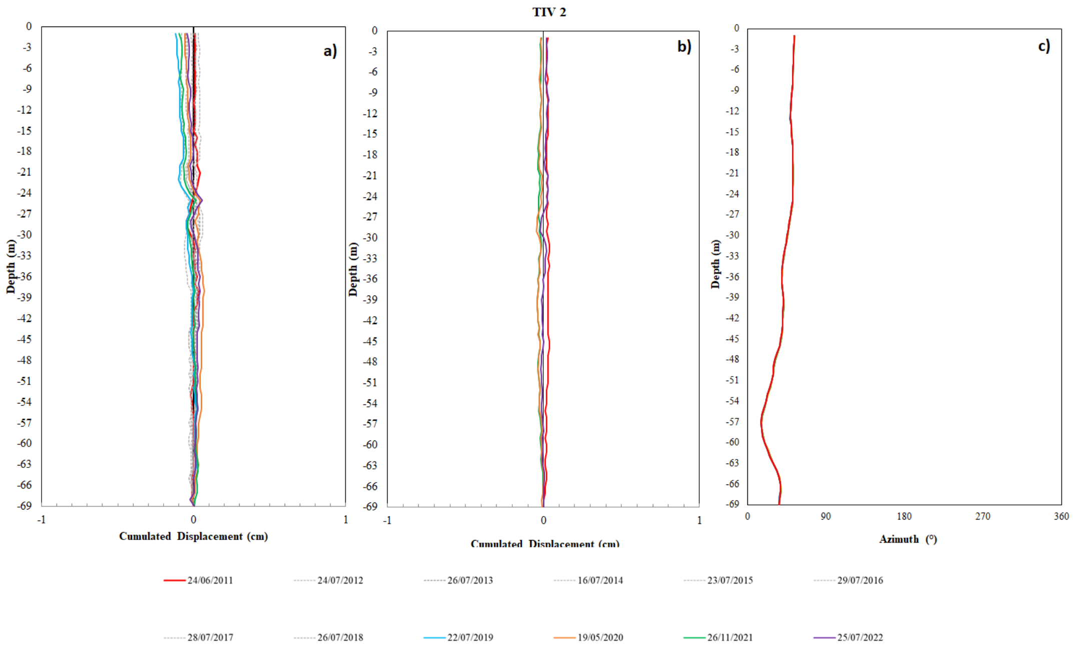

Figure 5.17: a) Graphical representation of the displacements of inclinometers TIV 2 compared to 2011; b) readings compared to 2019; c) displacement-azimuth graph.

- *Section 4*

Figures 5.18. 5.19 and 5.20 show the cumulative displacement graphs comparing the readings taken during the dam's operational period with both the zero reading of 2011 (Figures 5.18-5.20a)) and 2019 (Figures 5.18 - 5.20b).

It is interesting to note that along the TIV 3 inclinometer vertical, the comparative readings to 2011 (Fig. 5.18a) confirm the discontinuity at about 15 m depth. This discontinuity does not appear in Figure 5.18b compared to 2019. Essentially, an increase in the displacement trend compared to 2011 of about 4.5 mm is confirmed in the first 17 metres of the depth. On the other hand, comparing the displacement trend to 2019 (Fig. 5.18b) shows a stability during the period of operation. Also in this time interval, a variation in the direction of the displacement is noted, as is the experimental reservoir period.

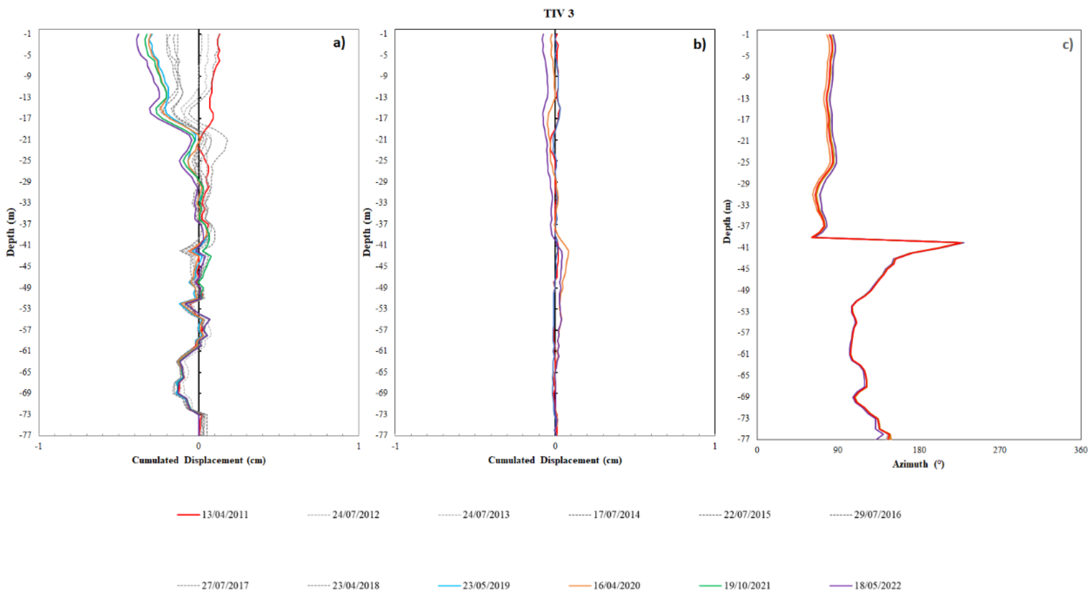

Figure 5.18: a) Graphical representation of the displacements of inclinometers TIV 3 compared to 2011; b) readings compared to 2019; c) displacement-azimuth graph.

The TIV 4 inclinometer, on the other hand, shows in both cases (Fig. 5.19a and Fig. 5.19b), a stable trend in the displacements from 2015 onwards, from which time there is almost perfect overlapping of the curves. In addition, the discontinuity verified in the experimental reservoir period is confirmed, proving that there is an error in the zero measurement. In fact, this discontinuity does not manifest itself in the comparison during the operating period (Fig. 5.19b). Finally, the azimuth (Fig. 5.19c) also shows the same trend along the vertical. Lastly, the TIV 5 inclinometer, as in the experimental reservoir period, shows no significant displacement in the operational phase. Both Figures 5.20 b) and 5.20 b) show that in 2022 the displacement tends towards perfect verticality.

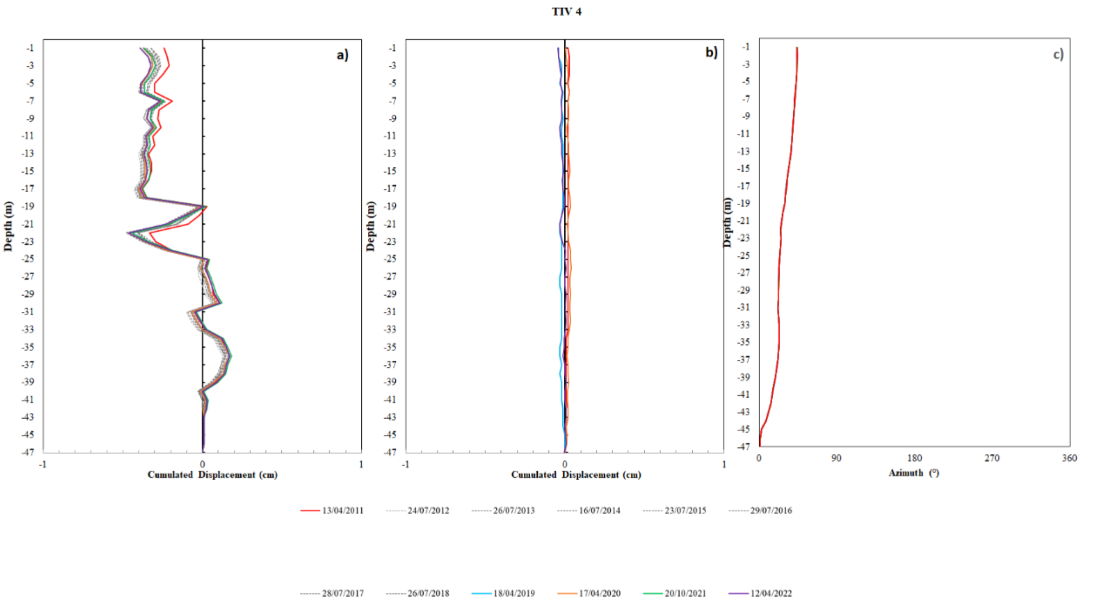

Figure 5.19: a) Graphical representation of the displacements of inclinometers TIV 4 compared to 2011; b) readings compared to 2019; c) displacement-azimuth graph.

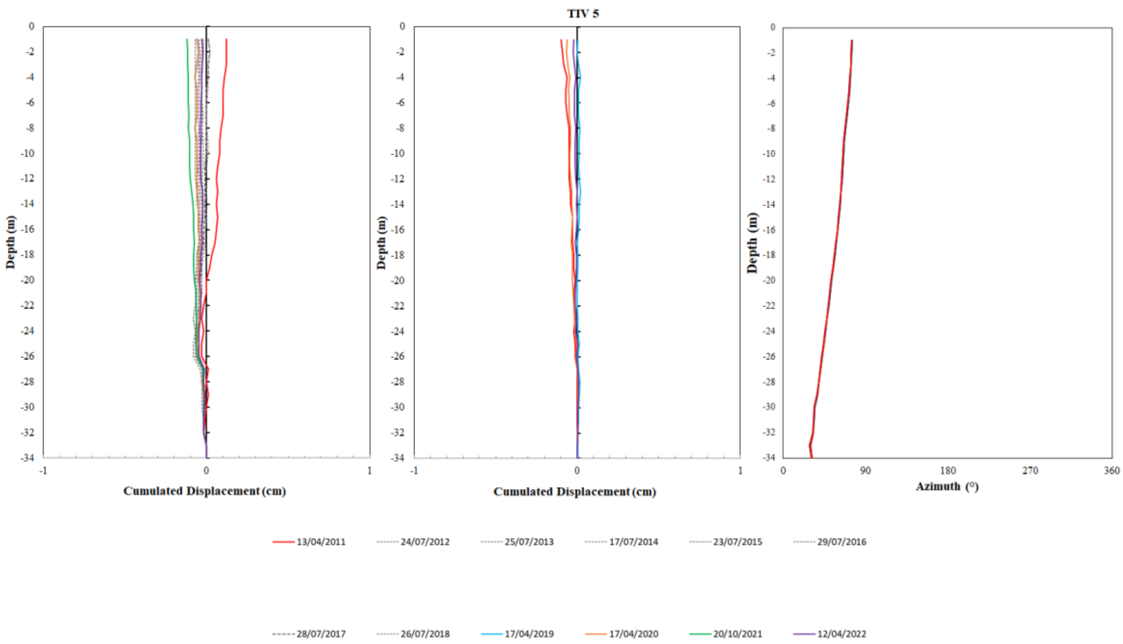

Figure 5.20: a) Graphical representation of the displacements of inclinometers TIV 4 compared to 2011; b) readings compared to 2019; c) displacement-azimuth graph.

5.3 Interpretation

The analysis of the inclinometers showed that there is a difference in the behaviour of the dam body between the crown zone and the area further downstream. In order to provide a better understanding of the displacement trend over time, from 2011 to 2022, the annual average of the displacements (AAD) at the head of the pipe, all relative to the zero reading (2011), was considered, shown in Figure 5.21.

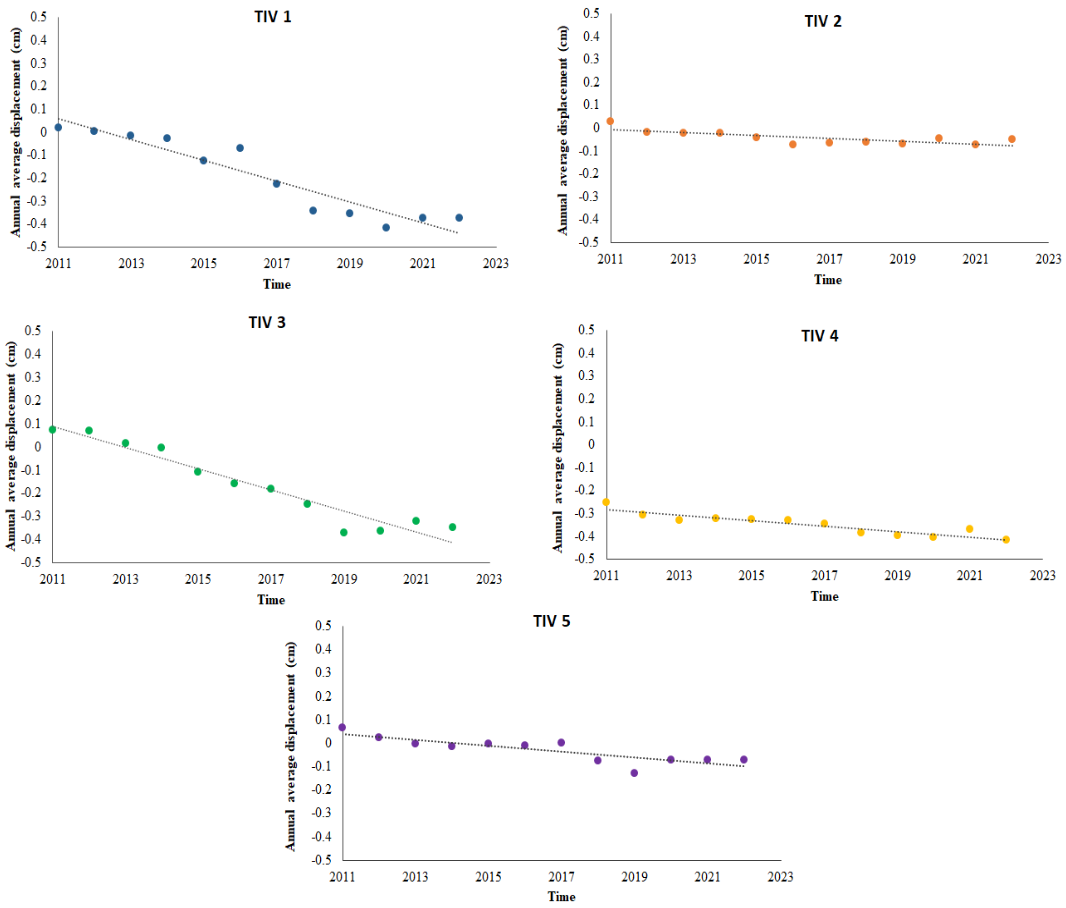

Figure 5.21: Trend graphs of average annual displacement at tube head.

The graphs demonstrate that the TIV 1 inclinometer shows a stable trend from 2011 to 2014, with millimetric displacement values. From 2015 onwards, a rather linear change in the slope of the linear trend is noted over time, until 2020, reaching approximately 4 mm. In 2021 and 2022, on the other hand, a slight change in the trend is noted, and a decrease in the displacement (around 3 mm).

A similar situation occurs for the TIV 3 inclinometer, also located on the crowning. In this case, it can be seen that from 2014 there is a change in the trend, confirmed in 2015 until 2019, reaching a maximum displacement of approximately 3.7 mm. From 2019, the trend is stable, i.e. there is no increase in displacement.

As mentioned before, the inclinometers TIV 2, TIV 4 and TIV 5, located along the second and third valley berms, show a linear trend over the entire time interval considered. It should be noted that the TIV 4 inclinometer, starting in 2011, shows a displacement start of about 2 mm, which is constant until 2022, proving that there is a measurement error in the zero reading. All these observations lead us to consider it very likely that instrumental problems exist with the inclinometer probe that leads to coarse instrumental errors on the measurements taken.

An overview of the diagrams illustrated so far shows unequivocally that, compared to the zero reading, horizontal displacements of the maximum order of 4.5 mm were recorded on the crown. These displacements are fully compatible with the stress-strain framework of the dam.

The variation of this pattern over time is to be correlated with the main causal factor acting on the structure, i.e. the reservoir level. Therefore, the cumulative displacements from 2011 to 2022 were considered, at different heights along the inclinometer verticals and correlated with the reservoir level. Figure 5.22 shows a comparison graph between inclinometers TIV 1, TIV 3 and the reservoir level. Three curves were identified for each inclinometer, relating to three depths. In particular, depth -1 (blue curve), corresponding to the head of the borehole, was considered for both, -45 and -37 for TIV 1 and TIV 3 respectively corresponding to the middle of the borehole (orange curve), and finally -89 and -77 (green curves) corresponding to the bottom of the borehole, for TIV 1 and TIV 3 respectively.

It is interesting to observe that in both inclinometers at depth -1, there is a recall of the trend comparable to the level of the reservoir. In detail, it can be seen that from 2011 to the end of 2015, despite the constant stepped reservoir, both inclinometers do not show any displacement trends. This behaviour could be due to fairly long periods of the reservoir level at a certain altitude. In fact, starting in 2016, coinciding with a rapid rise in the reservoir level to an altitude of 1418 m a.s.l., a negative peak is noted in inclinometer TIV 1, which reaches a displacement of about 3mm. In the inclinometer TIV 3, no negative peaks are noted for the same period, but a variation of the trend. Observing the period of maximum discharge in 2018, there is an immediate response in the inclinometers, reaching around 4 mm in the TIV 1 inclinometer and 4 mm in the TIV 3 inclinometer. The same negative peak can also be seen in the curve at -45 m in the TIV 1 inclinometer. Again, there is a response in the displacements with relative positive peaks. As mentioned above, from 2019 there is a change in the trend in the displacements, especially for those located in the crowning. This trend reflects the same as for the reservoir level in the operating period, where negative displacements in both inclinometers correspond to the period of emptying, as in May 2020. The same is reflected in the reservoir periods. In 2021, due to a lack of sufficient inclinometer data, there is no obvious recall in the trend. In contrast, in 2022 there are positive and negative displacement peaks that can be correlated with the reservoir level. It is therefore clear that the dam body is affected by the force acting on it. For long periods of reservoir at the same height, the dam shows stable trends. Conversely, when there are fluctuations over short periods, the dam body has a fairly immediate response. In particular it is affected at the crown, whereas at greater depths it is unaffected.

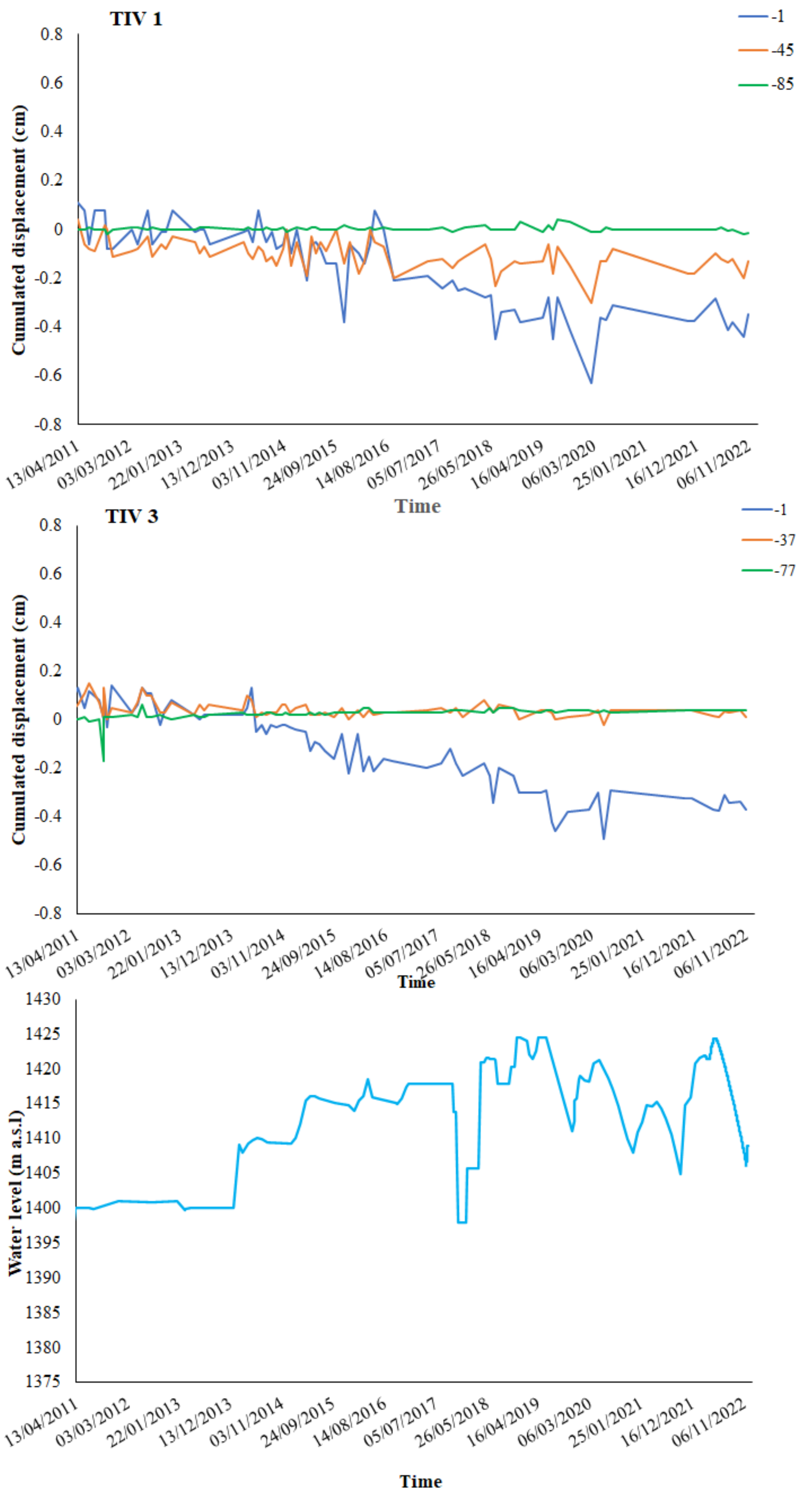

Figure 5.22: TIV 1 and TIV 3 inclinometer displacement graphs at different heights correlated with the reservoir level

Chapter 6

Displacement of the dam embankment: DInSAR measurements

This chapter will describe the data analysis carried out for the satellite measurements. As with the inclinometer measurements (Chapter 5), the satellite measurements will also be shown by dividing them into two time periods: from 2011 to 2018, which is the experimental reservoir period, and from 2019 to 2022, which is the dam operation period, referring to the dam sections indicated in Chapter 4. The satellite measurements will then be compared with the reservoir level to understand the potential of the technique and the behaviour of the dam.

6.1: Image Dataset

In order to reconstruct the evolution of ground deformations in the area under analysis, the COSMO-SkyMed (X band) and Sentinel-1 (C band) image datasets were analysed. In particular:

- 133 images acquired in ascending geometry from 25/01/2012 to 28/01/2019 with the COSMO-SkyMed sensor
- 139 images in ascending geometry from 05/06/2015 to 15/02/2020 with the Sentinel-1 sensor
- 111 images in descending geometry from 08/01/2016 to 27/06/2020 with the Sentinel-1 sensor
- 81 images in ascending geometry from 22/01/2020 to 08/09/2022 with the Sentinel-1 sensor.

The algorithm used for processing satellite radar images is called the Coherent Pixels Technique (CPT), developed by Mora et al. (2003) at the Remote Sensing Laboratory (RSLab) of the Universitat Politècnica de Catalunya (UPC). This algorithm allows the whole interferometric chain to be developed using image pairs with reduced spatial and temporal baselines and therefore characterised by a better phase response.

The processing process consists of three main phases:

- generation of the best interferograms from the available image dataset;
- selection of reflectors characterised by a fixed phase value considered indicative of a good stability of the electromagnetic response;
- calculation of the average displacement velocities and calculation of the displacement time series of the selected points over the observation period considered.

The output results obtained from processing with the CPT approach are characterised by a degree of precision and accuracy intrinsic to the application of the algorithm used.

The precision of the measurements indicates the degree of convergence of the measured values around their mean, while the accuracy quantifies the distance between the measurements and the actual datum. With reference to the interferometric datum, the issues relating to precision and accuracy concern the georeferencing of the reflectors, the determination of the average displacement velocity and the determination of the displacement time series.

With regard to the spatial positioning of the reflectors, the transition from coordinates in the SAR system to geographical coordinates in the WGS84 system is affected by a positioning error in the north-south direction and in the east-west direction of ±5 m. On the other hand, the error relative to the ellipsoid height of each point is estimated to be ±1.5 m.

The presence of disturbance, such as atmospheric and decorrelation noise, results in velocity measurement error of the order of ±2 mm/year.

6.2 Deformation analysis recorded in ascending geometry

The image processing was carried out using the technique of Differential SAR Interferometry, through an approach that works with radar targets (Persistent Scatterers, PS) directly visualised on the ground, allowing their possible displacement over time to be assessed.
With this approach it is therefore possible to analyse all the interferograms defined from the available image dataset, allowing analysis to be carried out on the individual pixel that shows a certain quality/stability in terms of phase.

6.2.1 Sentinel-1 analysis

Eighty-one images in ascending geometry were used from 22/01/2020 to 08/09/2022 with the Sentinel-1 sensor (Fig.6.1)

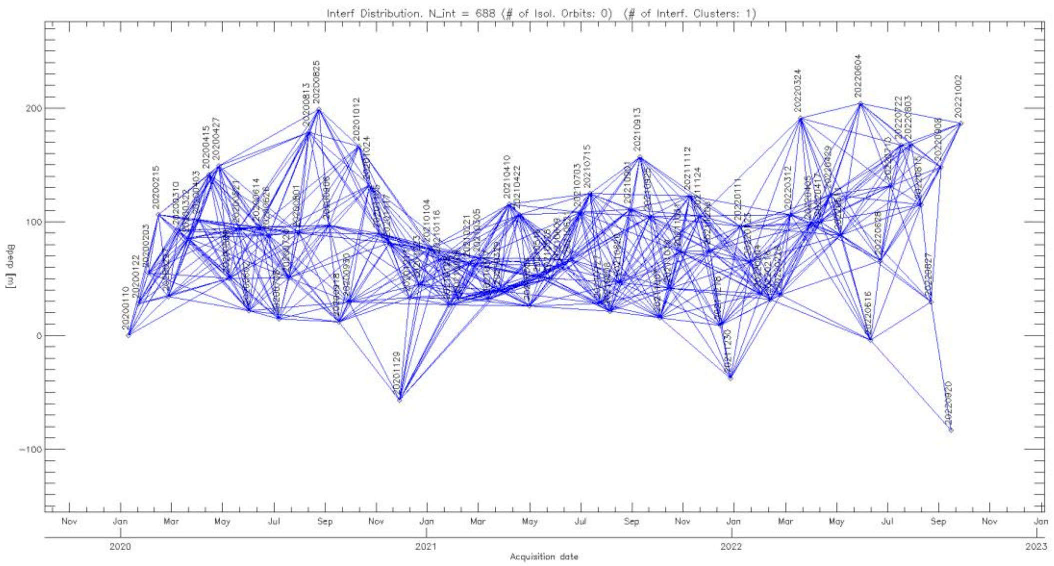

Figure 6.1: Temporal distribution of images in ascending geometry

The master image is then automatically identified by the software as the reference acquisition in order to co-register the entire image dataset. In particular, the master image turns out to be the one acquired on 16/05/202. Subsequently, the resolution image (Fig. 6.2) and the Temporal Phase

Coherence (TPC) map are obtained, which constitutes the quality parameter used for the selection of monitorable points (Fig. 6.3)

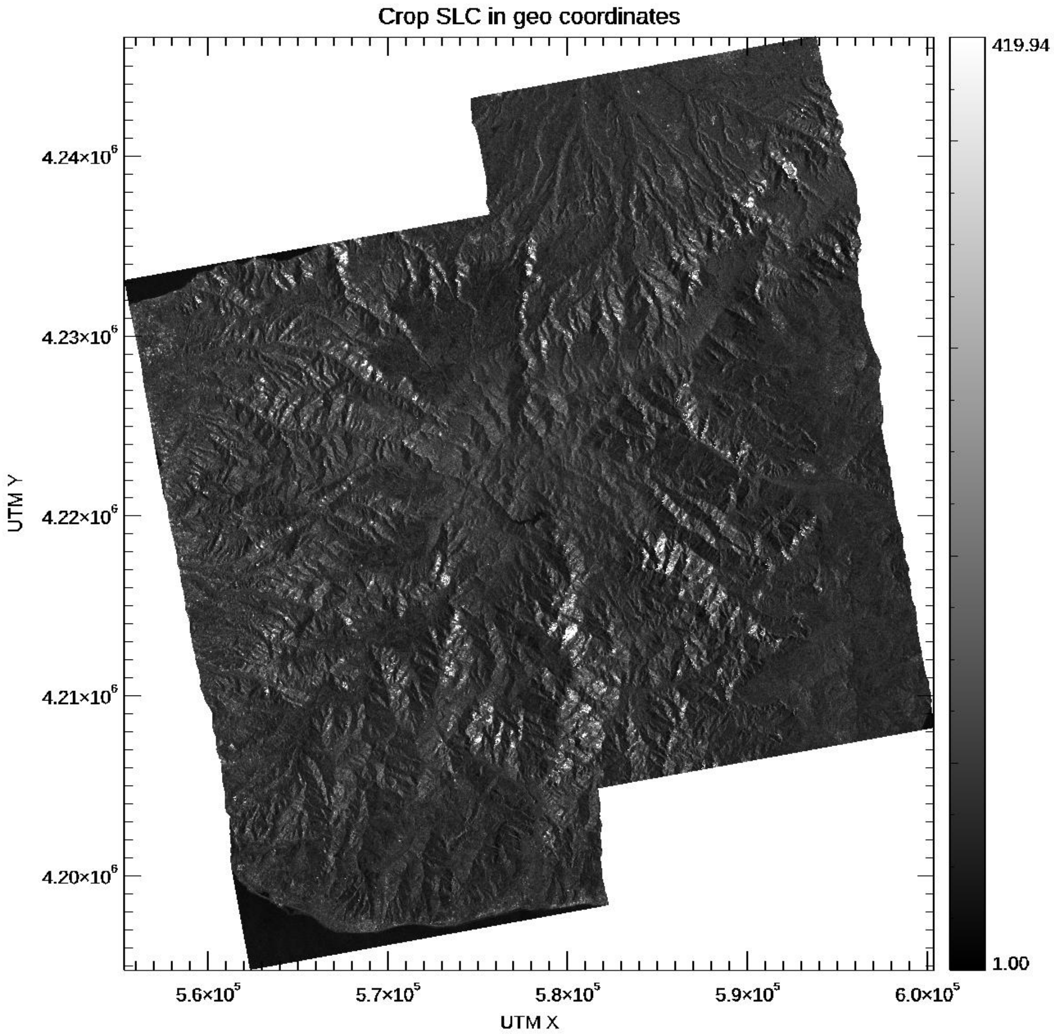

Figure 6.2: Master image acquired on 16/05/2021 in high resolution and georeferenced.

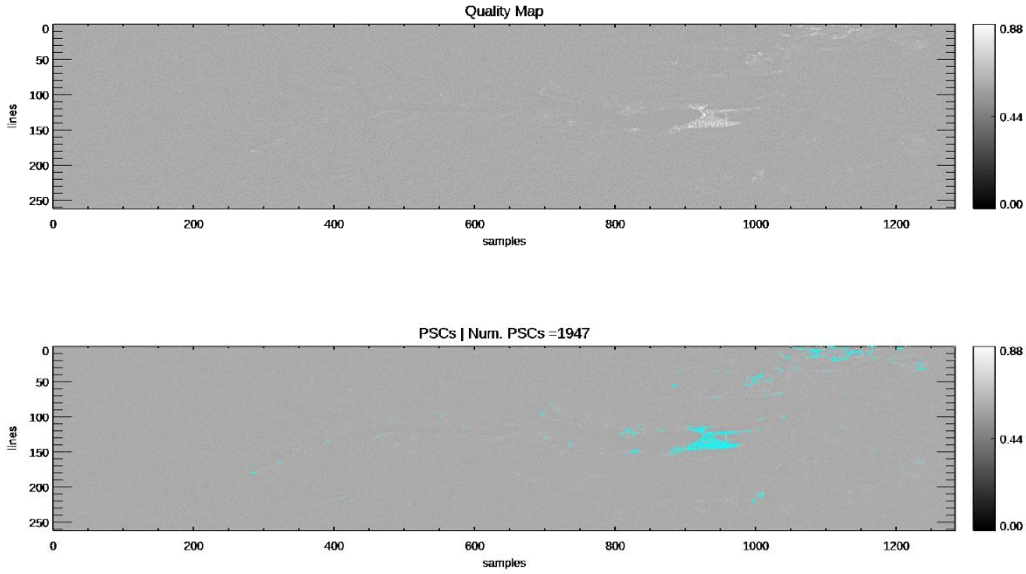

Figure 6.3: Coherent map and selection point.

6.3 Results in ascending geometry

At the end of the interferometric chain processing, the average velocity maps of the displacements along the LoS of the identified targets and the time series of the displacements were obtained for each processed, through the Persistent Scatterers approach.

It should be noted that the time series represent the cumulative displacements from the first available image, while the average velocities represent a kind of linear velocity that the model estimates for the entire acquisition interval. In addition, it should be noted that according to the commonly adopted convention, positive velocity and displacement values indicate an approach to the satellite (East-West direction for ascending geometry), while negative values indicate a departure from the satellite (West-East direction in ascending geometry) always along the LoS.

The advantage of using the DInSAR technique is that it is able to investigate large areas, therefore, from the displacement maps it is possible to analyse the behaviour of the entire reservoir and surrounding areas, unlike inclinometers that provide point indications.

As mentioned above, a double processing was carried out with both sensors, in ascending geometry.

Figure 6.4 represents the displacement map obtained with COSMO-SkyMed in the time interval from 2012 to 2019. A total of 7284 targets were identified in the area, covering only the dam body and partially the banks. Furthermore, a stability of the area is recognised, characterised by average displacement velocities along the LoS of the maximum order of 2.0 mm/year.

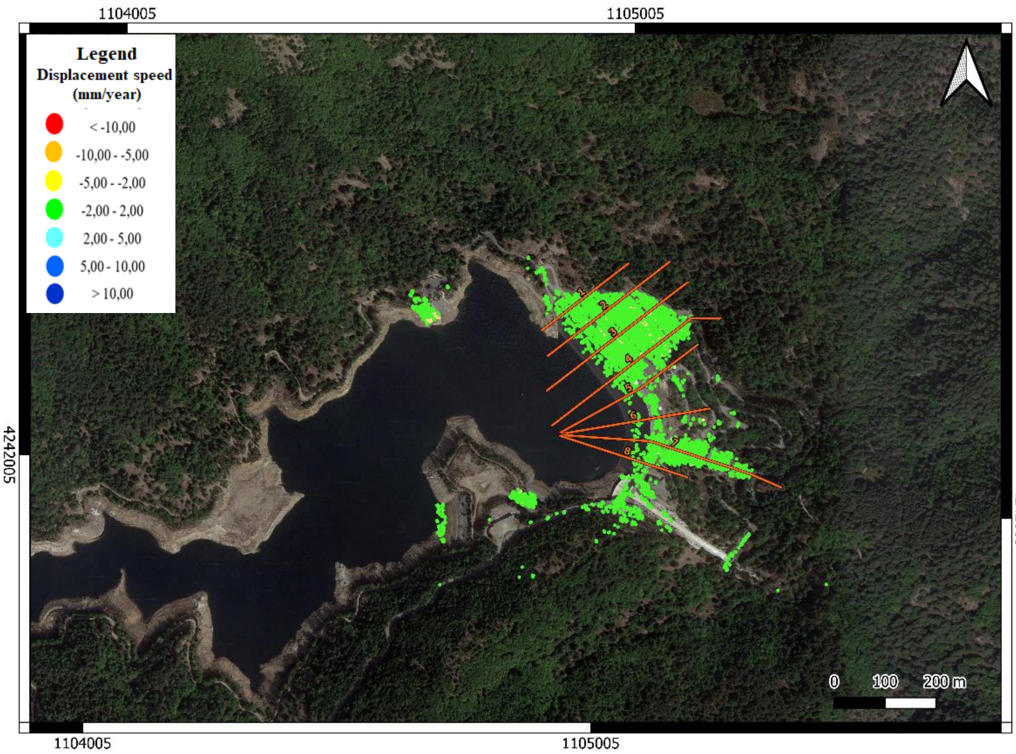

Figure 6.4: Map of the average displacement rate along the 'LoS' of targets identified in ascending geometry with the Cosmo-SkyMed sensor.

Figures 6.5 and 6.6 show the displacement maps obtained from the Sentinel-1 data processes in the periods 2015-2020 and 2020-2022, respectively. Again, an overall stability can be seen good coverage of the area in which 1135 targets in the period 2015-2020 and 1139 from 2020-2022.

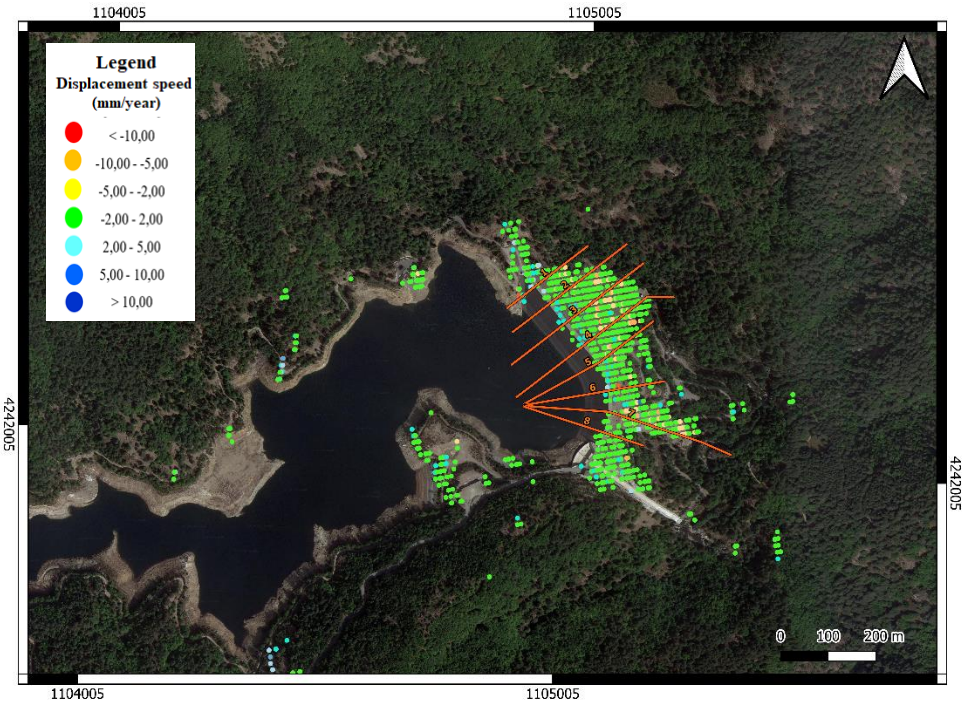

Figure 6.5: Map of the average displacement rate along the 'LoS' of targets identified in ascending geometry with the Sentinel-1 sensor from 2015 to 2020.

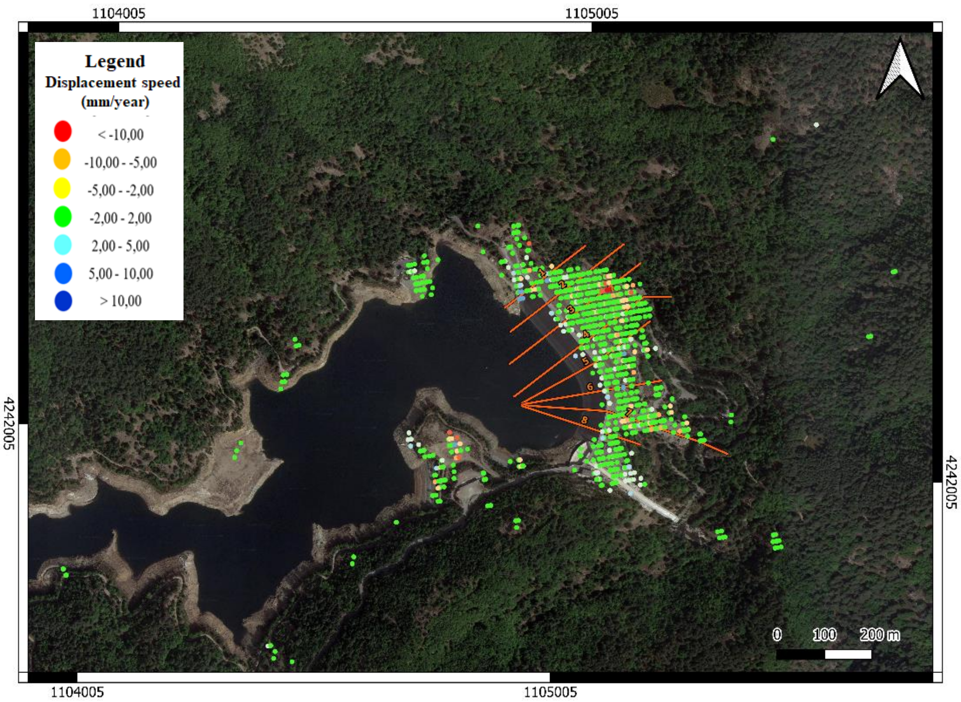

Figure 6.6: Map of the average displacement rate along the 'LoS' of targets identified in ascending geometry with the Sentinel-1 sensor from 2020 to 2022.

Thus, with both sensors, a high number of reflectors identified on the top of the embankment and the dam body confirms the high electromagnetic response; on the other hand, heavily vegetated environments are characterised by a small number of targets, making them difficult to investigate.

6.4 Results in descending geometry

Analogous to the description of ascending geometry, 111 images in descending geometry from 08/01/2016 to 27/06/2020 were processed using the Permanent Scatterer technique. The average displacement velocity map along the LoS of the identified targets shown in Figure 6.7 was obtained. As can be seen, an order of magnitude lower density of targets was obtained than those obtained in ascending geometry, about 400 in total. The targets are however located on the dam body and the top of the embankment, confirming the high electromagnetic response.

Even in this case, it should be noted that according to the convention commonly adopted, positive velocity/displacement values are to be interpreted as approaching the satellite (West-East direction in descending geometry) while negative values are to be interpreted as moving away from the satellite (East-West direction in descending geometry), always along the sensor-target line (Line of Sight, LoS).

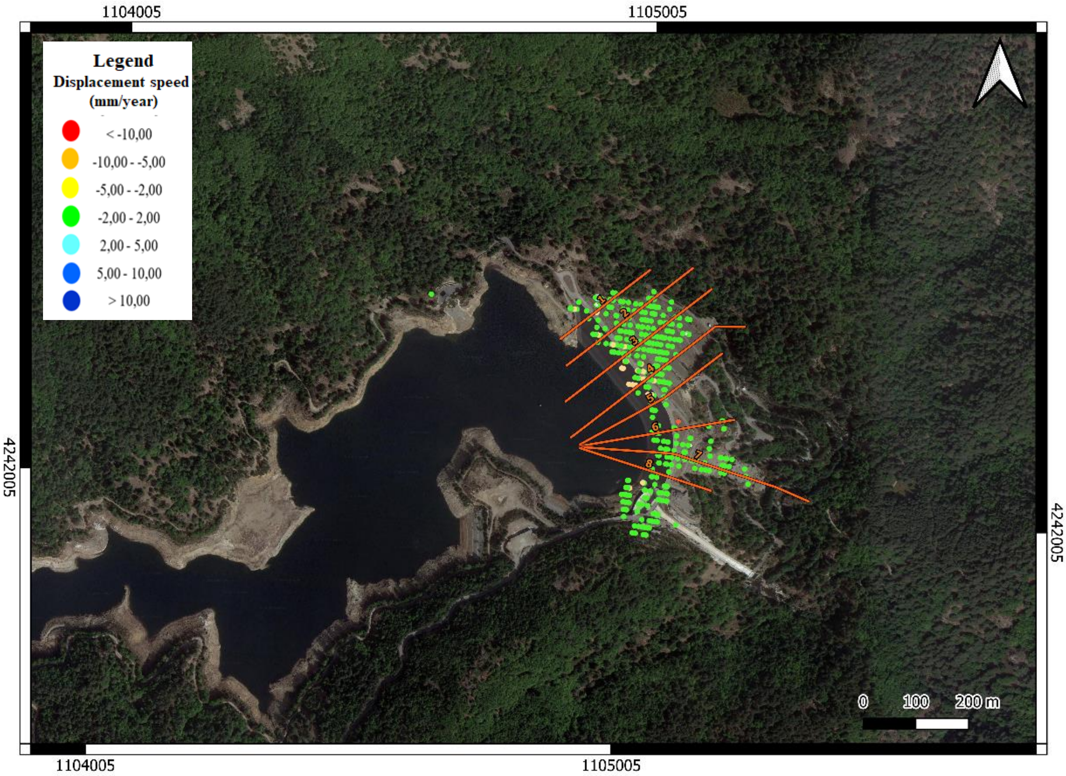

Figure 6.7: Map of the average displacement rate along the 'LoS' of targets identified in descending geometry with the Sentinel 1 sensor.

6.5 Time series analysis

In this chapter, the time series of the selected targets will be described, referring to the two phases of the dam reservoir. The displacement time series useful to evaluate the progressive evolution over time are then represented. Since the DInSAR technique allows the monitoring of large areas, the targets located along all sections of the dam were considered in order to be able to assess the general behaviour of the dam.

6.5.1 Experimental reservoir period

- *CosmoSky-Med time series*

The area was analysed with the COSMO-SkyMed sensor in ascending geometry from 25/01/2012 to 28/01/2019.

The time series of the points located on the crown along the 8 sections are shown below (Fig. 6.8).

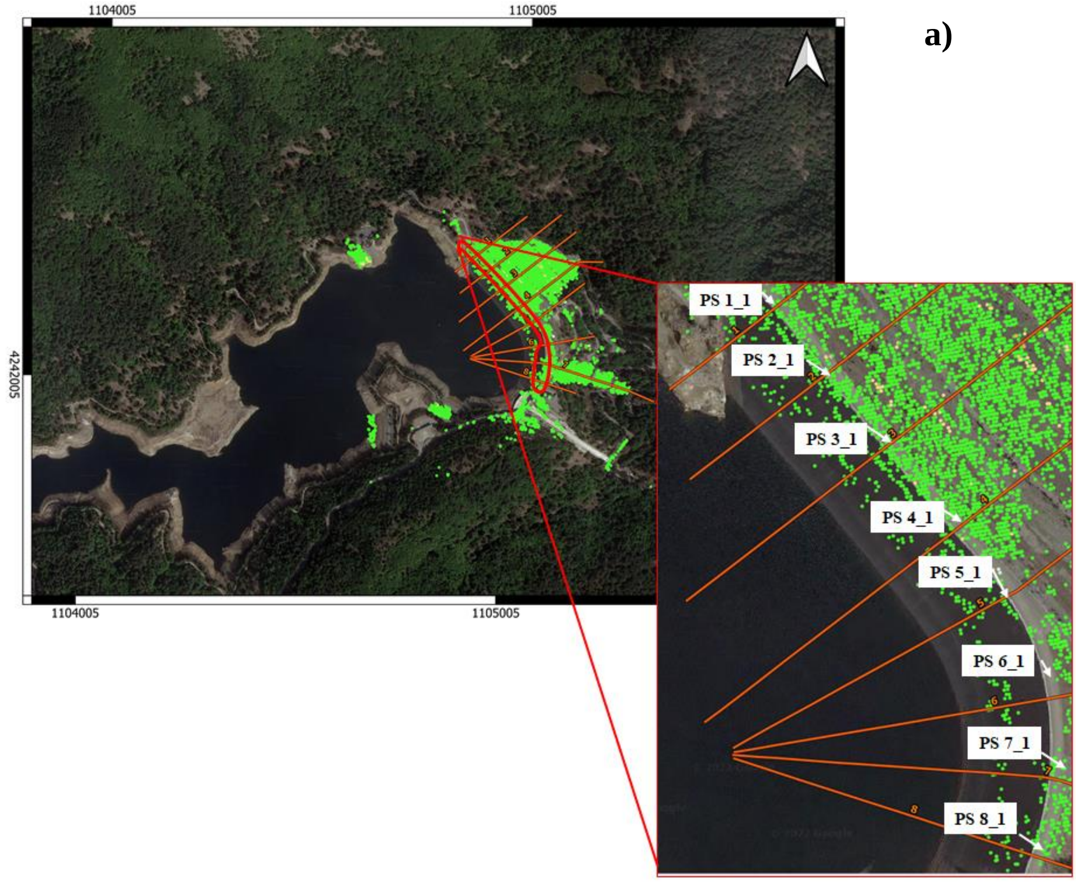

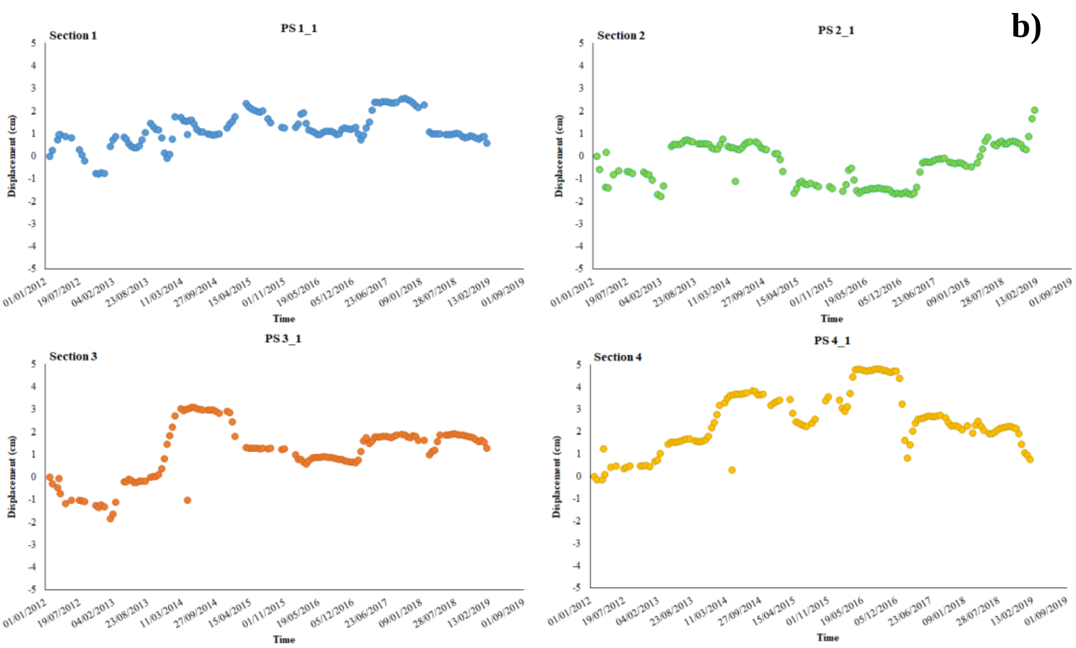

Figure 6.8: a) Focus on the top of the embankment of the ascending map of PS and zoom in on the chosen PS; b) time series of some targets on the top of the embankment along the 8 sections.

Figure 6.8: c) time series of some targets on the top of the embankment along the 8 sections.

The time series of the PS chosen along the top of the embankment, show a consistent trend. It is interesting to observe that in the analysed time interval, acceleration and deceleration periods alternate cyclically. In particular, it can be seen that from the end of 2013 to the beginning of 2014 in every PS there is an acceleration period, which reaches approximately 3.5 cm along sections 3,4 and 8. Furthermore, a period of deceleration is recognised from late 2017 to mid-2018, with maximum displacements of approximately 2.5cm along sections 4,6 and 7. Amongst the periods of acceleration and deceleration, periods of stability common to the 8 sections are evident. It should be noted that for all sections the displacement trends show the occurrence of small and insignificant displacements.

- *Sentinel-1 Time series*

The time series of selected PS on the top of the embankment, in ascending and descending geometry, are shown below (Figs. 6.9-6.11), noting that the acquisitions in ascending and descending geometry are not acquired on precisely the same days. Points directly selected in ascending geometry are indicated by 'A' and points directly selected in descending geometry by 'D'.

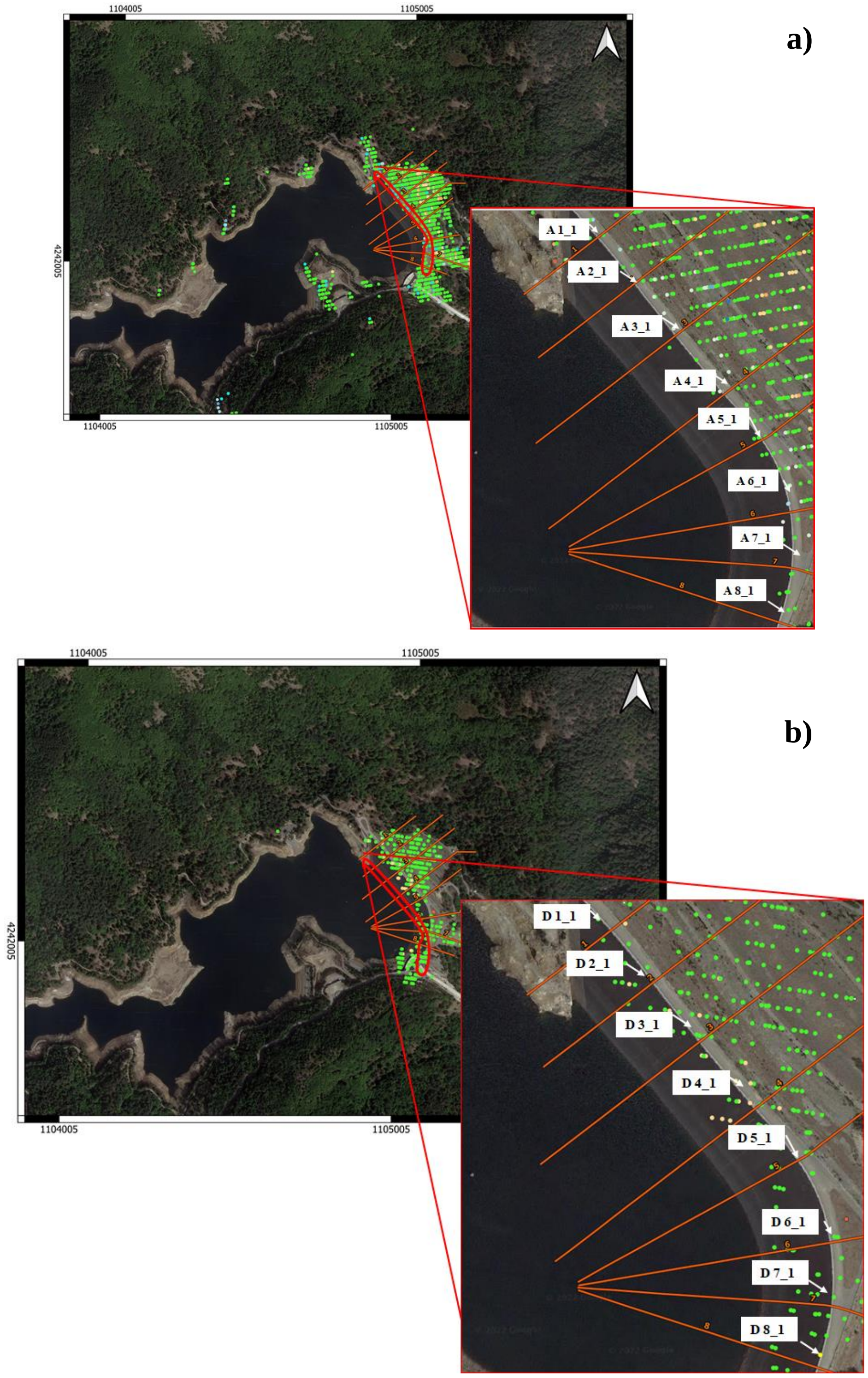

Figure 6.9: a) Focus on the top of the embankment of the ascending map of PS and zoom in on the chosen b) Focus on the top of the embankment of the descending map of PS and zoom in on the chosen.

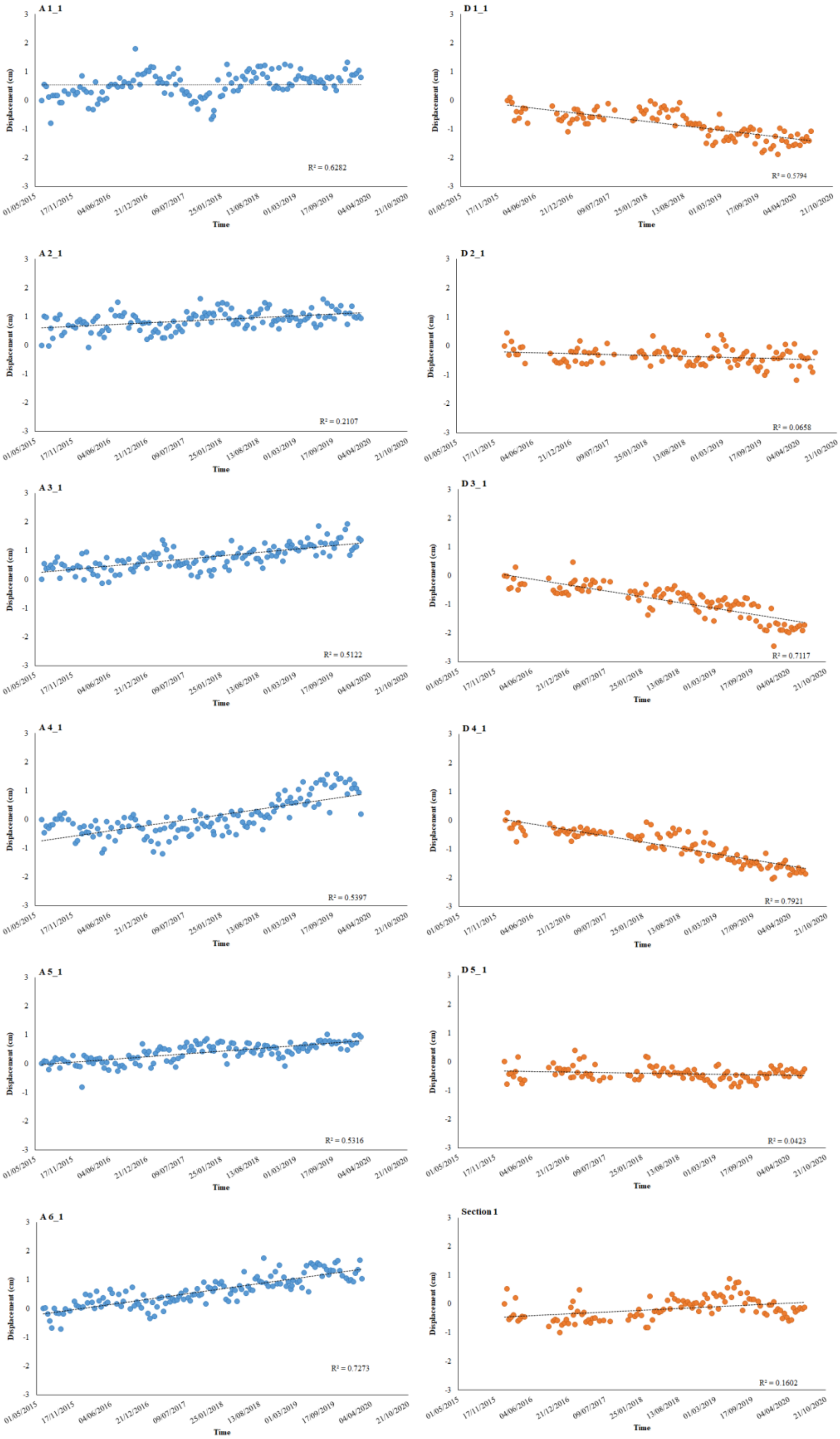

Figure 6.10: Time series of some targets on the top of the embankment along the sections 1-6 in ascending e descending geometry.

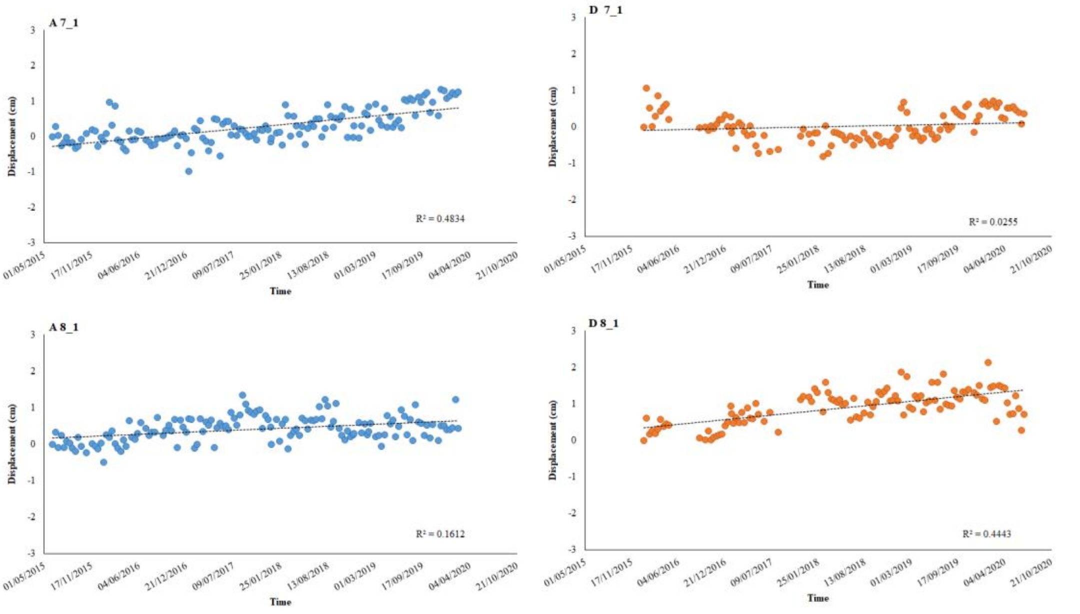

Figure 6.11: Time series of some targets on the top of the embankment along the sections 7 and 8 in ascending e descending geometry.

The PS time series located on the crown, show very low displacement rates, with a maximum value of approximately 2.0 cm occurring along sections 3 and 4, in descending geometry.

It is interesting to highlight that the analysis of the velocity profiles show an almost linear trend of deformation with a sometimes very strong linear correlation (R^2 values) in ascending geometry. This trend is also evident in descending geometry along sections 1, 3 and 4. Therefore, the selected PS are characterised by periodic accelerations and relative decelerations.

A few points were also selected along the second berm of the dam body, in both geometries except for section 5 as no points materialised in descending geometry. Their location on the map (Figs. 6.11a) and b)) and the time series are shown below (Fig. 6.12).

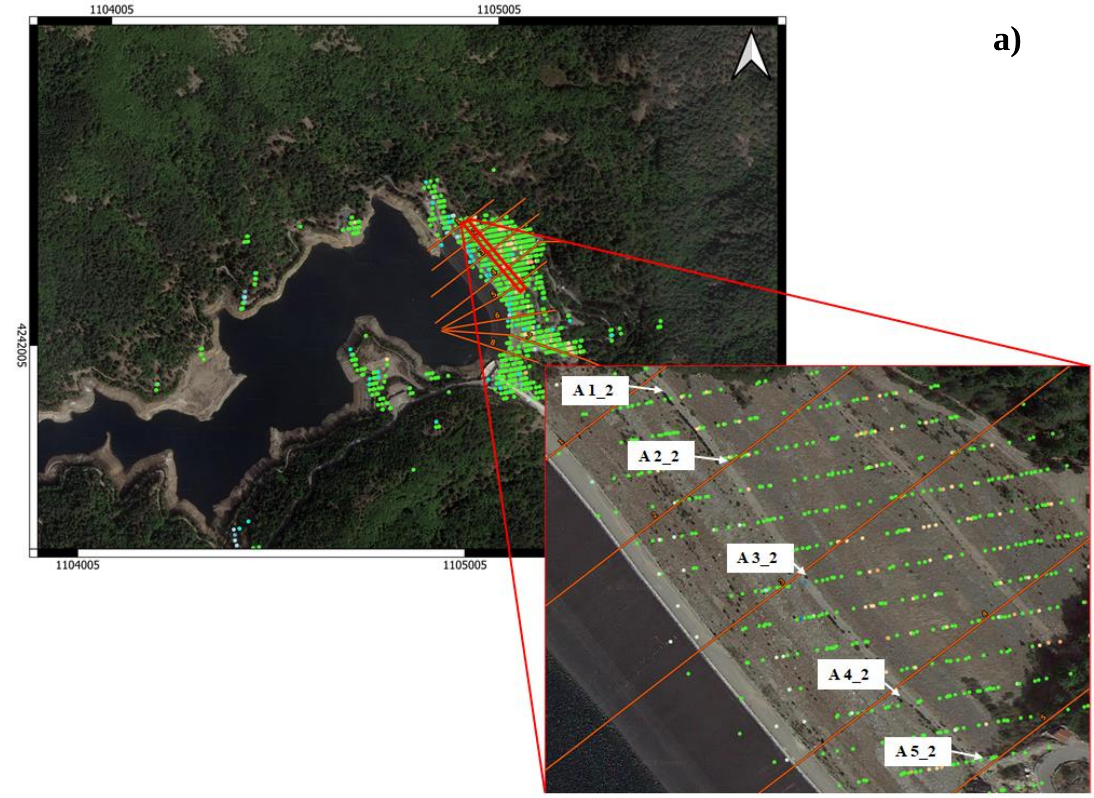

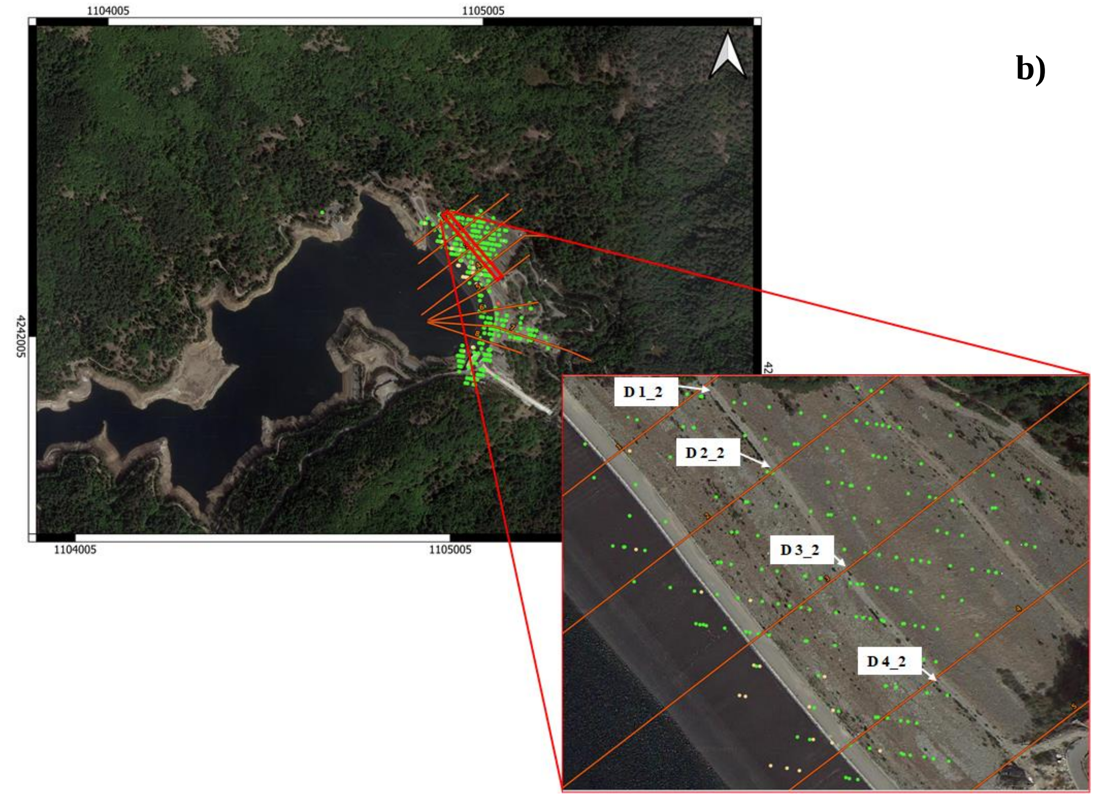

Figure 6.11: a) Focus on the second berm of the ascending map of PS and zoom in on the chosen b) Focus on the second berm of the descending map of PS and zoom in on the chosen

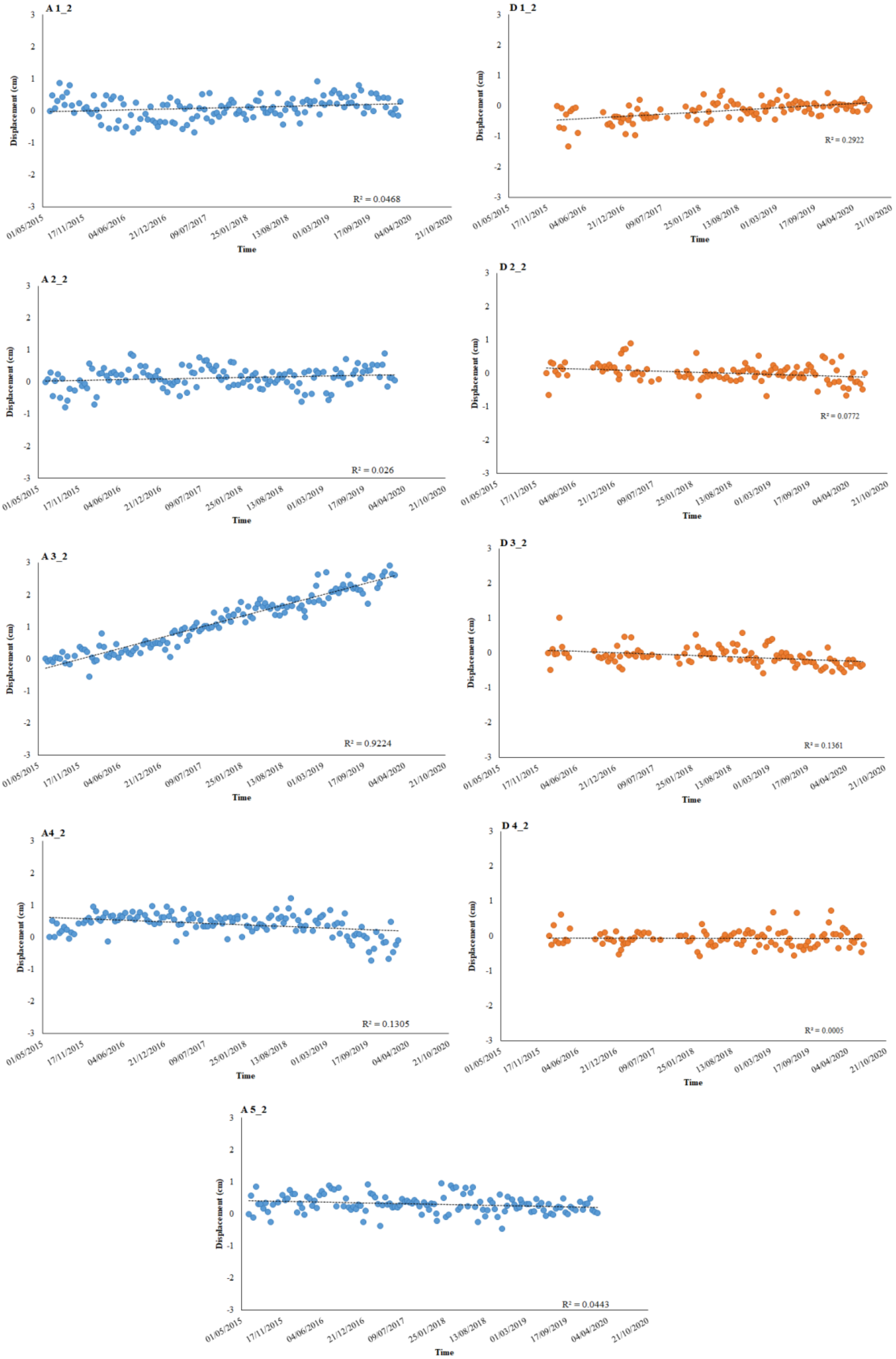

Figure 6.12: Time series of some targets on the second berm along the sections from 1 to 5 in ascending e descending geometry.

The time series show a particularly stable situation, with maximum displacement values of around 1cm. In contrast to the points located on the top of the embankment, the R^2 values are very low except for point A3_2 along section 3. In fact, point A3_2 presents a linear trend and constant acceleration over time, showing an increase in cumulative displacement of approximately 3cm.

6.5.2 Operating reservoir period

Monitoring was implemented until 2022 in ascending geometry with the Sentinel 1 satellite, during the dam's operational period. The time series from 2019 to 2022 considering the previously described points are shown below (Figs. 6.13 and 6.14).

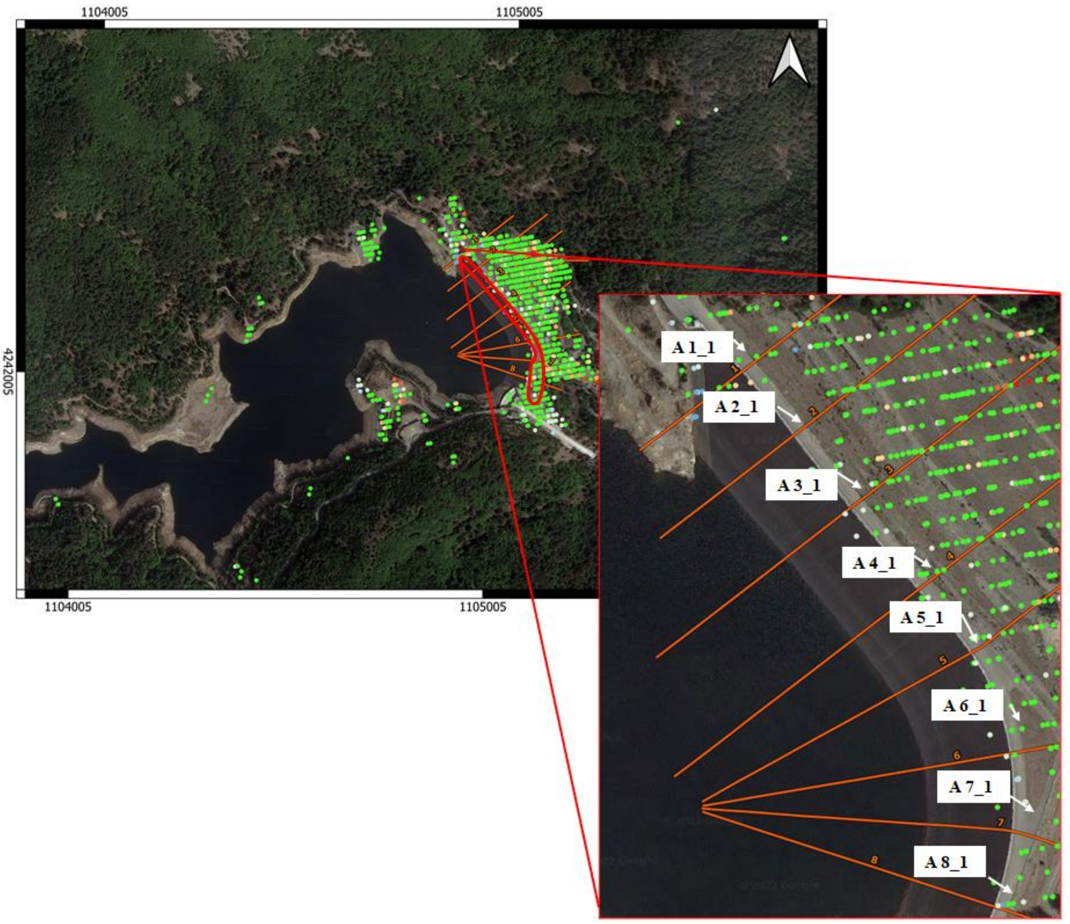

Figure 6.13: Focus on the top of the embankment of the ascending displacement map of PS and zoom in on the chosen in the period from 2019 to 2022.

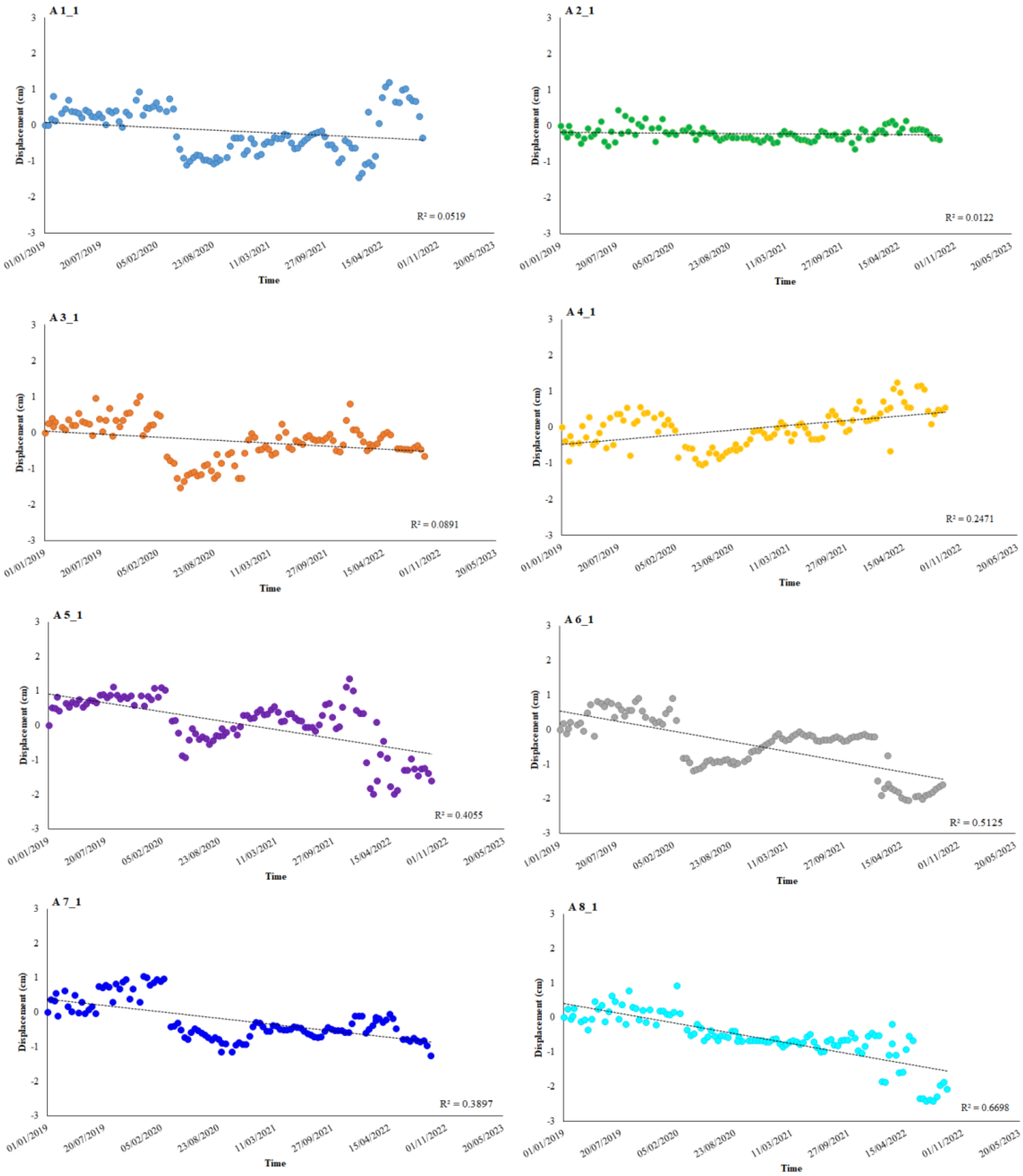

Figure 6.14: Time series of some targets on the top of the embankment along the sections in ascending e geometry from 2019 to 2022.

The analysis carried out on the top of the embankment during the dam's operational period shows interesting aspects common to all sections. In particular a rapid deceleration from February 2020 to April 2020 is evident in all sections with the exception of 2 and 5. Even in this period, phases of rapid acceleration and deceleration are evident, spaced out by periods of stability. The trend appears rather linear represented by rather high R2 values.

It can also be seen that points A5_1, A 6_1 and A8_1 reach maximum displacement values of approximately 2.5cm during the phase of rapid deceleration observed from January 2022 to February 2022.

Focusing on the second berm instead (Figs. 6.15 and 6.16), a rather stable trend with maximum displacement rates of 1cm is evident. It can also be seen that along sections 1 and 2, the points show a rapid acceleration from January 2022 to April 2022; on the other hand, a deceleration can be seen along sections 3 and 4 during the same period. The point along section 5 was not shown as it did not realise.

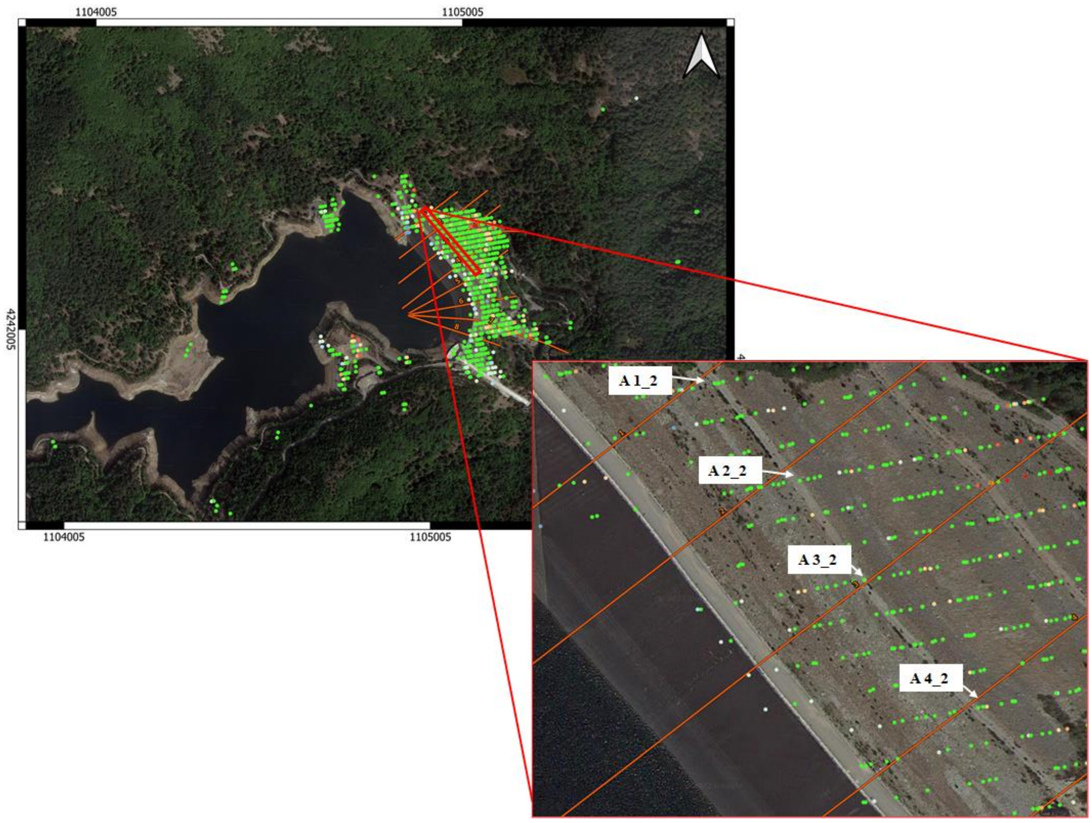

Figure 6.15: Focus on the second berm of the ascending map of PS and zoom in on the chosen

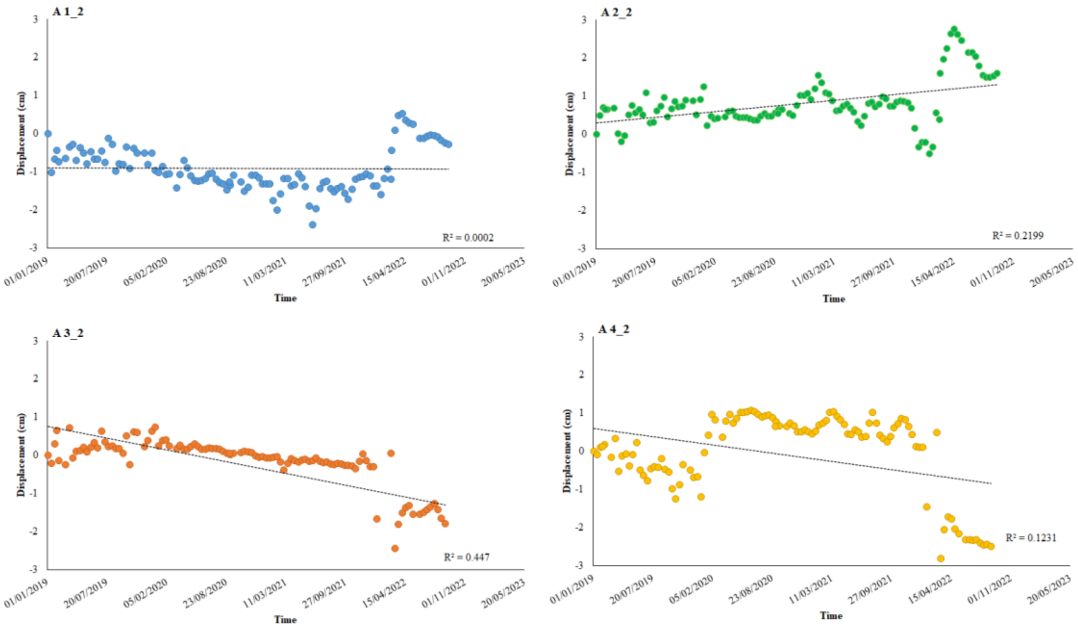

Figure 6.16: Time series of some targets on the second berm along the sections in ascending geometry from 2019 to 2022.

6.6: Results interpretation

The time series analysis of the satellite data reveals a dam behaviour comparable to the inclinometer measurements.

The integration of a multi-band analysis with X-band and C-band sensors was useful to obtain a high point density. It is highlighted and confirmed that the morphology of the terrain and a good orientation of the dam guarantee the presence of a good number of reflectors even if the density is very different both for ascending and descending geometry acquisitions and for the use of different sensors.

It is important to mention that positive displacement values mean an approach to the satellite, while negative values are to be interpreted as a departure from the satellite, always along the sensor-target junction (Line of Sight, LoS). In addition, displacement values with opposite direction in the two distinct geometries characterise a motion with a predominant component in the horizontal plane, while in the case where the sensor detects a displacement with concordant direction in both sight geometries, the motion is characterised by a predominant component in the vertical direction.

On the basis of these important considerations, the interferometric products obtained from the processing of the COSMO-SkyMed images show a very similar behaviour along the top of the embankment, with coincident acceleration and deceleration phases.

In order to better understand these phases, the displacement trends of the selected PS are compared to the trend of the reservoir level from 25/01/2012 to 28/01/2019 (Fig. 6.17) corresponding mainly to the experimental reservoir.

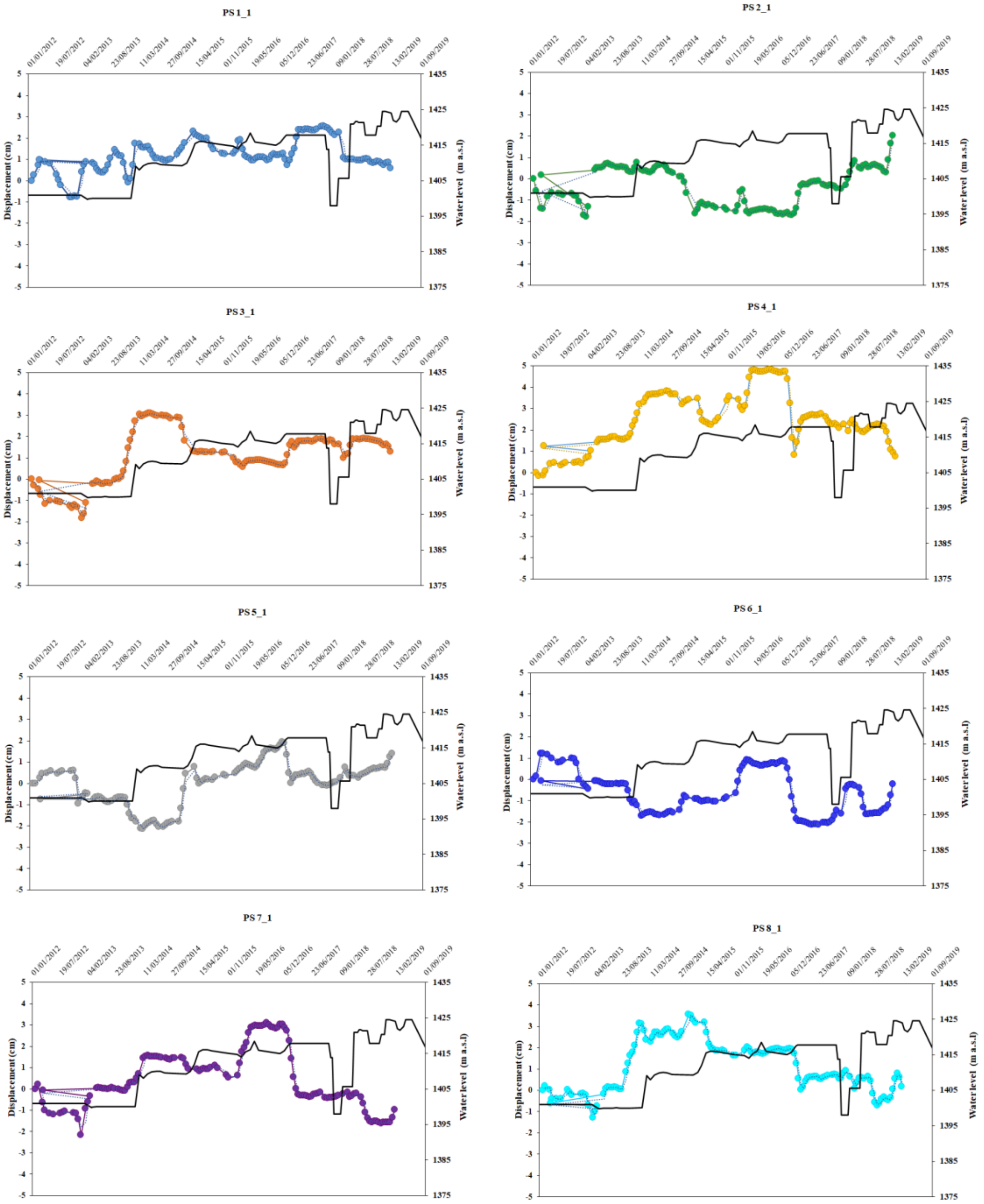

Figure 6.17: time series of COSMO-SkyMed targets selected compared to water level (black curve)

It is known that the reservoir level represents an acting force perpendicular to the dam. Comparison of the trends shows that, during stationary phases of the reservoir level correspond a stable displacement along the LoS, particularly during long time intervals, as in 2014 and 2017. It is also evident that the phases of acceleration and deceleration occur with a slight delay compared to the strong variations in flooding and emptying.

Analyses carried out Sentinel-1 in both geometries in the period from 2015 to 2019, coinciding with the experimental reservoir phase and the beginning of the operational phase, show a predominantly horizontal displacement component for the points located on the crest along almost all sections, except for the sections 6, 7 and 8, which show a vertical component. Along section 4, until 2018 both geometries show a concordant trend, after which a strongly divergent trend, as does section 3. These trends are consistent with the displacement that is expected in relation to the reservoir level. Figure 6.18 shows the trends of the selected points, ascending points in blue and descending points in orange.

The selected points along the second berm, on the other hand, show a consistent trend in both geometries, representing a predominantly vertical displacement component, unaffected by the change in the reservoir level.

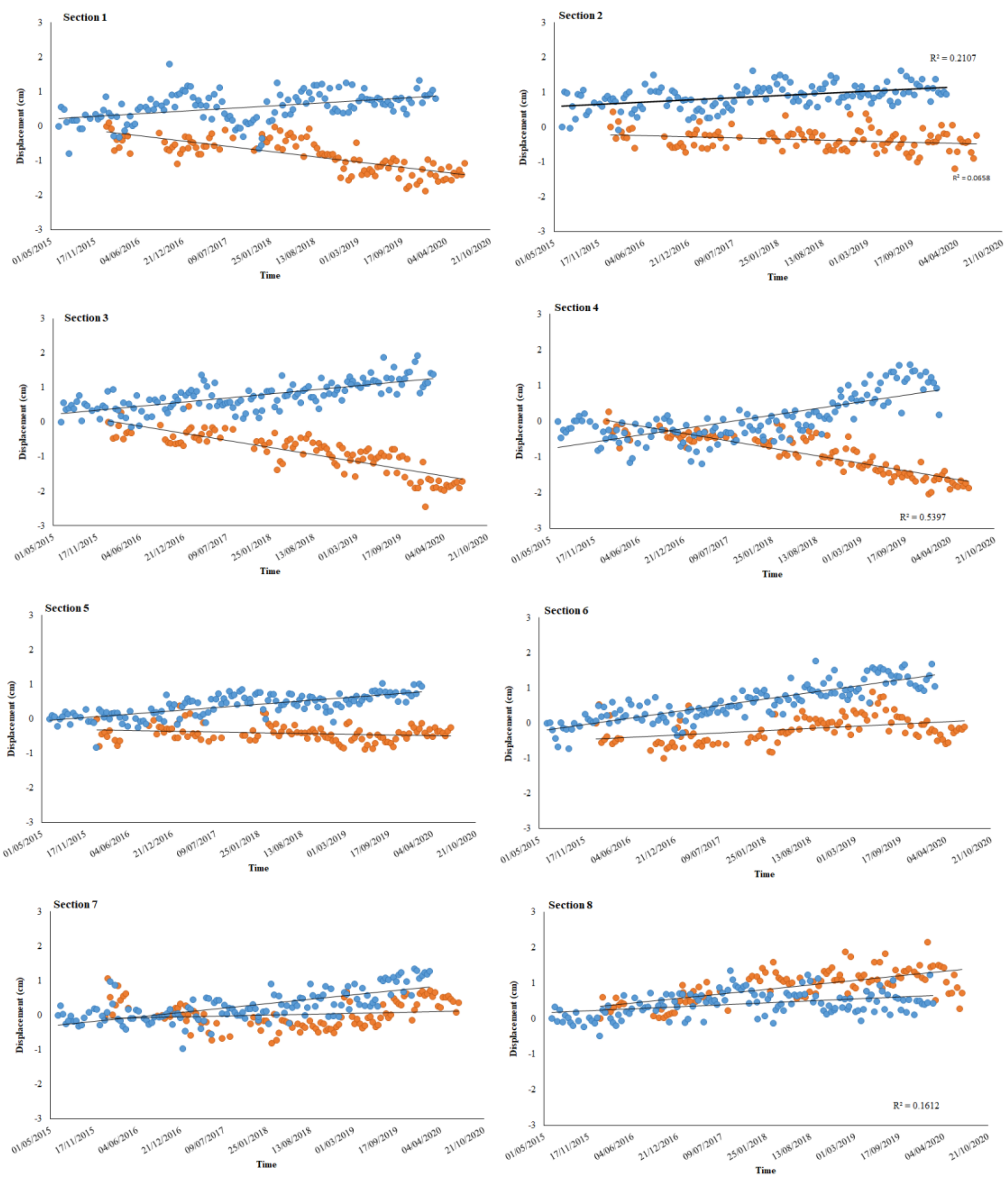

Figure 6.18: Time series of Sentinel 1 targets on the crown in ascending (blu points) and descending (orange point) geometry.

Figure 6.19 shows the trends in ascending and descending geometry for the experimental reservoir period correlated with the reservoir level. It is very interesting to note that, along sections 1, 3 and 4 the displacement trends are stable from 2015 to June 2017 the displacement trends along the LoS are stable, consistent with that of the reservoir level which remains fixed at 1415 m a.s.l. From that period onwards an evolution in the trends can be seen.

In detail:

- along section 1 the PS in ascending geometry (blue dots) show a deceleration while the PS in ascending geometry shows an acceleration, consistent with the period of maximum dam discharge. Since 2018, there has been an acceleration in ascending geometry and deceleration in descending geometry at about 1422 m a.s.l.;

- along sections 3 and 4, there is an acceleration in ascending geometry and deceleration in descending geometry since the period of maximum discharge (June 2017).

Along the other sections, the trends are stable and do not show any significant variation with the reservoir level.

Instead, Figure 6.20 shows in ascending geometry only the PSs located on the top of embankment during the period of the operational phase in relation to the reservoir level.

As in the previous phase (Fig. 6.19), a different trend can be observed along sections 1,3 and 4. In contrast, however, also along sections 5, 6, 7 and 8.

In all the trends, a deceleration is evident from September2019 until March 2020, probably related to the previous period of emptying that began a few months earlier, with a change in the reservoir level of approximately 10 m. in the following interval, an acceleration of the PS is recognisable, reaching approximately 1 cm, probably corresponding to the later phases of emptying.

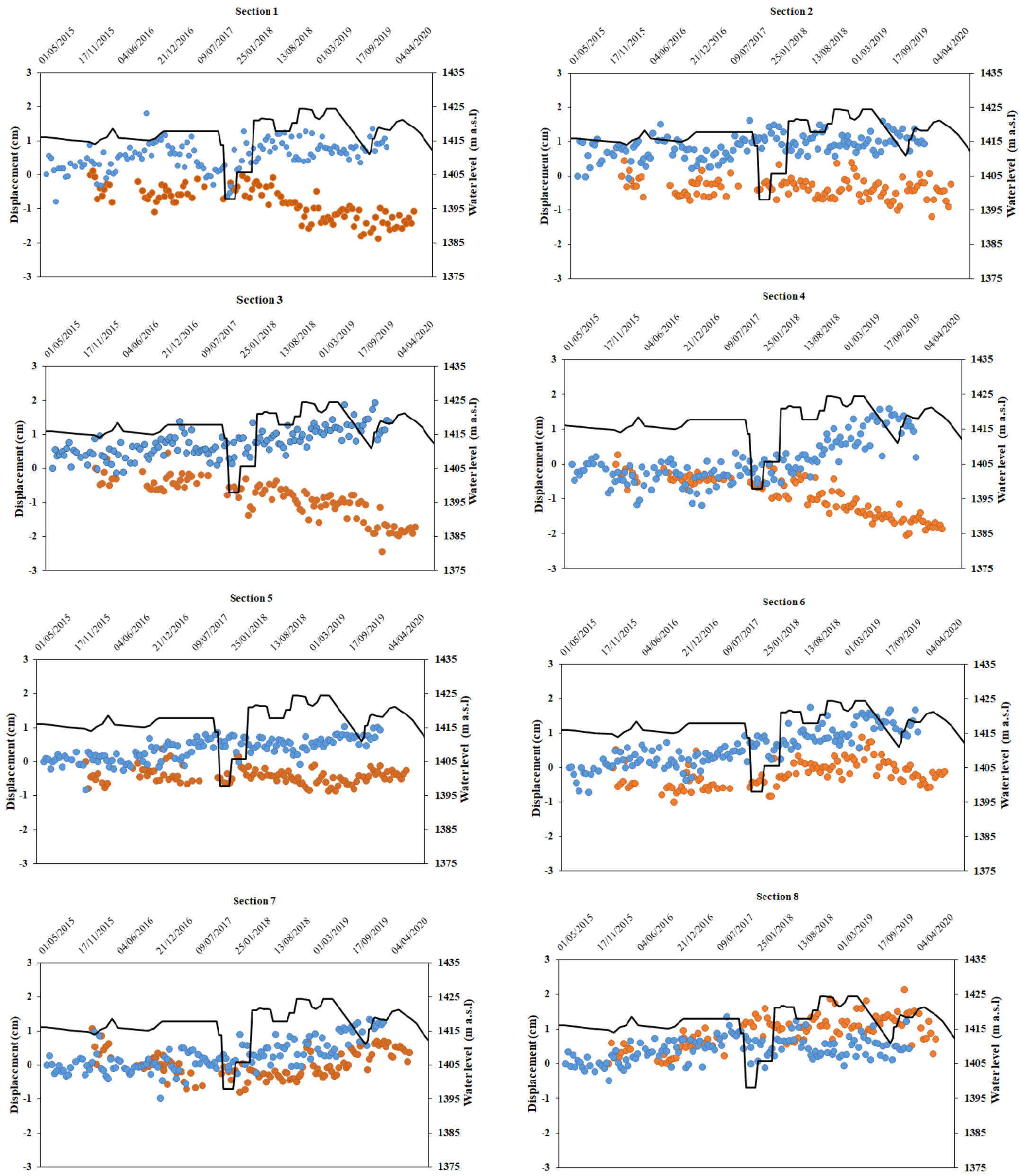

Figure 6.19: Time series of Sentinel 1 targets selected during the experimental phase compared to water level. The blue dots represent PS in ascending geometry and the orange dots in descending geometry.

\

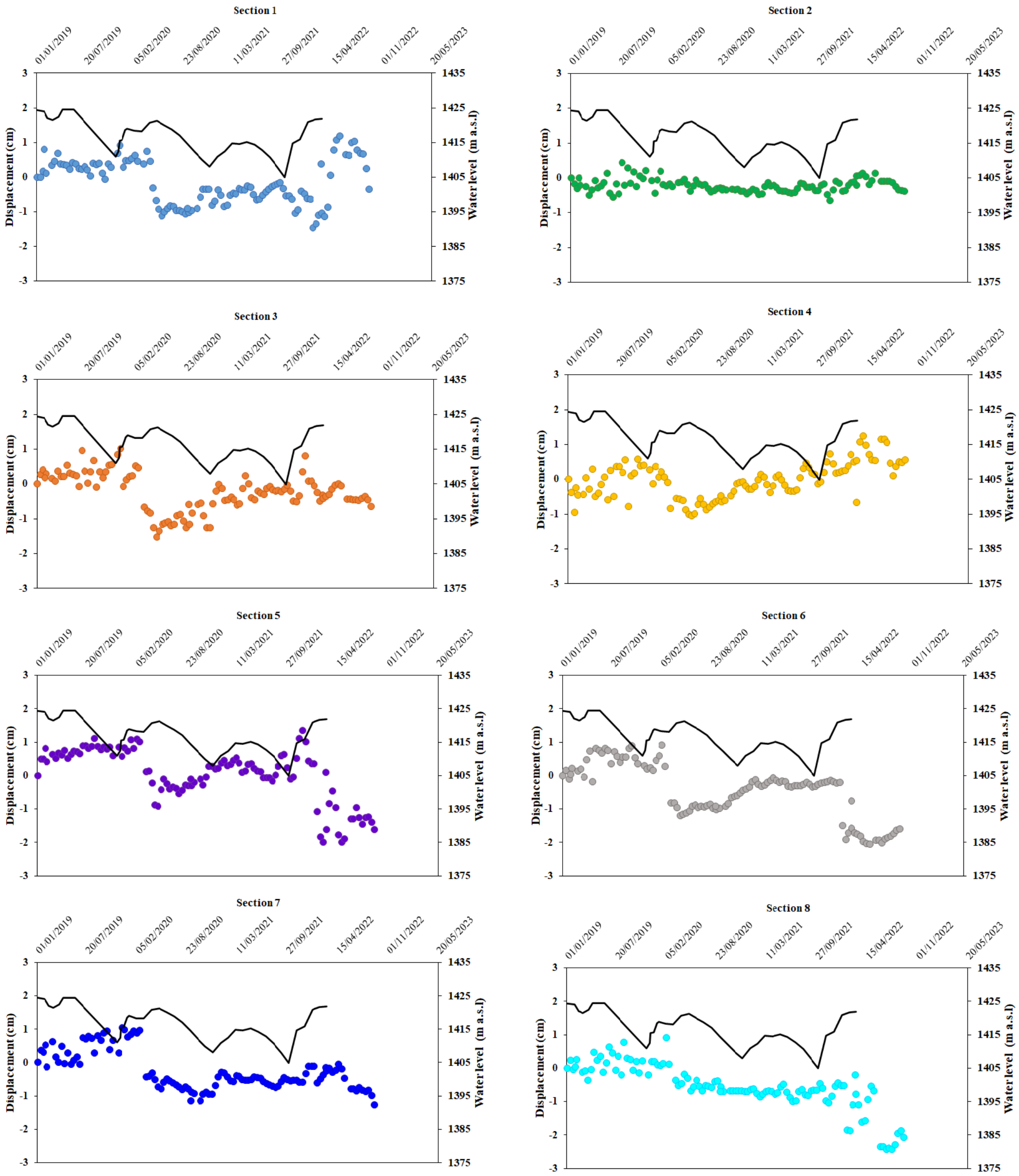

Figure 6.20: Time series of Sentinel 1 ascending targets selected during the operational phase compared to water level.

Chapter 7

Inclinometer data vs satellite data

7.1: Satellite and inclinometer data comparison

The combined use of satellite data and in-situ measurements provides support for the monitoring and data validation activities of an integrated monitoring system.

Therefore, a comparison was made with the inclinometer measurements at sections 3 and 4 during the common acquisition period.

For the comparison, the Sentinel 1 sensor was used in ascending and descending geometry in the common acquisition period, i.e:

- from June 2015 to July 2022 in ascending geometry

- from February 2016 to October 2019 in descending geometry.

To do this, ground deformations recorded by the inclinometers have been projected along the LoS of satellites according to the following equation:

$$S_{LoS} = - S\ sen\theta\ \cos(\alpha-\gamma)$$

where S is the ground displacement recorded by the inclinometer, θ is the satellite incidence angle (equal to 41° for ascending geometry and 43° for descending geometry products employed), α is the inclinometer azimuth angle measured during the field acquisition and γ represents the heading angle (i.e., satellite azimuth angle).

7.2 Results

The SPs in the immediate surroundings of the inclinometers in both geometries, both on the crowning and on the second berm, were chosen.

The inclinometer TIV 1 is located on the crowning of section 3 and points A3_1 and D3_1 are in the immediate proximity (Fig. 7.1)

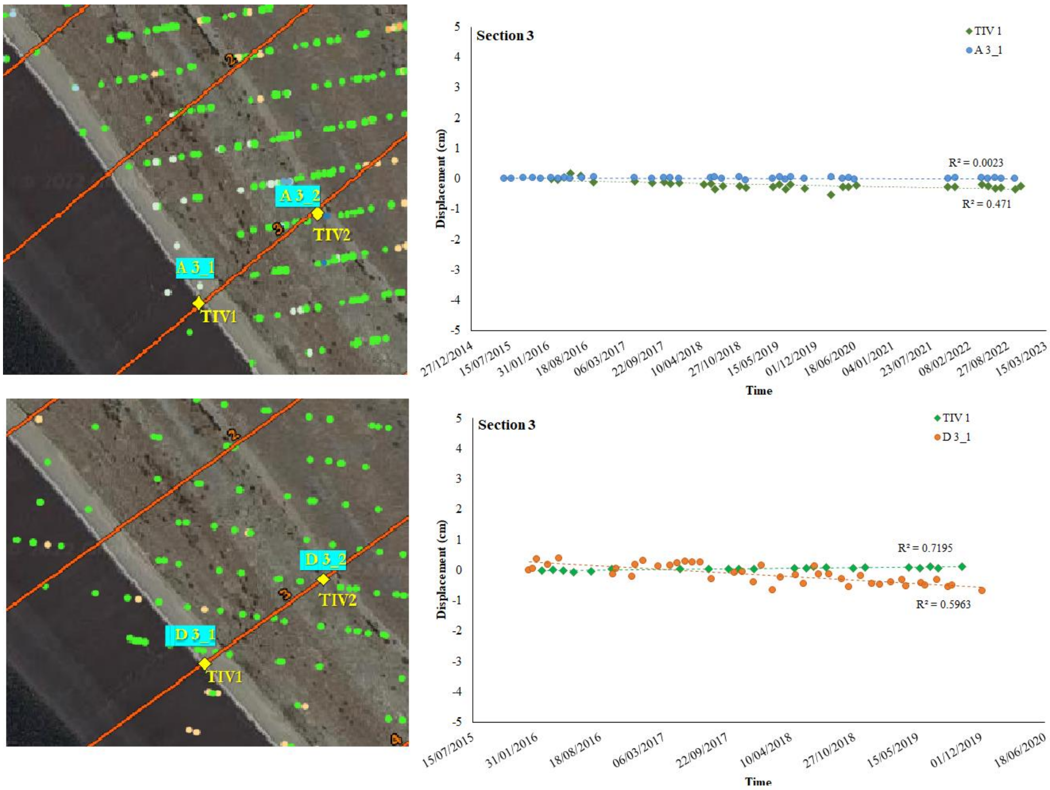

Figure 7.1: In situ measurements projected along the LoS of the satellite (green diamonds) and comparison with the time series of A3_1 (top) and D3_1(bottom) included in the ascending and descending dataset respectively.

The projected inclinometer measurements show a good fit to the overlapping time in terms of displacements with the time series considered.

Fig. 7.2 shows the comparison with the TIV 2 inclinometer located along the second berm with points A3_2 and D3_2 in ascending and descending.

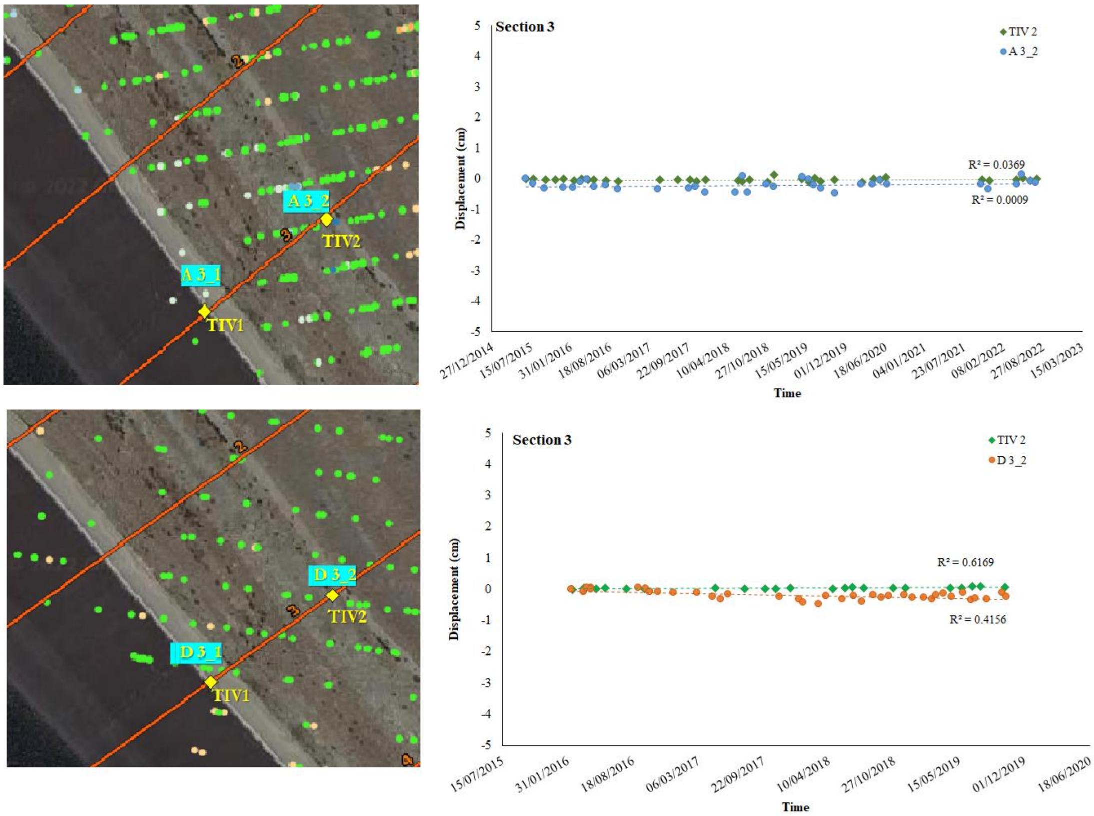

Figure 7.2: In situ measurements projected along the LoS of the satellite (green diamonds) and comparison with the time series of A3_2 (top) and D3_2 (bottom) included in the ascending and descending dataset respectively.

Again, the inclinometer data show consistency with the PS displacements.

TIV 3 located on the top embankment of section 4, is compared with the points A4_2 and D4_2 in ascending and descending geometry respectively (Fig. 7.3). However, in both geometries there is overlapping of the displacements, but as of 2018 there is an acceleration with a deviation of approximately 1.5 cm.

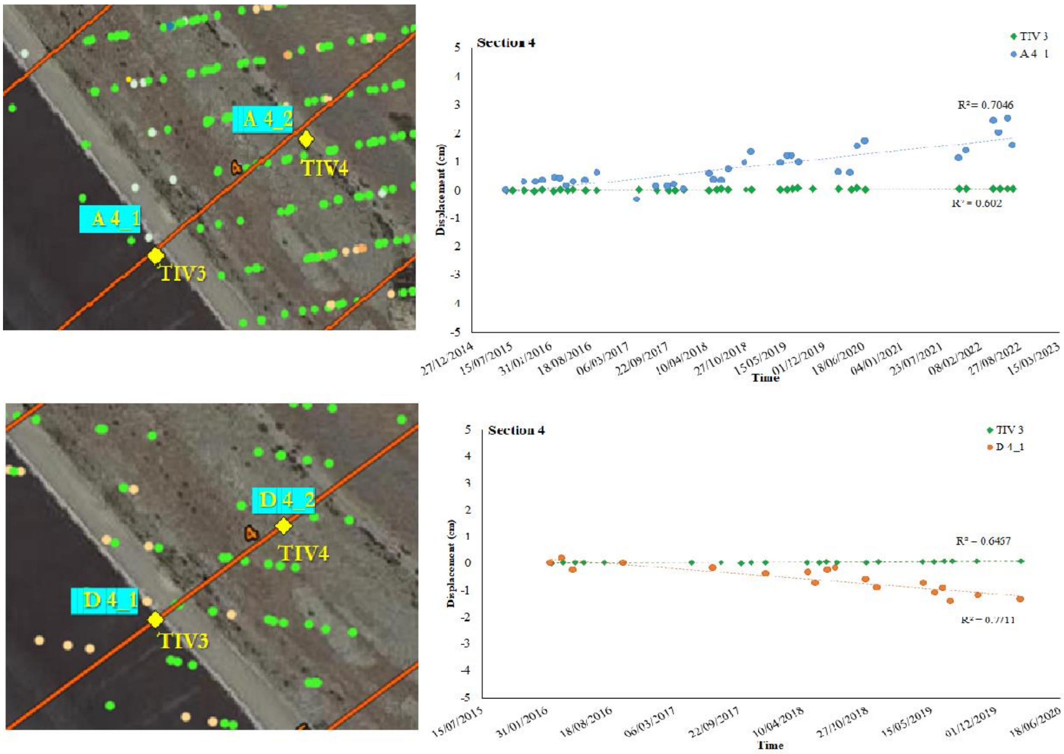

Figure 7.3: In situ measurements projected along the LoS of the satellite (green diamonds) and comparison with the time series of A 4_1 (top) and D 4_1 (bottom) included in the ascending and descending dataset respectively.

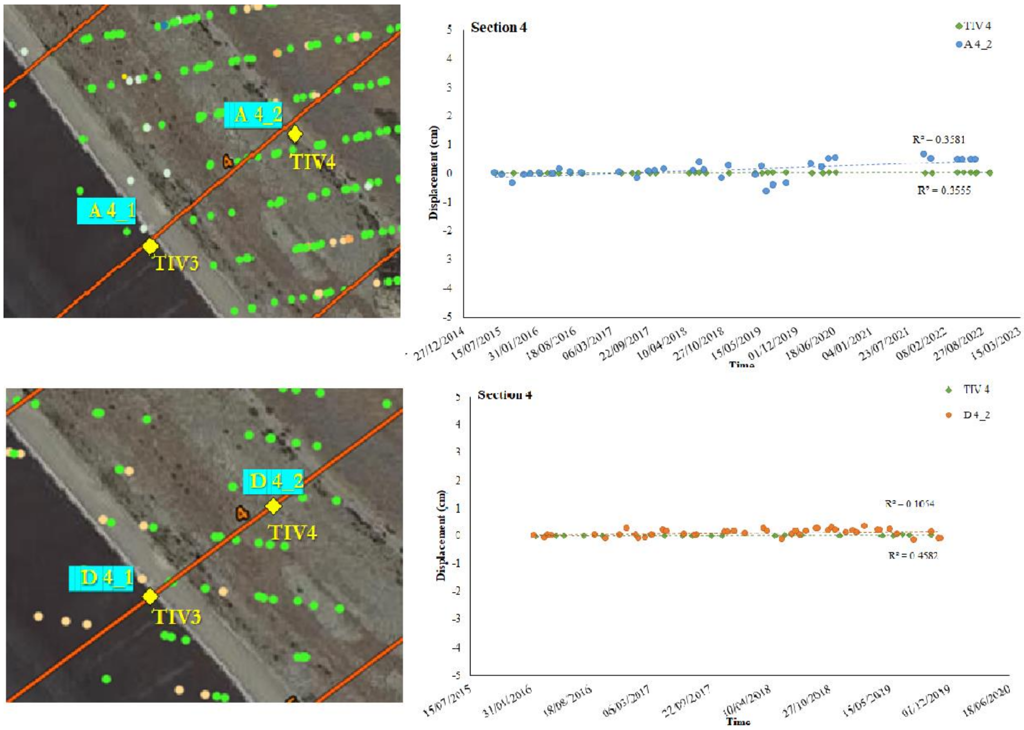

Figure 7.4: In situ measurements projected along the LoS of the satellite (green diamonds) and comparison with the time series of A 4_1 (top) and D 4_1 (bottom) included in the ascending and descending dataset respectively.

The inclinometer and satellite data comparison confirms a stability of the dam over the time considered for all sections. Only along section 4 is a variation of approximately 1 cm between the inclinometers and the PS. It is important to emphasise that the displacements are however small, confirming the substantial stability of the area.

Chapter 8

Conclusion

The aim of this thesis was to monitor the Menta Dam, located in southern Italy, by comparing innovative and conventional techniques. In particular, a monitoring of approximately 10 years was conducted, from 2011 to 2022, including the period of experimental reservoir and dam operation. Therefore, the displacement analyses were divided into two time intervals: from 2011 to 2018 corresponding to the experimental reservoir period and from 2019 to 2022 corresponding to the operating period.

The results obtained show very clear and consistent evidence on the behaviour of the dam. In particular, the inclinometer data underline a different behaviour of the dam between the crest and the downstream berms. In fact, displacements in time of the maximum order of 0.5 cm occur along sections 3 and 4 at inclinometers TIV1 and TIV 3. On the contrary, the other inclinometers do not indicate significant displacements, supporting the fact that the dam is essentially affected by horizontal displacements due to the pressure of the reservoir level on the upstream face.

The satellite data confirms the elastic behaviour of the dam, especially during the reservoir and outflow phases, corresponding to the satellite's approach and departure. Moreover, the satellite data present a trend that is fully comparable with the level of the reservoir.

This study lays the foundations to be able to apply such monitoring to dams and infrastructures in general, making it possible to optimise time and costs for monitoring large works. This research provides the basis for further extending and integrating the dam's monitoring during the operational phases. In particular, corner reflectors are being designed to be installed in the immediate neighbourhood of the inclinometers, so as to be able to acquire data with both Sentinel and CosmoSkyMed satellites, in both geometries, in order to have fixed points. In addition, other types of monitoring analysis by drone and laser scanner can certainly provide insight at different scales into the health of the dam over time.

References

- Adamo, N., Al-Ansari, N., Sissakian, V., Laue, J., & Knutsson, S. (2021). Dam Safety: Use of Instrumentation in Dams. Journal of Earth Sciences and Geotechnical Engineering, 11(1), 145-202.
- Altinbilek, D. (2002). The role of dams in development. In Water Science and Technology (Vol. 45, pp. 169–180). https://doi.org/10.1080/07900620220121620
- American Society Of Civil Engineers (ASCE 1891) - Report of the Committee on the Cause of the Failure of the South Fork Dam. In: Transactions, Vol. XXIV, n. 477, June 1891. Ed. ASCE - New York, 1891, pagg. 431-469.
- Amodio-Morelli, L., et al. (1976), L'Arco Calabro-Peloritanio nell'orogene Appenninico-Maghrebide, Mem. Soc. Geol. Ital., **17**, 1– 60.
- Arenillas parra, Miguel - Obras hidráulicas romanas en Hispania. In: Actas del I Congreso: Las obras públicas romanas en Hispania. Ed. Colegio de Ingenieros Técnicos de Obras Públicas - Madrid, 2002, pagg. 107-136.
- Atzori, P., Del Moro, A., & Rottura, A. (1990). Rb/Sr radiometric data from medium-to high-grade metamorphic rocks (Aspromonte nappe) of the north-eastern Peloritani Mountains (Calabrian Arc), Italy. European Journal of Mineralogy, 2(3), 363-371.
- Baek, W. K., & Jung, H. S. (2021). Performance comparison of oil spill and ship classification from x-band dual-and single-polarized sar image using support vector machine, random forest, and deep neural network. Remote Sensing, 13(16), 3203.
- Bamler R, Hartl P (1998) Synthetic aperture radar interferometry. Inverse Problems 14:R1–R54. https://doi.org/10.1088/0266-5611/14/4/001
- Barbieri, M. & Lichtenegger, J. 2005. Introduction to SAR for Geology. In K. Fletcher (ed), Spaceborne radar applications in Geology; ESA TM-17: 1–54, Noordwijk: European Space Agency
- Barrett, E.C. & Curtis L. F. (1976). Introduction to Environmental Remote Sensing. Chapman and Hall Ltd.,
- Berardino, P., Costantini, M., Franceschetti, G., Iodice, A., Pietranera, L., & Rizzo, V. (2003). Use of differential SAR interferometry in monitoring and modelling large slope instability at Maratea (Basilicata, Italy). Engineering Geology, 68(1-2), 31-51.
- Berardino, P., Fornaro, G., Lanari, R., & Sansosti, E. (2002). A new algorithm for surface deformation monitoring based on small baseline differential SAR interferograms. IEEE Transactions on geoscience and remote sensing, 40(11), 2375-2383.

- Bonardi, G., Compagnoni, R., Del Moro, A., Macaione, E., Messina, A., & Perrone, V. (2008). Rb–Sr age constraints on the Alpine metamorphic overprint in the Aspromonte Nappe (Calabria–Peloritani Composite Terrane, southern Italy). Bollettino della Società Geologica Italiana, 127, 173-190.
- Bonelli, S., Tourment, R., & Felix, H. (2003). Analysis of earthdam monitoring data. Selected problems of water engineering, Kraków, 133-150.
- Bosshard, P. (2010). The dam industry, the World Commission on Dams and the HSAF process. Water Alternatives, 3(2), 58–70.
- Bowels, D.S., Gilulian, F.L, Desmond, N.D., Hartford, J.P., Hans, F.M., McGraths, S., Poupart, M., Stewart, D. and Zeliniski, P.A. (2007). ICOLD Bulletin On Dam Safety Management. SGM Consulting. https://www.sgmconsulting.com.au/our-people
- Brown, P. H., Tullos, D., Tilt, B., Magee, D., & Wolf, A. T. (2009). Modeling the costs and benefits of dam construction from a multidisciplinary perspective. Journal of Environmental Management, 90(SUPPL. 3). https://doi.org/10.1016/j.jenvman.2008.07.025
- Calcaterra, D., & Parise, M. (2010). Weathering in the crystalline rocks of Calabria, Italy, and relationships to landslides. Geological Society, London, Engineering Geology Special Publications, 23(1), 105-130.
- Campbell JB, Wynne RH (2011) Introduction to Remote Sensing, Fifth Edition. Guilford Press
- Casagli, N., Tofani, V., Ciampalini, A., Raspini, F., Lu, P. and Morelli, S. (2018). XT-tool 2.039-3.1: Satellite Remote Sensing Techniques for Landslides Detection and Mapping. n book: Landslide Dynamics: ISDR-ICL Landslide Interactive Teaching Tools. January.
- Cheng X, Li QQ, Zhou ZW, Luo ZX, Liu M, Liu L. Research on a seepage monitoring model of a high core rockfill dam based on machine learning. Sensors. 2018; **18**: 1- 14.
- Cirrincione, R., Fazio, E., Fiannacca, P., Ortolano, G., Pezzino, A., & Punturo, R. (2015). The Calabria-Peloritani Orogen, a composite terrane in Central Mediterranean; its overall architecture and geodynamic significance for a pre-Alpine scenario around the Tethyan basin. Periodico di Mineralogia, 84(3B), 701-749.
- Confuorto P., Di Martire D., Centolanza G., Iglesias R., Mallorqui J. J., Novellino A.,Plank S., Ramondini ., Thuro K, & Calcaterra, D. (2017). Post-failure evolution analysis of a rainfall-triggered landslide by multi-temporal interferometry SAR approaches integrated with geotechnical analysis. Remote sensing of environment, 188, 51-72.
- Deutsches Talsperren Komitee (2020). E.V (German Committee for Large Dams). Dams Worldwide. Web site visited on 2019-12-20. https://www.talsperrenkomitee.de/de/talsperren-weltweit.html

- Di Martire D., Novellino A., Ramondini M., & Calcaterra D. (2016). A-differential synthetic aperture radar interferometry analysis of a deep seated gravitational slope deformation occurring at Bisaccia (Italy). Science of the Total Environment, 550, 556-573.
- Di Martire, D., Iglesias, R., Monells, D., Centolanza, G., Sica, S., Ramondini, M., ... & Calcaterra, D. (2014). Comparison between differential SAR interferometry and ground measurements data in the displacement monitoring of the earth-dam of Conza della Campania (Italy). Remote sensing of environment, 148, 58-69.
- El Kamali, M., Abuelgasim, A., Papoutsis, I., Loupasakis, C., & Kontoes, C. (2020). A reasoned bibliography on SAR interferometry applications and outlook on big interferometric data processing. Remote Sensing Applications: Society and Environment, 19, 100358.
- Emadali, L., Motagh, M., & Haghshenas Haghighi, M. (2017). Characterizing post-construction settlement of the Masjed-Soleyman embankment dam, Southwest Iran, using TerraSAR-X SpotLight radar imagery. Engineering Structures, 143, 261–273. https://doi.org/10.1016/j.engstruct.2017.04.009
- Emadali, L., Motagh, M., & Haghshenas Haghighi, M. (2017). Characterizing post-construction settlement of the Masjed-Soleyman embankment dam, Southwest Iran, using TerraSAR-X SpotLight radar imagery. Engineering Structures, 143, 261–273. https://doi.org/10.1016/j.engstruct.2017.04.009
- Erol, S., Erol, B., & Ayan, T. (2004). A general review of the deformation monitoring techniques and a case study: Analysing deformations using GPS/levelling. A Paper Presented at XXth ISPRS Congress" Geo-Imagery Bridging Continents, 12–23.
- Fazio, E., Cirrincione, R., & Pezzino, A. (2015). Tectono-metamorphic map of the south-western flank of the Aspromonte Massif (southern Calabria-Italy). Journal of Maps, 11(1), 85-100.
- Faccenna, C., Molin, P., Orecchio, B., Olivetti, V., Bellier, O., Funiciello, F., ... & Billi, A. (2011). Topography of the Calabria subduction zone (southern Italy): Clues for the origin of Mt. Etna. Tectonics, 30(1).
- Feigl, K. L., Gasperi, J., Sigmundsson, F., & Rigo, A. (2000). Crustal deformation near Hengill volcano, Iceland 1993–1998: Coupling between magmatic activity and faulting inferred from elastic modeling of satellite radar interferograms. Journal of Geophysical Research: Solid Earth, 105(B11), 25655-25670.
- Ferretti, A., Prati, C., & Rocca, F. (2001). Permanent scatterers in SAR interferometry. IEEE Transactions on geoscience and remote sensing, 39(1), 8-20.
- Franceschetti, G., Iodice, A., Perna, S., & Riccio, D. (2006). Efficient simulation of airborne SAR raw data of extended scenes. IEEE Transactions on Geoscience and Remote Sensing, 44(10), 2851-2860.

- Gabriel, A. K., Goldstein, R. M., & Zebker, H. A. (1989). Mapping small elevation changes over large areas: Differential radar interferometry. Journal of Geophysical Research: Solid Earth, 94(B7), 9183-9191.
- Gökalp, E., & Taşçı, L. (2009). Deformation Monitoring by GPS at Embankment Dams and Deformation Analysis. Survey Review, 41(311), 86–102. https://doi.org/10.1179/003962608X390021

-Heymes, T., Bouillin, J. P., Pecher, A., Monié, P., & Compagnoni, R. (2008). Middle Oligocene extension in the Mediterranean Calabro-Peloritan belt (southern Italy): Insights from the Aspromonte nappes pile. Tectonics, 27(2).

-Ho Tong Minh, D., Hanssen, R., & Rocca, F. (2020). Radar interferometry: 20 years of development in time series techniques and future perspectives. Remote Sensing, 12(9), 1364.

http://www.infoterra.de/terrasar-x.html

- https://annuario.isprambiente.it/
- https://dgdighe.mit.gov.it/categoria/articolo/_cartografie_e_dati/_cartografie/cartografia_dighe
- https://dgdighe.mit.gov.it/categoria/articolo/_storia_delle_dighe/prime_dighe
- ICOLD (2020). World Register of Dams-General Synthesis.
- https://www.icoldcigb.org/GB/world_register/world_register_of_dams.asp
- ICOLD. (1989). Monitoring of dams and their foundations - state of the art. Paris.

- Infante, D., Di Martire, D., Confuorto, P., Tessitore, S., Ramondini, M., & Calcaterra, D. (2018). Differential SAR interferometry technique for control of linear infrastructures affected by ground instability phenomena. Int. Arch. Photogramm. Remote Sens. Spat. Inf. Sci, 251-258
- Ioppolo, S., Pezzino, A., & Puglisi, G. (1982). Caratteri petrografico-strutturali et petrochomici delle metamorfiti di grado medio-basso di Madonna dei Polsi (Aspromonte, Calabria Meridionale). Mineralogica et petrographica acta, 26, 143-158.
- Johansson, S., & Watley, D. (2007). Dam safety experiences from distributed strain measurements in five embankment dams. Stockholm. Retrieved from http://www.hydroresearch.se/en/downloads/07_52_rappport_DTSS4.pdf
- K. Choi, J. Yi, C. Park and S. Yoon, "Deep Learning for Anomaly Detection in Time-Series Data: Review, Analysis, and Guidelines," in IEEE Access, vol. 9, pp. 120043-120065, 2021, doi: 10.1109/ACCESS.2021.3107975.
- L. Amodio-Morelli, G. Bonardi, V. Colonna, D. Dietrich, G. Giunta, F. Ippolito, V. Liguori, S. Lorenzoni, A. Paglionico, V. Perrone, G. Piccarreta, M. Russo, P. Scandone, E. Zanettin-Lorenzoni, A. Zuppetta- L'arco Calabro-Peloritano nell'orogene appenninico Maghrebide (The Calabrian-Peloritan Arc in the Apennine-Maghrebide orogen) Memorie della Società Geologica Italiana, 17 (1976), pp. 1-60

- L. Tortorici Lineamenti geologico-strutturali dell'Arco Calabro Peloritano (Geologic-structural lineaments of the Calabrian-Peloritan Arc) Società Italiana di Mineralogia e Petrografia, 38 (1982), pp. 927-940
- Li Z, Liu Z, Wang Z. GPS in dam deformation monitoring (in Chinese). J Wuhan Univ Hydraulic Electr Eng, 1996, 29: 26–29
- Li, B., Yang, J., & Hu, D. (2020). Dam monitoring data analysis methods: A literature review. Structural Control and Health Monitoring, 27(3), e2501.
- Massonnet, D., & Rabaute, T. (1993). Radar interferometry: limits and potential. IEEE Transactions on Geoscience and Remote Sensing, 31(2), 455-464.
- Mays, L. W. (2010). Water resources engineering. John Wiley & Sons.International Rivers Organization (2020). Damming Statistics
- McNairn, H., & Shang, J. (2016). A review of multitemporal synthetic aperture radar (SAR) for crop monitoring. Multitemporal Remote Sensing: Methods and Applications, 317-340.
- Michalis, P., Pytharouli, S. I., & Raftopoulos, S. (2016). Long-term Deformation Patterns of Earth-fill Dams based on Geodetic Monitoring Data: the Pournari I Dam Case Study. In Proc. of 3rd Joint International Symposium on Deformation Monitoring (pp. 1–5).
- Michalis, P., Sentenac, P., & Macbrayne, D. (2016, March). Geophysical assessment of dam infrastructure: The mugdock reservoir dam case study. In Proceedings of the 3rd Joint International Symposium on Deformation Monitoring (JISDM), Vienna, Austria (Vol. 30, pp. 1-6).
- Milillo, P., Perissin, D., Salzer, J. T., Lundgren, P., Lacava, G., Milillo, G., & Serio, C. (2016). Monitoring dam structural health from space: Insights from novel InSAR techniques and multi-parametric modeling applied to the Pertusillo dam Basilicata, Italy. International Journal of Applied Earth Observation and Geoinformation, 52, 221–229. https://doi.org/10.1016/j.jag.2016.06.013
- Milillo, P., Perissin, D., Salzer, J. T., Lundgren, P., Lacava, G., Milillo, G., & Serio, C. (2016). Monitoring dam structural health from space: Insights from novel InSAR techniques and multi-parametric modeling applied to the Pertusillo dam Basilicata, Italy. International Journal of Applied Earth Observation and Geoinformation, 52, 221–229. https://doi.org/10.1016/j.jag.2016.06.013
- Mizuno, M., & Hirose, T. (2009). Instrumentation and monitoring of dams and reservoirs. Water Storage, Transport, and Distribution, 253.
- Mora, J. R., Bono, M. R., Manjunath, N., Weninger, W., Cavanagh, L. L., Rosemblatt, M., & Von Andrian, U. H. (2003). Selective imprinting of gut-homing T cells by Peyer's patch dendritic cells. Nature, 424(6944), 88-93.
- Musa, Z. N., Popescu, I., & Mynett, A. (2015). A review of applications of satellite SAR, optical, altimetry and DEM data for surface water modelling,

mapping and parameter estimation. Hydrology and Earth System Sciences, 19(9), 3755-3769.

- Parise, M., Sorriso-Valvo, M., & Tansi, C. (1997). Mass movements related to tectonics in the Aspromonte massif (southern Italy). Engineering Geology, 47(1-2), 89-106.
- Parise, M., Sorriso-Valvo, M., & Tansi, C. (1997). Mass movements related to tectonics in the Aspromonte massif (southern Italy). Engineering Geology, 47(1-2), 89-106.
- Pereira, S., Magalhães, F., Gomes, J. P., Cunha, Á., & Lemos, J. V. (2018). Dynamic monitoring of a concrete arch dam during the first filling of the reservoir. Engineering Structures, 174, 548-560
- Perissin, D. (2016). Interferometric SAR Multitemporal Processing: Techniques and Applications. In Multitemporal Remote Sensing (pp. 145–176). Springer
- Pezzino, A., Angì, G., Fazio, E., Fiannacca, P., Lo Giudice, A., Ortolano, G., ... & De Vuono, E. (2008). Alpine metamorphism in the Aspromonte massif: Implications for a new framework for the southern sector of the Calabria-Peloritani orogen, Italy. International Geology Review, 50(5), 423-441.
- Prati, C., Rocca, F., Guarnieri, A. M., & Damonti, E. (1990). Seismic migration for SAR focusing: Interferometrical applications. IEEE Transactions on Geoscience and Remote Sensing, 28(4), 627-640.
- Roque, D., Perissin, D., Falcão, A. P., Fonseca, A. M., & Maria, J. (2015). Dams regional safety warning using time-series insar techniques. In Second Internatinal Dam World Conference (pp. 21–24). Lisbon: LNEC.
- Roque, D., Perissin, D., Falcao, A.P., Fonseca, A.M., Henriques, M.J., Franco, J. (2015). Dams regional safety warning using time-series InSAR techniques. In 2nd International Dam World Conference, Portugal, Lisbon, 21-24 April.
- Ruiz-Armenteros, A. M., Marchamalo-Sacrsitán, M., Bakoň, M., Lamas-Fernández, F., Delgado, J. M., Sánchez-Ballesteros, V., ... & Sousa, J. J. (2021). Monitoring of an embankment dam in southern Spain based on Sentinel-1 Time-series InSAR. Procedia Computer Science, 181, 353-359.
- Salazar F, Toledo MA, Oñate E, Morán R. An empirical comparison of machine learning techniques for dam behaviour modelling. Struct Saf. 2015; **56**: 9- 17
- Samsonov, S., & d'Oreye, N. (2012). Multidimensional time-series analysis of ground deformation from multiple InSAR data sets applied to Virunga Volcanic Province. Geophysical Journal International, 191(3), 1095-1108.
- Scaioni, M., Marsella, M., Crosetto, M., Tornatore, V., Wang, J. (2018).Geodetic and Remote-Sensing Sensors for Dam Deformation Monitoring. Sensors, 18, 3682.

- Schmullius, C. C., & Evans, D. L. (1997). Review article Synthetic aperture radar (SAR) frequency and polarization requirements for applications in ecology, geology, hydrology, and oceanography: A tabular status quo after SIR-C/X-SAR. International Journal of Remote Sensing, 18(13), 2713-2722.
- SCHNITTER, Niklaus - A History of Dams The Useful Pyramids. Ed. Balkema - Rotterdam, 1994.
- Sjödahl, P. (2006). Resistivity investigation and monitoring for detection of internal erosion and anomalous seepage in embankment dams. Lund University.
- Stewart, M., & Tsakiri, M. (1993). The Application of GPS To Dam Surface Monitoring. Journal of Geospatial Engineering, 3(1), 45–57
- Sousa, J.J., Lazecky, M., Hlavacova, I., Bakon, M., Patricio, G, Perissin, D. (2015). Satellite SAR interferometry for monitoring dam deformations in Portugal. Second International Dam World Conference, Portugal, 21–24 April.
- Stewart, M., & Tsakiri, M. (1993). The Application of GPS To Dam Surface Monitoring. Journal of Geospatial Engineering, 3(1), 45–57.
- Szostak-Chrzanowski, A., & Massiéra, M. (2004). Modelling of deformations during construction of a large earth dam in the la grande complex, Canada. Technical Sciences, 7.
- Szostak-Chrzanowski, A., & Massiéra, M. (2006). Relation between monitoring and design aspects of large earth dams. In Proceedings of the 3rd IAG Symposium on Geodesy for Geotechnical and Structural Engineering and 12-th FIG Symposium on Deformation Measurements, ed. H. Kahmen and A. Chrzanowski, Baden, Austria, May (pp. 21–24).
- Tata and Howard blog (2016). A History of Dams from ancient times today. Unsurpassed solutions in Water Environment, T&H, May 17. https://tataandhoward.com/2016/05/a-history-of-dams-from-ancient-times-totoday
- Tempfli K, Kerle N, Huurneman GC, Janssen LL (2009) Principles of remote sensing. In The international institute for geo-information science and Earth observation, Netherlands.
- (Tele – Rilevamento Europa, 2008).
- Tomas, R., Cano, M., Garcia-Barba, J., Vicente, F., Herrera, G., Lopez-Sanchez, J. M., Mallorqui, J. J. (2013). Monitoring an earthfill dam using differential SAR interferometry: La Pedrera dam, Alicante, Spain. Engineering Geology, 157, 21–32
- Tortorici, L., Monaco, C., Tansi, C., & Cocina, O. (1995). Recent and active tectonics in the Calabrian arc (Southern Italy). Tectonophysics, 243(1-2), 37-55.
- U.S.Bureau Of Reclamation. (1987). Design of small dams (3rd ed.). Washington D.C.: U.S. Government Printing Office

- Ullo, S. L., Addabbo, P., Di Martire, D., Sica, S., Fiscante, N., Cicala, L., & Angelino, C. V. (2019). Application of DInSAR technique to high coherence Sentinel-1 images for dam monitoring and result validation through in situ measurements. IEEE Journal of Selected Topics in Applied Earth Observations and Remote Sensing, 12(3), 875-890.
- Wang, J., Stewart, M. P., & Tsakiri, M. (1998). Stochastic modeling for static GPS baseline data processing. Journal of Surveying Engineering, 124(4), 171-181.
- Wang, T., Perissin, D., Rocca, F., & Liao, M. S. (2011). Three Gorges Dam stability monitoring with time-series InSAR image analysis. Science China Earth Sciences, 54(5), 720–732. https://doi.org/10.1007/s11430-010-4101-1
- Wang, T., Perissin, D., Rocca, F., & Liao, M. S. (2011). Three Gorges Dam stability monitoring with time-series InSAR image analysis. Science China Earth Sciences, 54, 720-732.
- Wu ZR. Safety Monitoring Theory & Its Application of Hydraulic Structures. 1st ed. Beijing: Higher Education Press; 2003.
- Yan J, Li S. Optimization design of deformation monitoring for TGP's dam (in Chinese). Yangtze River, 2002, 33: 36–38
- Yang J, Wu Z. Present conditions and development of dam safety monitoring and control researches home and abroad (in Chinese). J Xi'an Univ Technol, 2002, 18: 26–30
- Yang, H., Haynes, M., Winzenread, S., & Okada, K. (1999). The History of Dams. watershed.ucdavis.edu.
- Zakhvatkina, N., Smirnov, V., & Bychkova, I. (2019). Satellite SAR data-based sea ice classification: An overview. Geosciences, 9(4), 152.
- Zebker, H. A., & Goldstein, R. M. (1986). Topographic mapping from interferometric synthetic aperture radar observations. Journal of Geophysical Research: Solid Earth, 91(B5), 4993-4999.

Annex 1

Inclinometer graphs

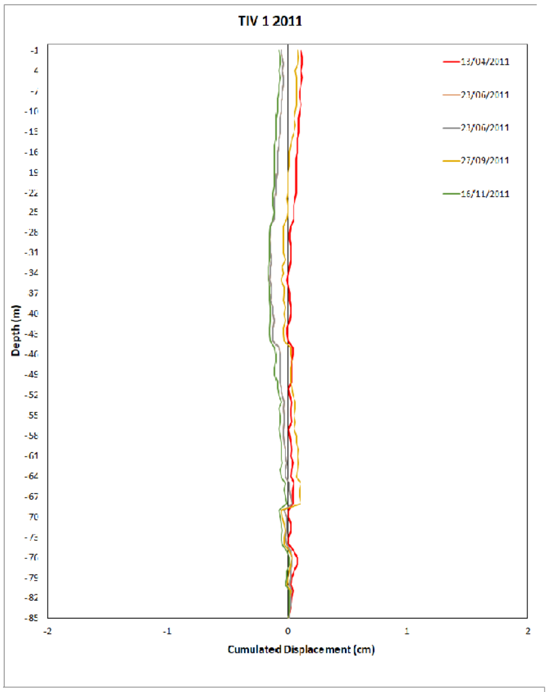
TIV 1 2011
13/04/2011
21/06/2011
21/06/2011
27/09/2011
16/11/2011
Depth (m)
Cumulated Displacement (cm)

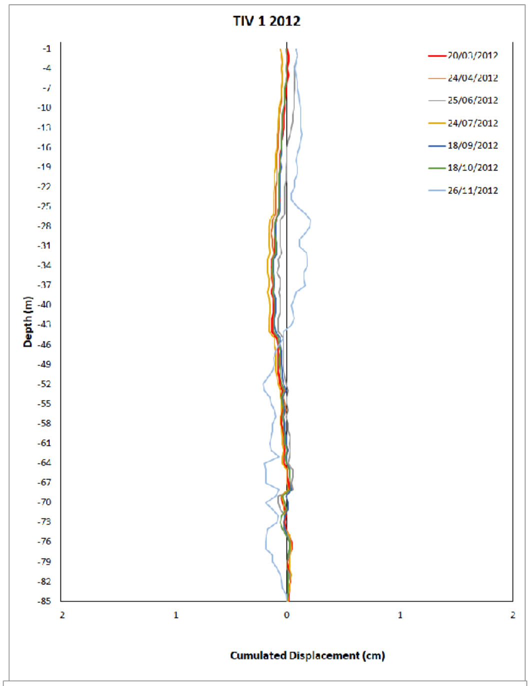
TIV 1 2012
20/03/2012
24/04/2012
25/06/2012
24/07/2012
18/09/2012
18/10/2012
26/11/2012
Depth (m)
Cumulated Displacement (cm)

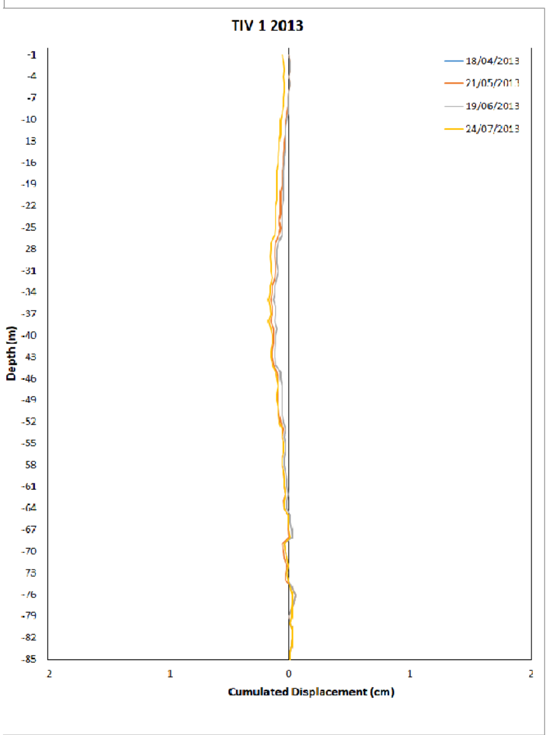
TIV 1 2013
18/04/2013
21/05/2013
19/06/2013
24/07/2013
Depth (m)
Cumulated Displacement (cm)

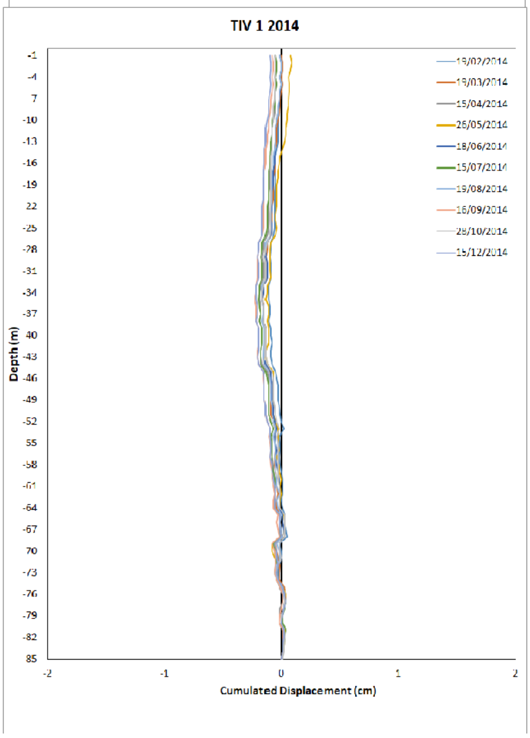
TIV 1 2014
19/02/2014
19/03/2014
15/04/2014
26/05/2014
18/06/2014
15/07/2014
19/08/2014
16/09/2014
28/10/2014
15/12/2014
Depth (m)
Cumulated Displacement (cm)

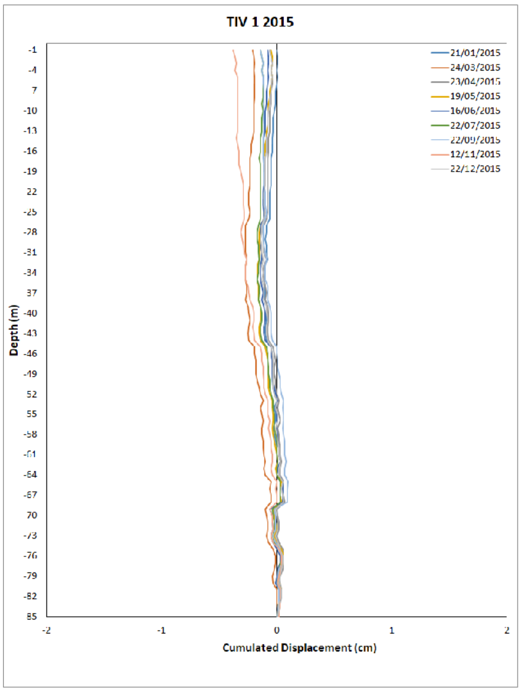
TIV 1 2015
21/01/2015
24/03/2015
23/04/2015
19/05/2015
16/06/2015
22/07/2015
22/09/2015
12/11/2015
22/12/2015
Depth (m)
Cumulated Displacement (cm)

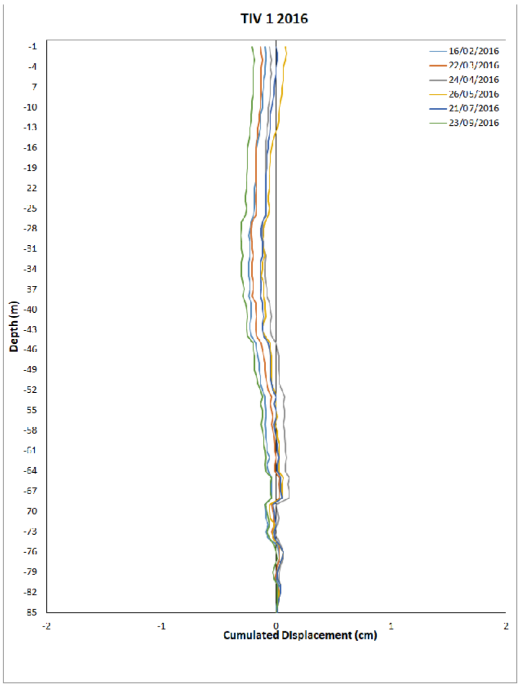
TIV 1 2016
16/02/2016
22/03/2016
24/04/2016
26/05/2016
21/07/2016
23/09/2016
Depth (m)
Cumulated Displacement (cm)

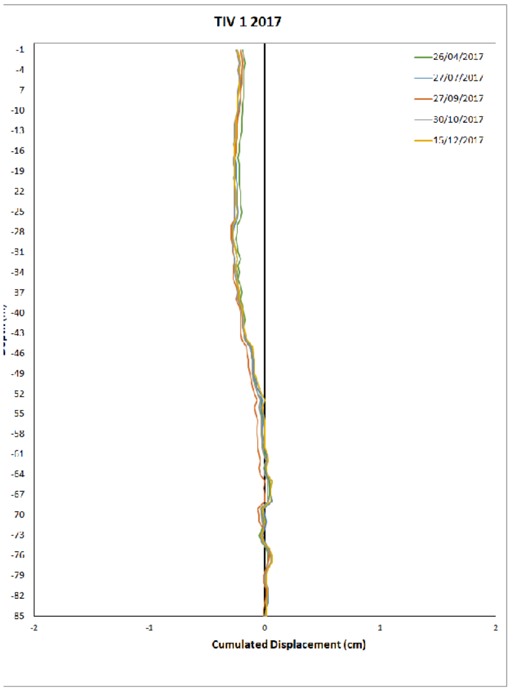
TIV 1 2017
26/04/2017
27/07/2017
27/09/2017
30/10/2017
15/12/2017
Cumulated Displacement (cm)

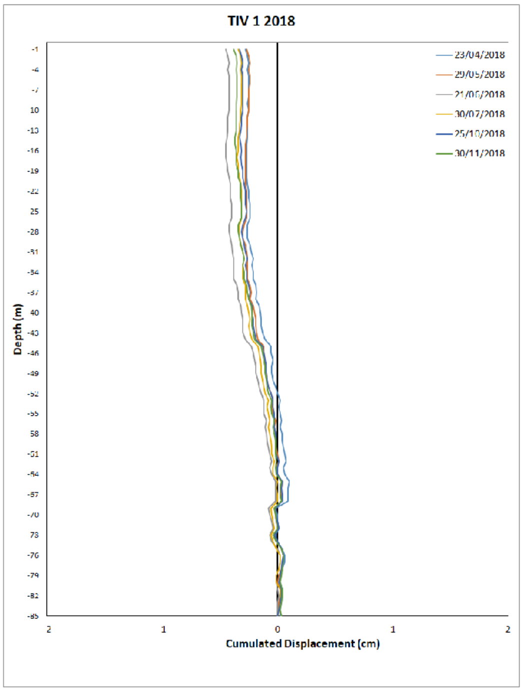
TIV 1 2018
23/04/2018
29/05/2018
21/06/2018
30/07/2018
25/10/2018
30/11/2018
Depth (m)
Cumulated Displacement (cm)

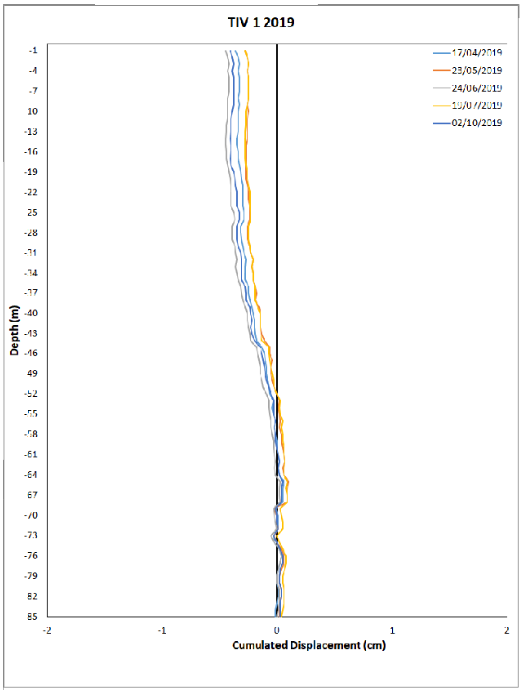
TIV 1 2019
17/04/2019
23/05/2019
24/06/2019
19/07/2019
02/10/2019
Depth (m)
Cumulated Displacement (cm)

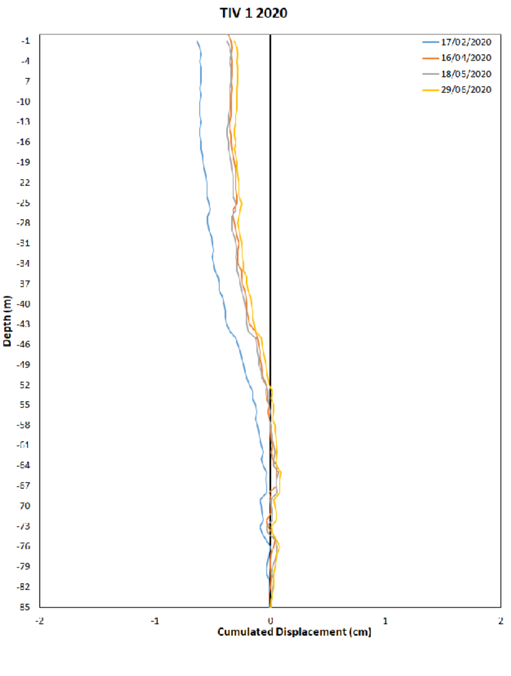
TIV 1 2020
17/02/2020
16/04/2020
18/05/2020
29/06/2020
Depth (m)
Cumulated Displacement (cm)

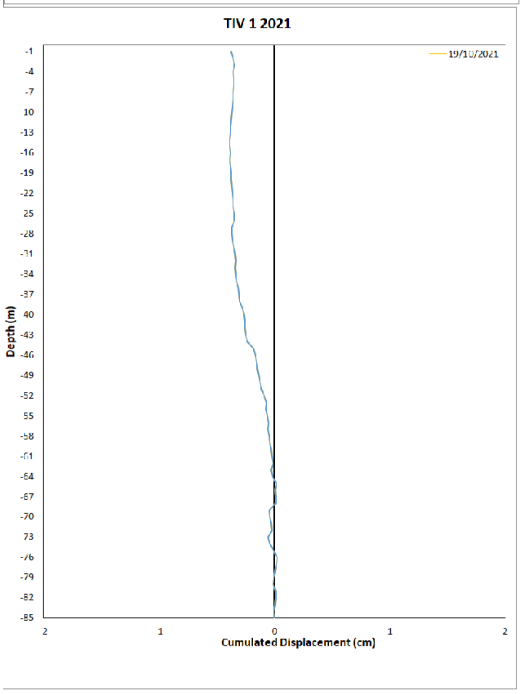
TIV 1 2021
19/10/2021
Depth (m)
Cumulated Displacement (cm)

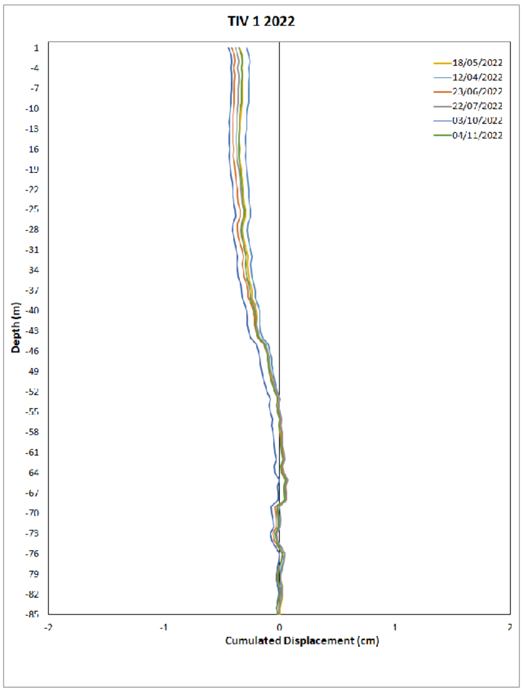
TIV 1 2022
18/05/2022
12/04/2022
23/06/2022
22/07/2022
03/10/2022
04/11/2022
Depth (m)
Cumulated Displacement (cm)

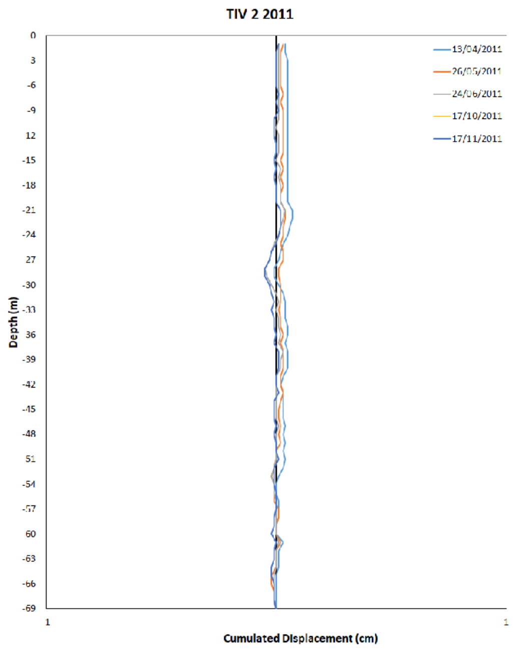
TIV 2 2011
13/04/2011
26/05/2011
24/06/2011
17/10/2011
17/11/2011
Depth (m)
Cumulated Displacement (cm)

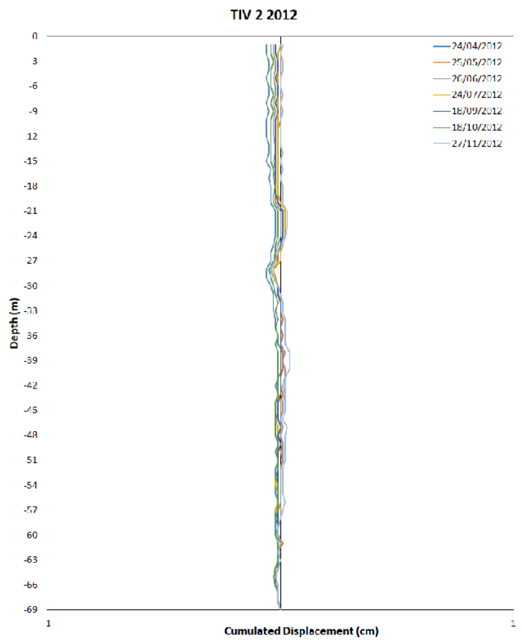
TIV 2 2012
24/04/2012
25/05/2012
20/06/2012
24/07/2012
18/09/2012
18/10/2012
27/11/2012
Depth (m)
Cumulated Displacement (cm)

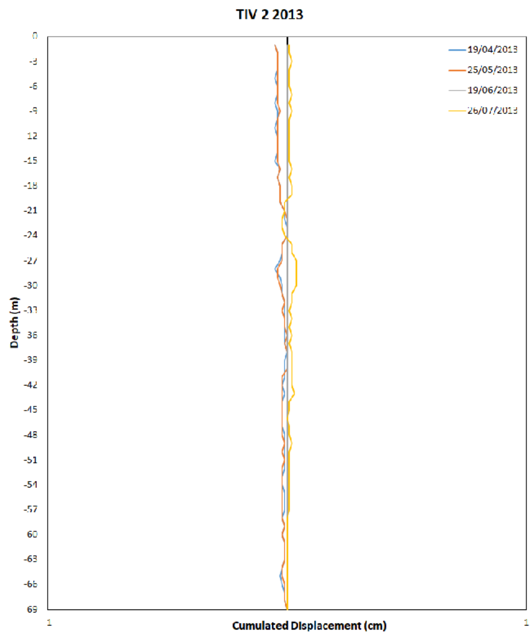
TIV 2 2013
19/04/2013
25/05/2013
19/06/2013
26/07/2013
Depth (m)
Cumulated Displacement (cm)

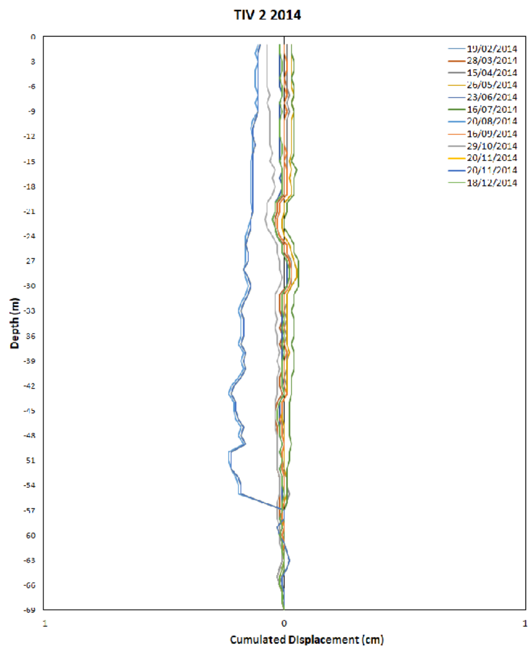
TIV 2 2014
19/02/2014
28/03/2014
15/04/2014
26/05/2014
23/06/2014
16/07/2014
20/08/2014
16/09/2014
29/10/2014
20/11/2014
20/11/2014
18/12/2014
Depth (m)
Cumulated Displacement (cm)

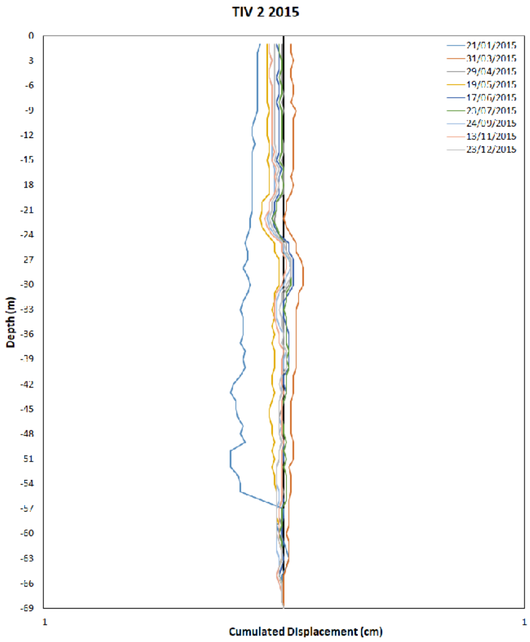
TIV 2 2015
Depth (m)
Cumulated Displacement (cm)
21/01/2015
31/03/2015
29/04/2015
19/05/2015
17/06/2015
23/07/2015
24/09/2015
13/11/2015
23/12/2015

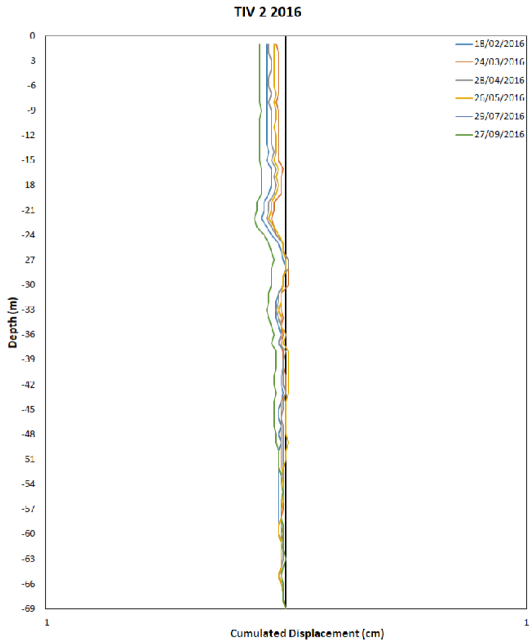
TIV 2 2016
Depth (m)
Cumulated Displacement (cm)
18/02/2016
24/03/2016
28/04/2016
26/05/2016
29/07/2016
27/09/2016

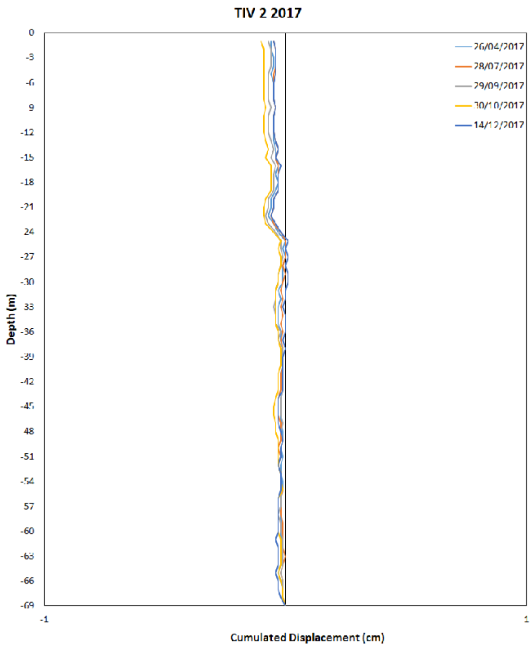
TIV 2 2017
Depth (m)
Cumulated Displacement (cm)
26/04/2017
28/07/2017
29/09/2017
30/10/2017
14/12/2017

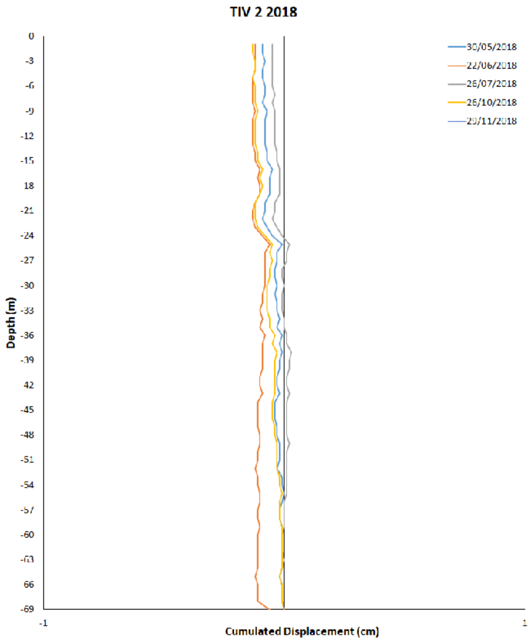
TIV 2 2018
Depth (m)
Cumulated Displacement (cm)
30/05/2018
22/06/2018
26/07/2018
26/10/2018
29/11/2018

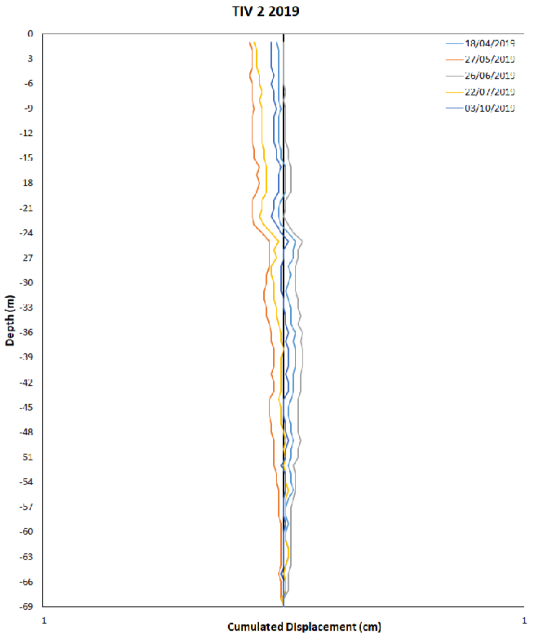
TIV 2 2019
18/04/2019
27/05/2019
26/06/2019
22/07/2019
03/10/2019
Depth (m)
Cumulated Displacement (cm)

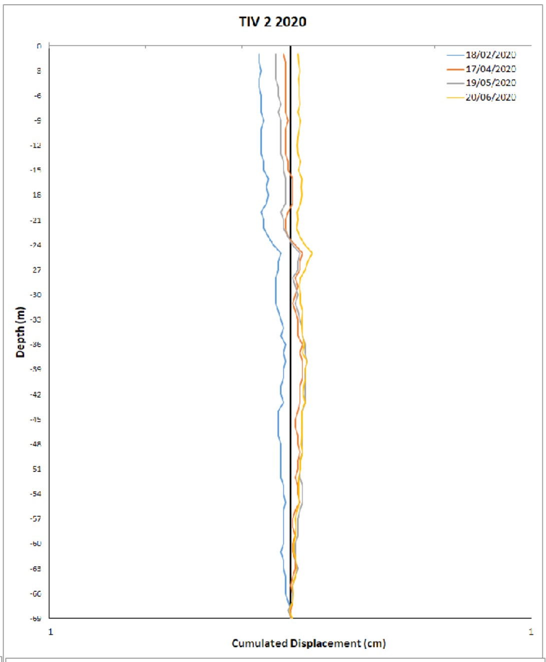
TIV 2 2020
18/02/2020
17/04/2020
19/05/2020
20/06/2020
Depth (m)
Cumulated Displacement (cm)

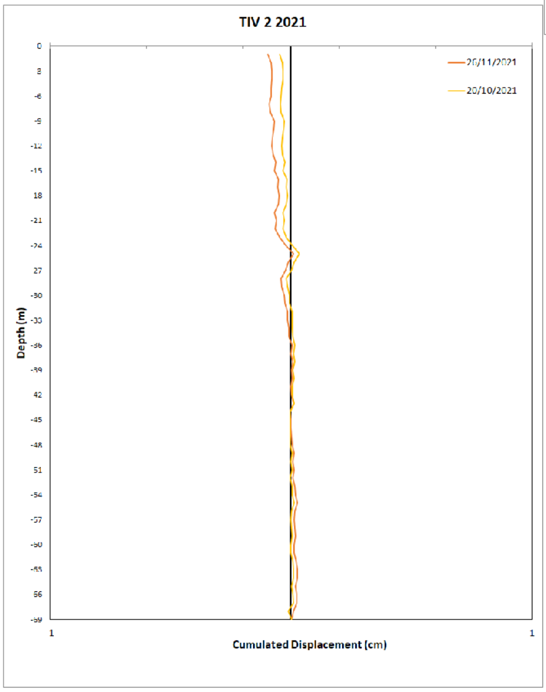
TIV 2 2021
26/11/2021
20/10/2021
Depth (m)
Cumulated Displacement (cm)

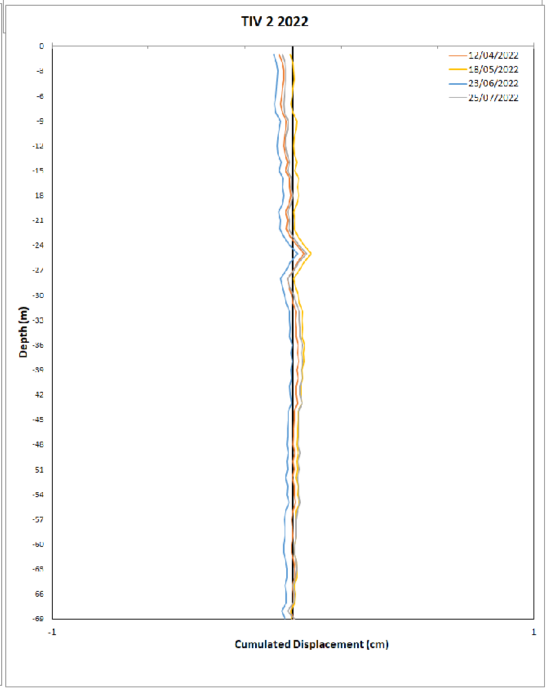
TIV 2 2022
12/04/2022
18/05/2022
23/06/2022
25/07/2022
Depth (m)
Cumulated Displacement (cm)

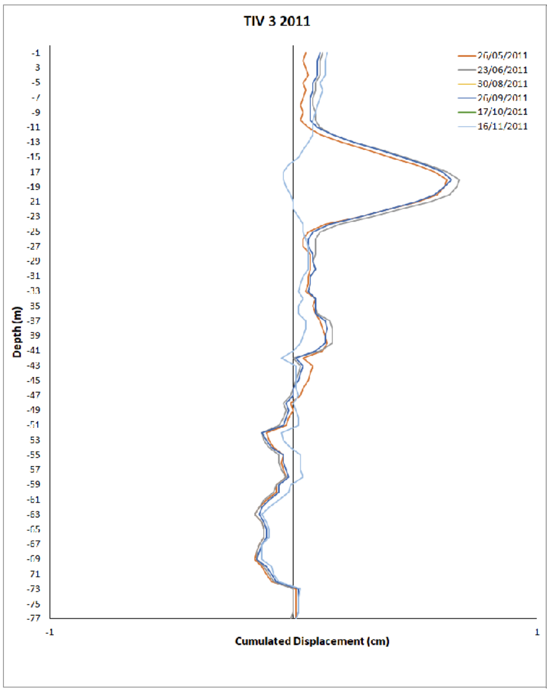
TIV 3 2011
26/05/2011
23/06/2011
30/08/2011
26/09/2011
17/10/2011
16/11/2011
Depth (m)
Cumulated Displacement (cm)
-1
1

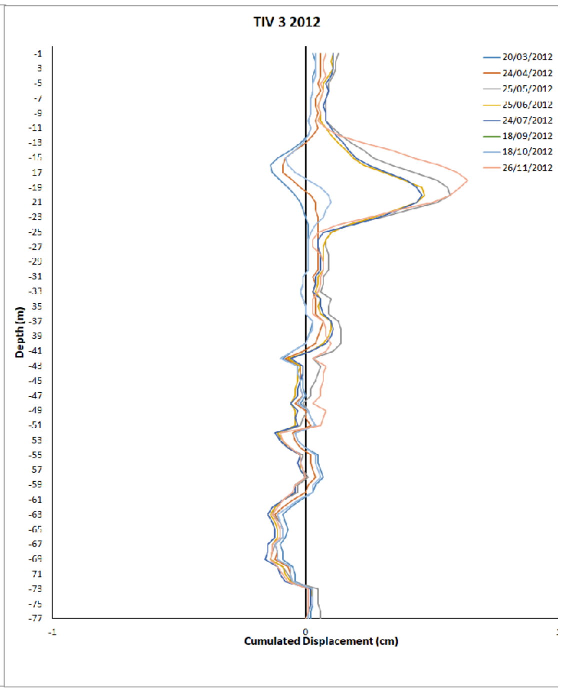
TIV 3 2012
20/03/2012
24/04/2012
25/05/2012
25/06/2012
24/07/2012
18/09/2012
18/10/2012
26/11/2012
Depth (m)
Cumulated Displacement (cm)
-1
0

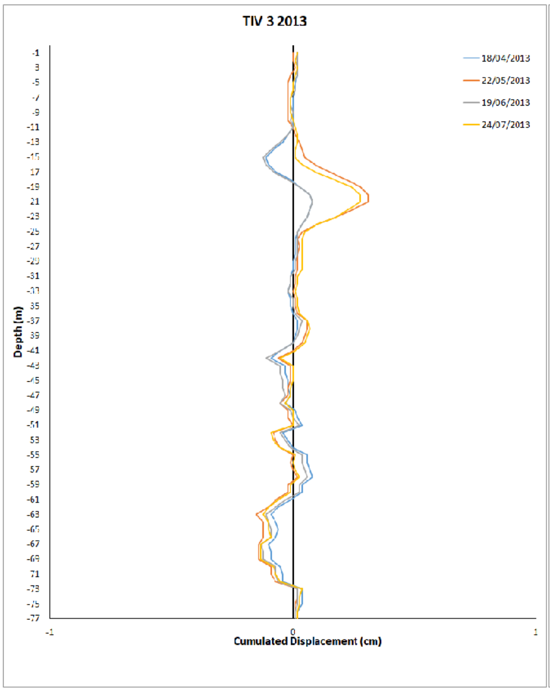
TIV 3 2013
18/04/2013
22/05/2013
19/06/2013
24/07/2013
Depth (m)
Cumulated Displacement (cm)
-1
0
1

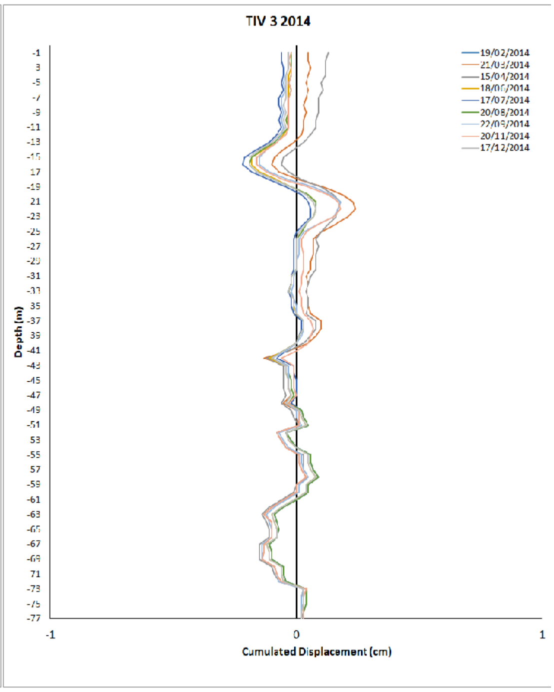
TIV 3 2014
19/02/2014
21/03/2014
15/04/2014
18/06/2014
17/07/2014
20/08/2014
22/09/2014
20/11/2014
17/12/2014
Depth (m)
Cumulated Displacement (cm)
-1
0
1

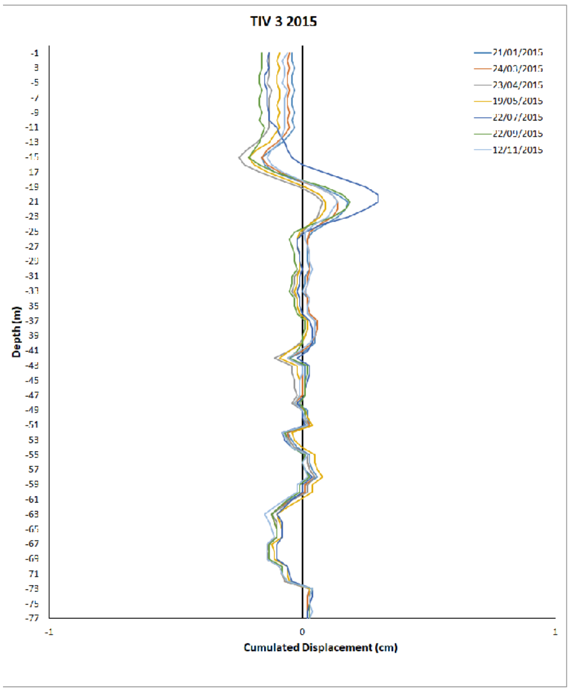
TIV 3 2015
21/01/2015
24/03/2015
23/04/2015
19/05/2015
22/07/2015
22/09/2015
12/11/2015
Depth (m)
Cumulated Displacement (cm)

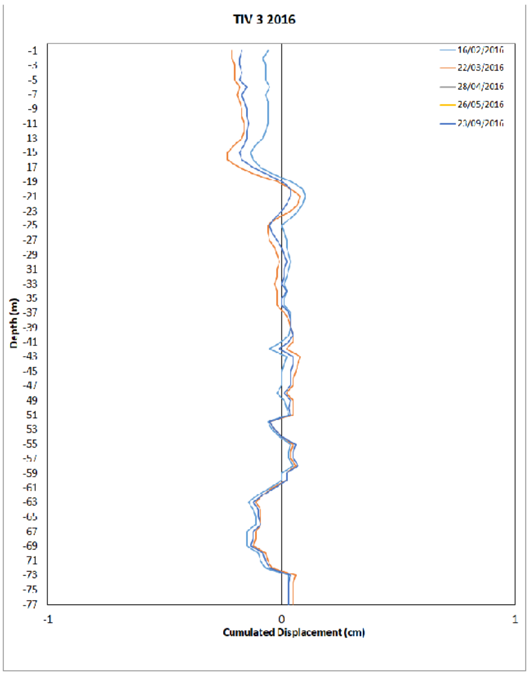
TIV 3 2016
16/02/2016
22/03/2016
28/04/2016
26/05/2016
23/09/2016
Depth (m)
Cumulated Displacement (cm)

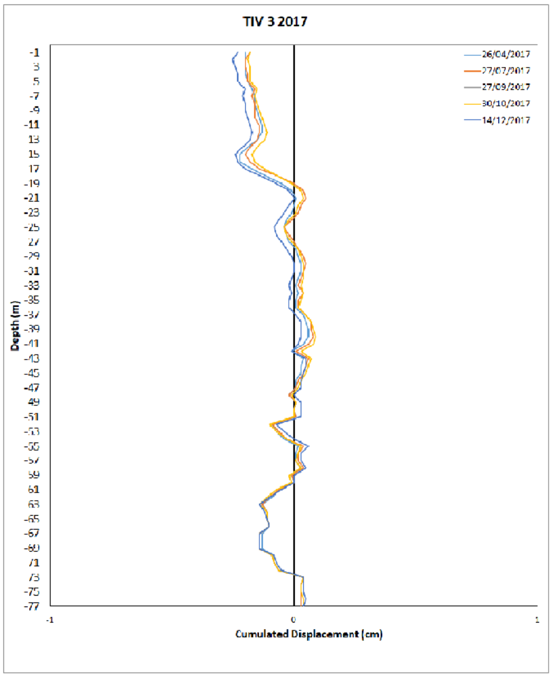
TIV 3 2017
26/04/2017
27/07/2017
27/09/2017
30/10/2017
14/12/2017
Depth (m)
Cumulated Displacement (cm)

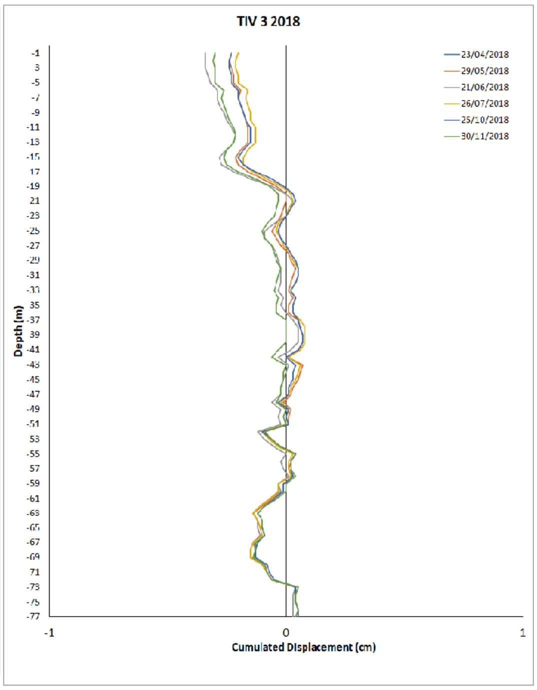
TIV 3 2018
23/04/2018
29/05/2018
21/06/2018
26/07/2018
25/10/2018
30/11/2018
Depth (m)
Cumulated Displacement (cm)

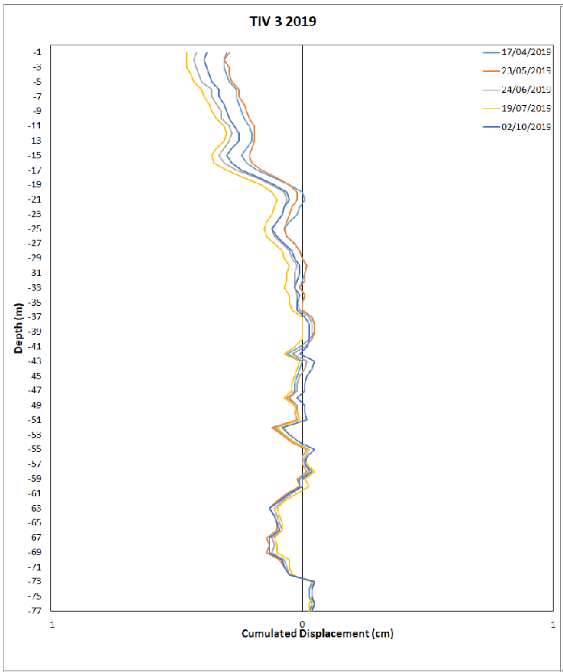
TIV 3 2019
17/04/2019
23/05/2019
24/06/2019
19/07/2019
02/10/2019
Depth (m)
Cumulated Displacement (cm)

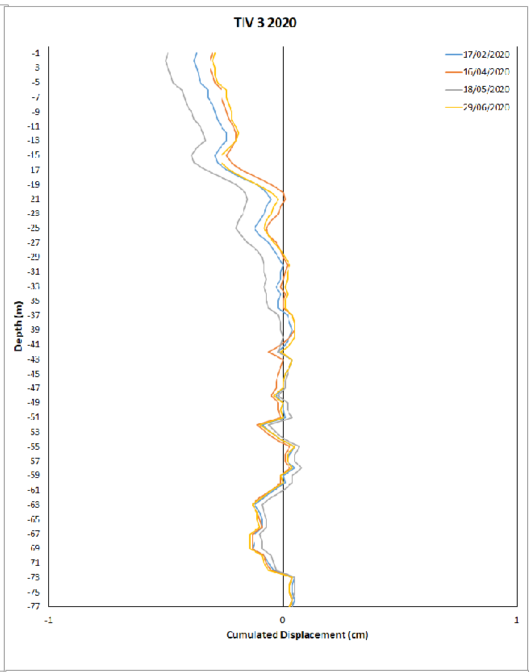
TIV 3 2020
17/02/2020
18/05/2020
Depth (m)
Cumulated Displacement (cm)

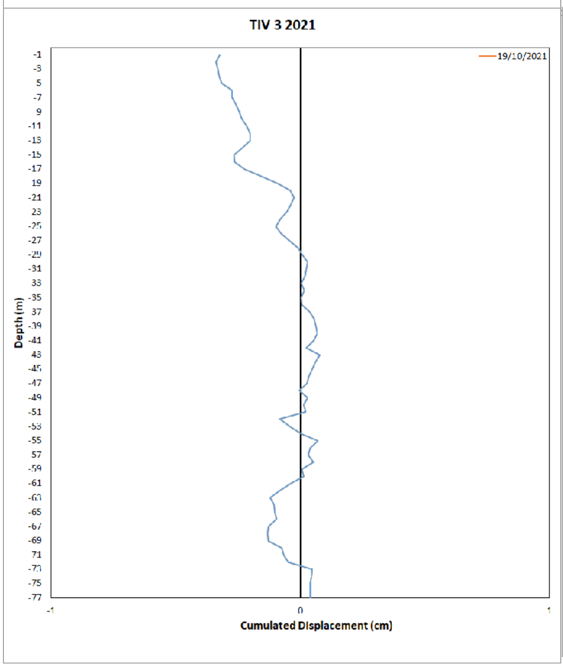
TIV 3 2021
19/10/2021
Depth (m)
Cumulated Displacement (cm)

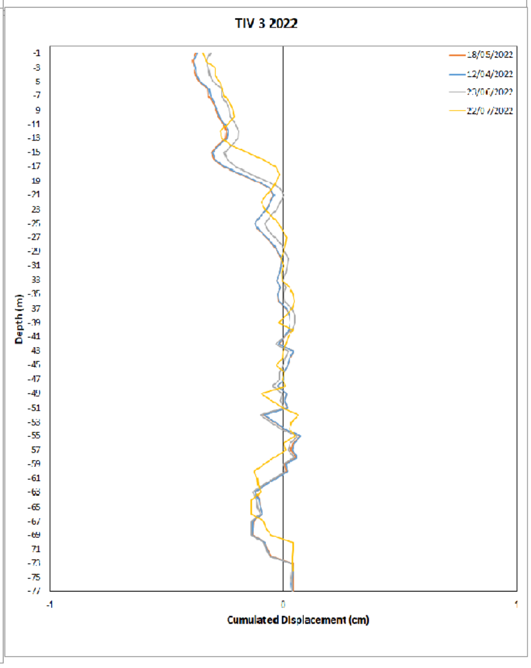
TIV 3 2022
18/05/2022
12/04/2022
Depth (m)
Cumulated Displacement (cm)

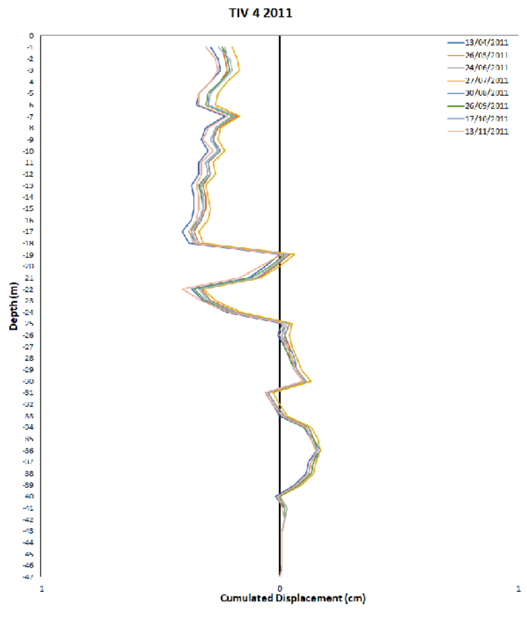
TIV 4 2011
13/04/2011
26/05/2011
24/06/2011
27/07/2011
30/08/2011
26/09/2011
17/10/2011
13/11/2011
Depth (m)
Cumulated Displacement (cm)

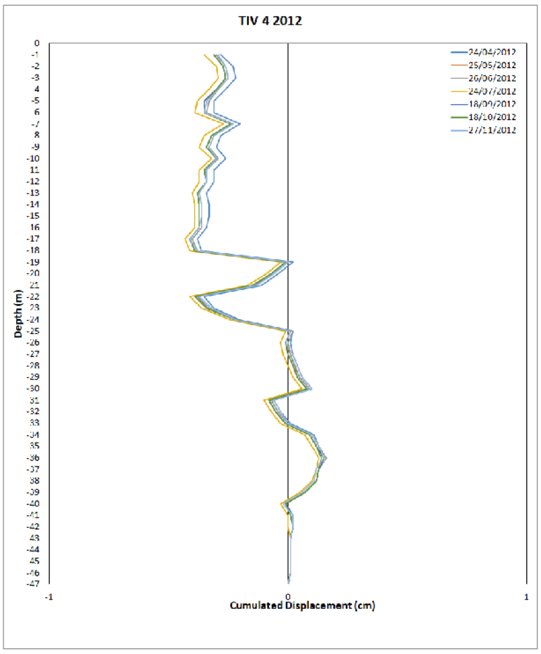
TIV 4 2012
24/04/2012
25/05/2012
26/06/2012
24/07/2012
18/09/2012
18/10/2012
27/11/2012
Depth (m)
Cumulated Displacement (cm)

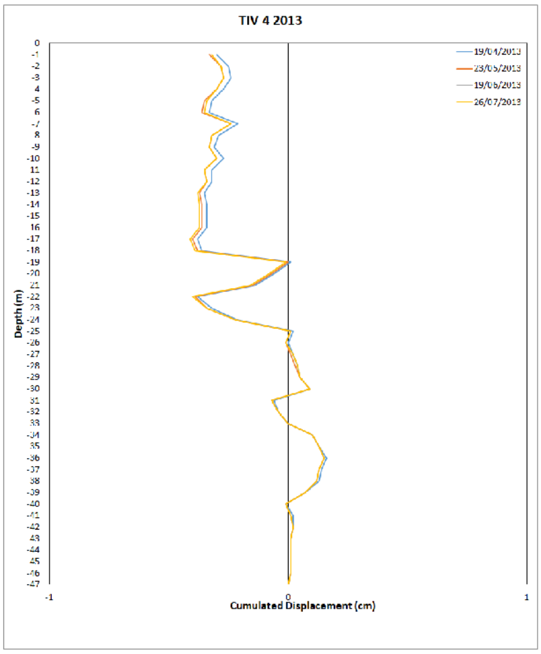
TIV 4 2013
19/04/2013
23/05/2013
19/06/2013
26/07/2013
Depth (m)
Cumulated Displacement (cm)

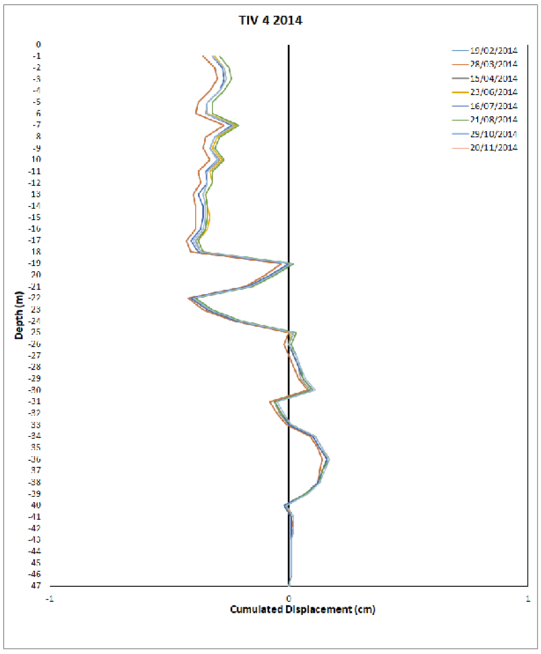
TIV 4 2014
19/02/2014
28/03/2014
15/04/2014
23/06/2014
16/07/2014
21/08/2014
29/10/2014
20/11/2014
Depth (m)
Cumulated Displacement (cm)

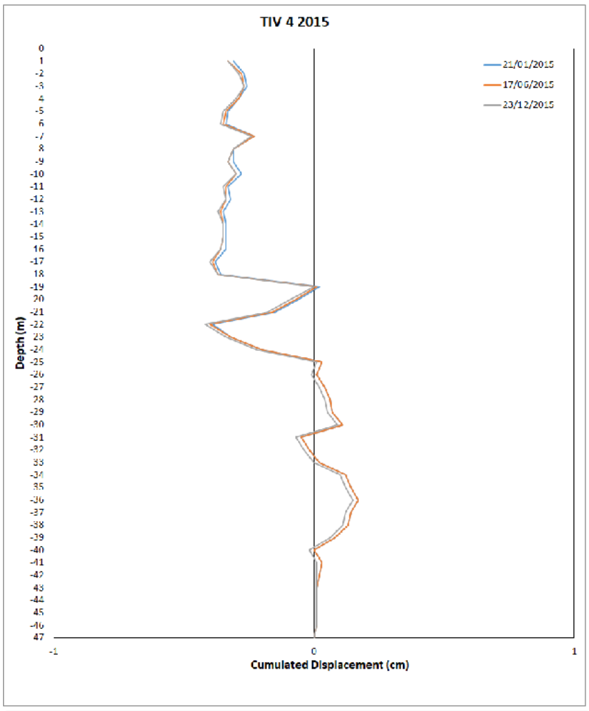
TIV 4 2015
21/01/2015
17/06/2015
23/12/2015
Depth (m)
-1
0
1
Cumulated Displacement (cm)

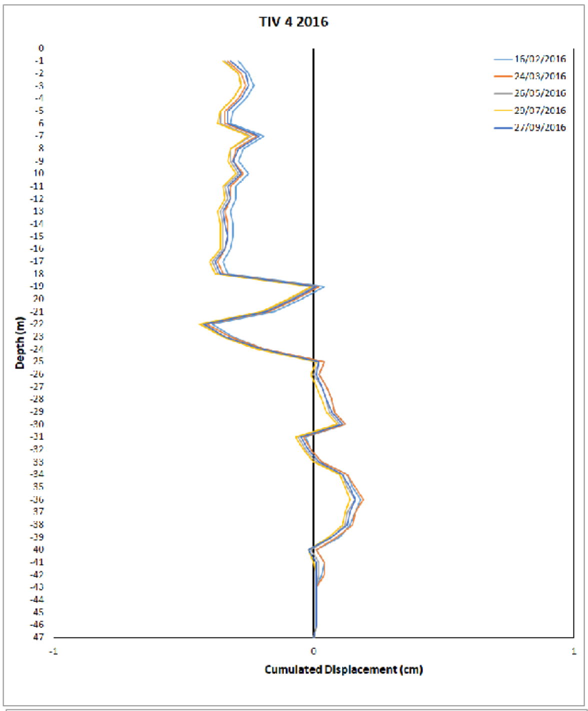
TIV 4 2016
16/02/2016
24/03/2016
26/05/2016
29/07/2016
27/09/2016
Depth (m)
-1
0
1
Cumulated Displacement (cm)

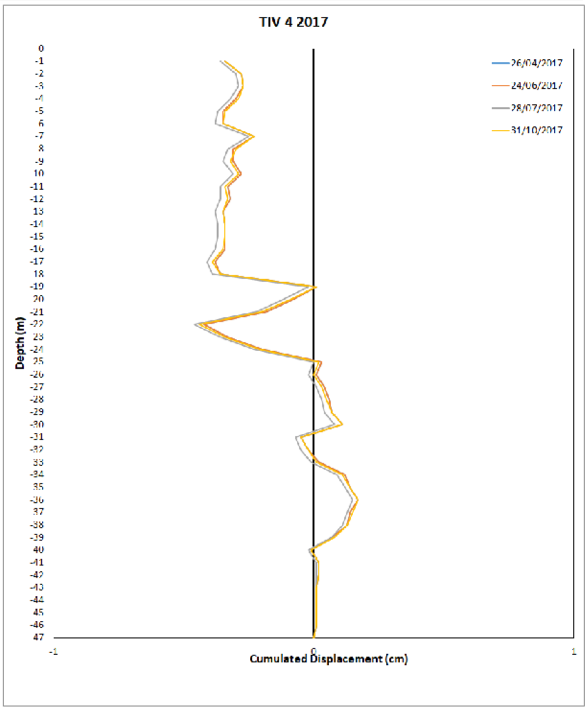
TIV 4 2017
26/04/2017
24/06/2017
28/07/2017
31/10/2017
Depth (m)
-1
0
1
Cumulated Displacement (cm)

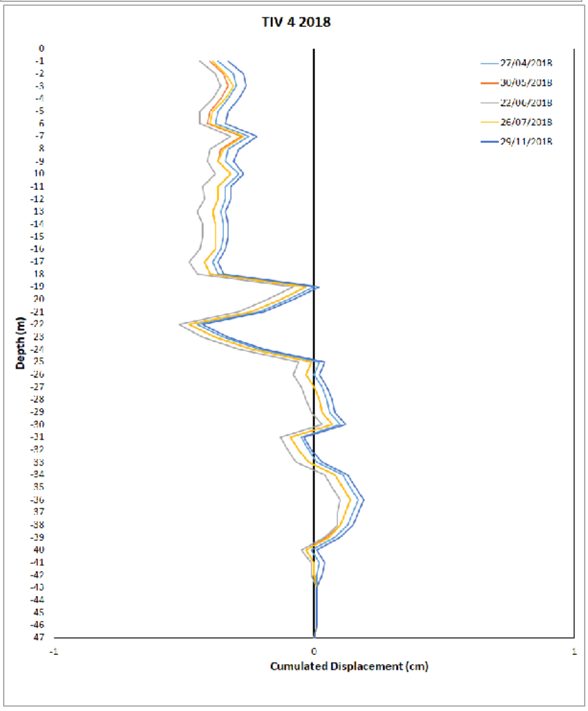
TIV 4 2018
27/04/2018
30/05/2018
22/06/2018
26/07/2018
29/11/2018
Depth (m)
-1
0
1
Cumulated Displacement (cm)

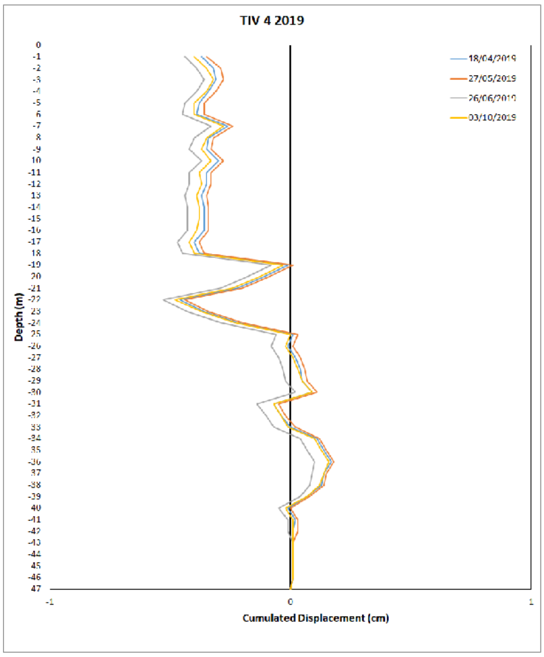
TIV 4 2019
18/04/2019
27/05/2019
26/06/2019
03/10/2019
Depth (m)
Cumulated Displacement (cm)

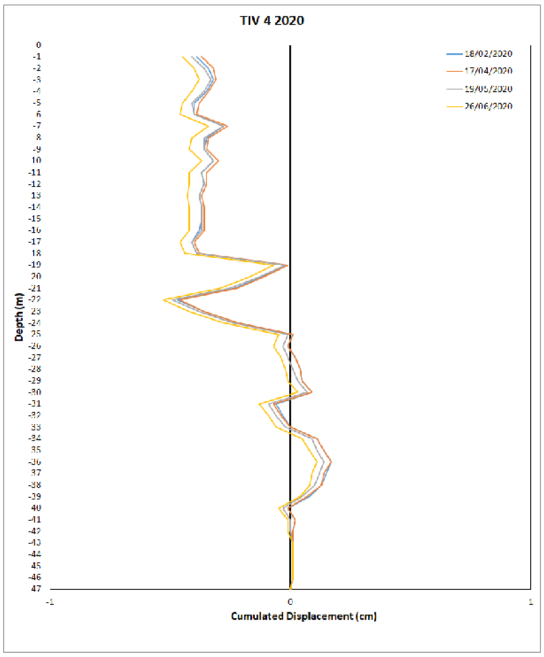
TIV 4 2020
18/02/2020
17/04/2020
19/05/2020
26/06/2020
Depth (m)
Cumulated Displacement (cm)

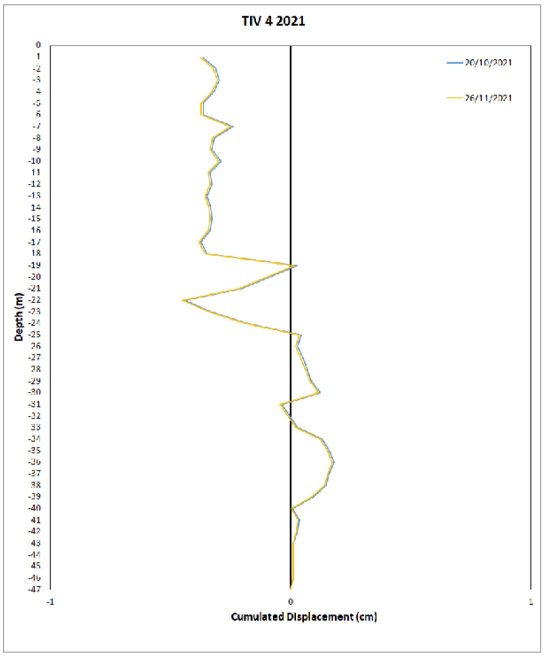
TIV 4 2021
20/10/2021
26/11/2021
Depth (m)
Cumulated Displacement (cm)

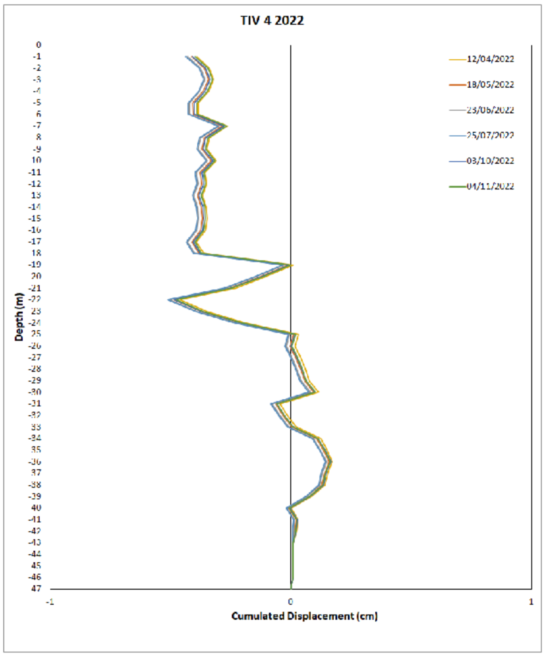
TIV 4 2022
12/04/2022
18/05/2022
23/06/2022
25/07/2022
03/10/2022
04/11/2022
Depth (m)
Cumulated Displacement (cm)

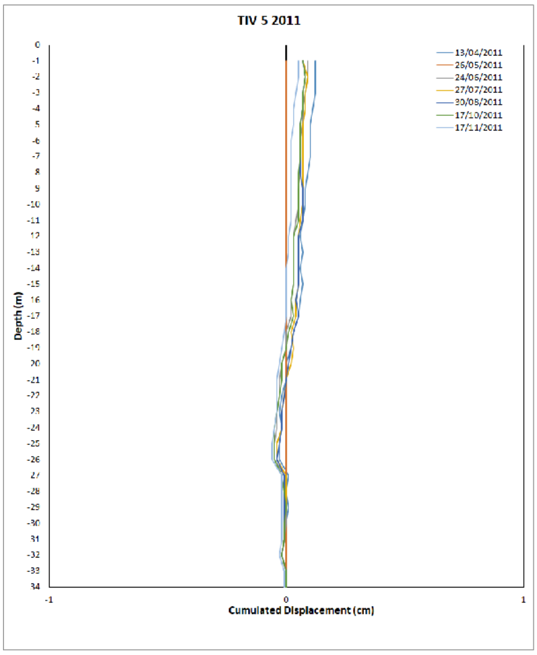
TIV 5 2011
13/04/2011
26/05/2011
24/06/2011
27/07/2011
30/08/2011
17/10/2011
17/11/2011
Depth (m)
Cumulated Displacement (cm)

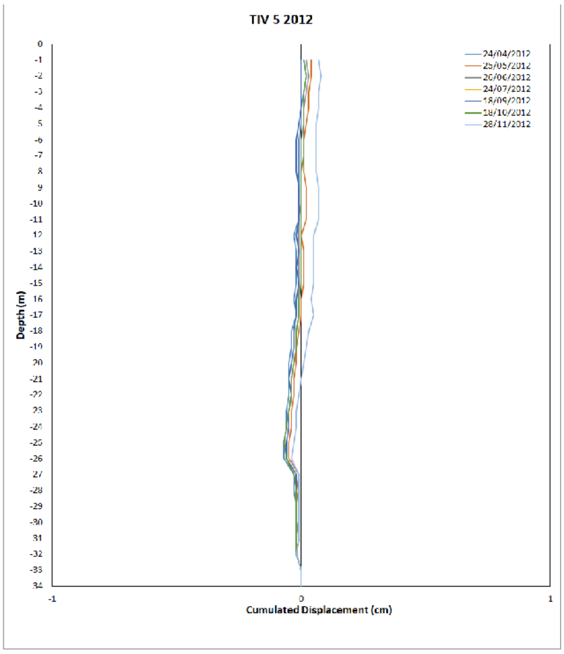
TIV 5 2012
24/04/2012
25/05/2012
20/06/2012
24/07/2012
18/09/2012
18/10/2012
28/11/2012
Depth (m)
Cumulated Displacement (cm)

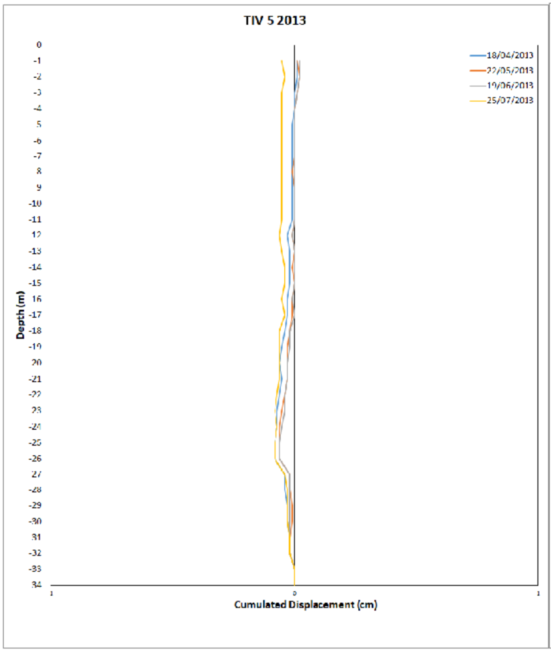
TIV 5 2013
18/04/2013
22/05/2013
19/06/2013
25/07/2013
Depth (m)
Cumulated Displacement (cm)

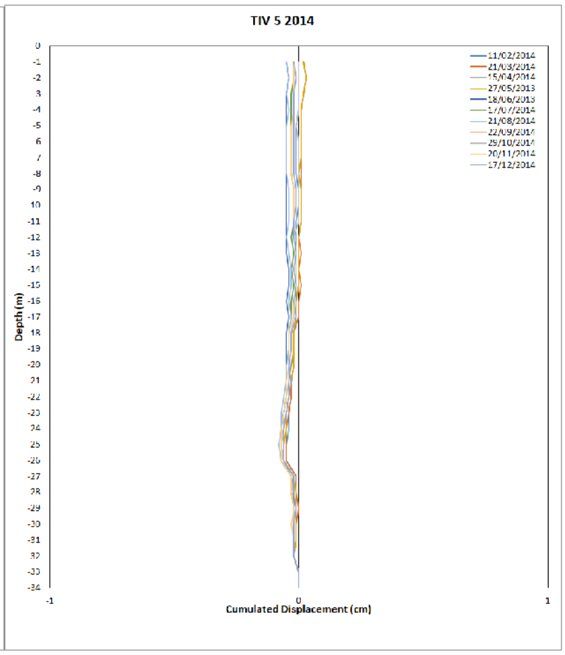
TIV 5 2014
11/02/2014
21/03/2014
15/04/2014
27/05/2013
18/06/2013
17/07/2014
21/08/2014
22/09/2014
29/10/2014
20/11/2014
17/12/2014
Depth (m)
Cumulated Displacement (cm)

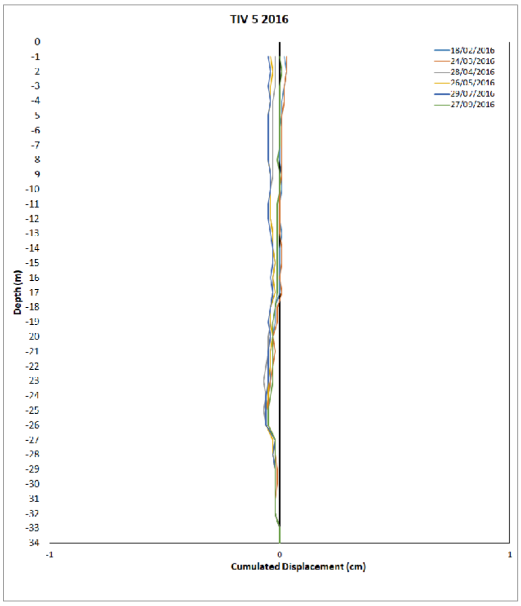
TIV 5 2016
18/02/2016
28/04/2016
26/05/2016
29/07/2016
Depth (m)
Cumulated Displacement (cm)

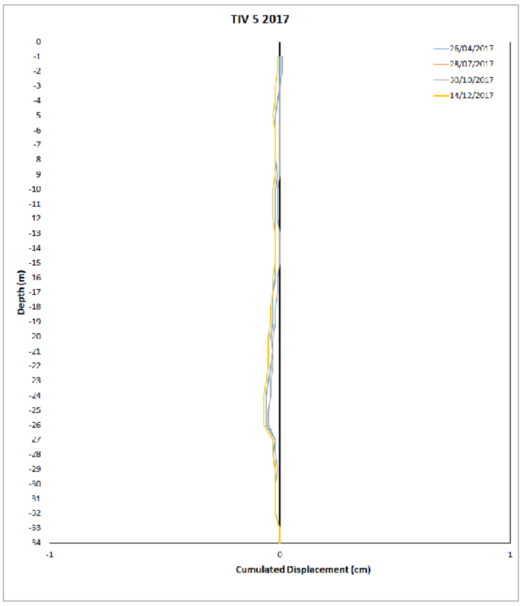
TIV 5 2017
26/04/2017
28/07/2017
30/10/2017
14/12/2017
Depth (m)
Cumulated Displacement (cm)

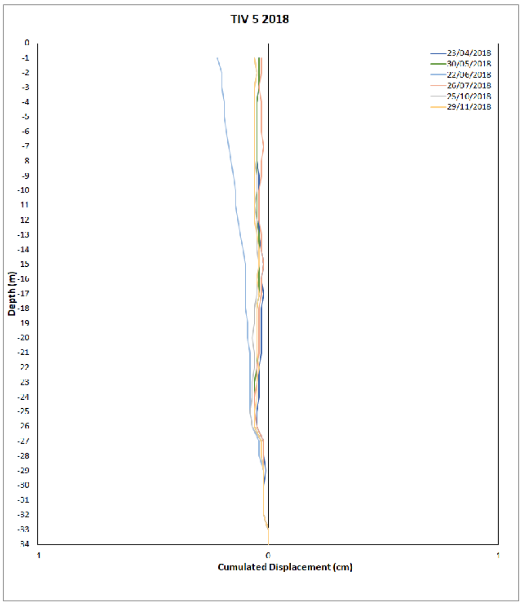
TIV 5 2018
23/04/2018
30/05/2018
22/06/2018
26/07/2018
25/10/2018
29/11/2018
Depth (m)
Cumulated Displacement (cm)

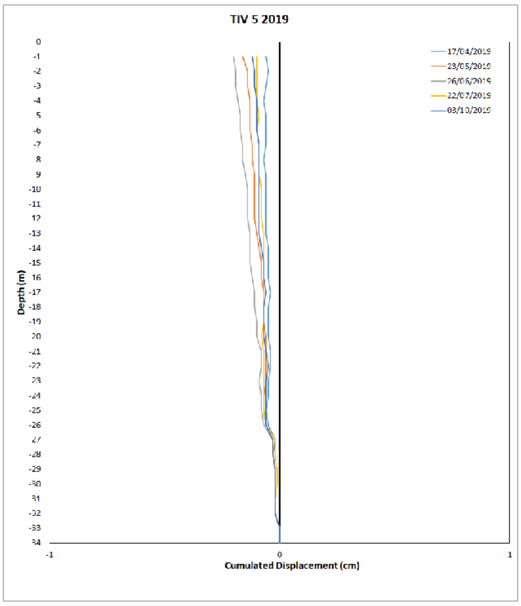
TIV 5 2019
17/04/2019
23/05/2019
26/06/2019
22/07/2019
03/10/2019
Depth (m)
Cumulated Displacement (cm)

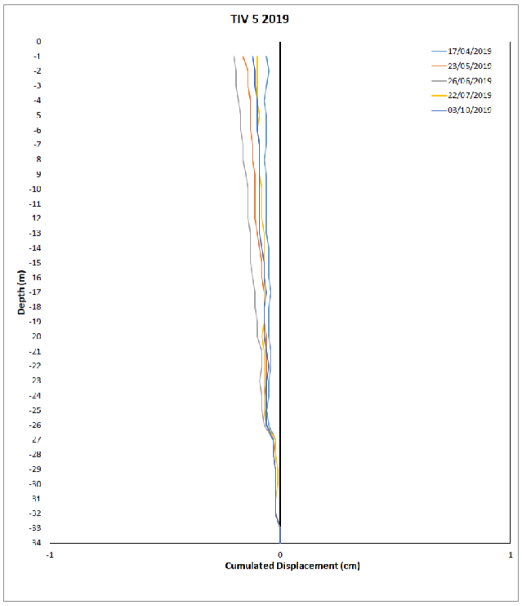
TIV 5 2019
Depth (m)
0 -1 -2 -3 -4 -5 -6 -7 -8 -9 -10 -11 -12 -13 -14 -15 -16 -17 -18 -19 -20 -21 -22 -23 -24 -25 -26 -27 -28 -29 -30 -31 -32 -33 -34
-1 0 1
Cumulated Displacement (cm)
17/04/2019
23/05/2019
26/06/2019
22/07/2019
03/10/2019

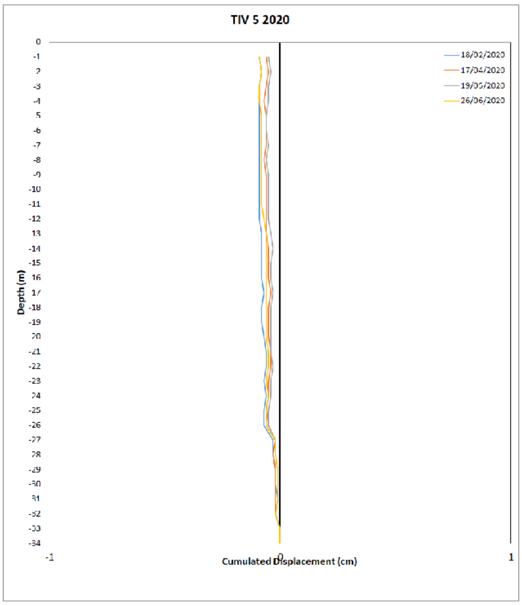
TIV 5 2020
Depth (m)
0 -1 -2 -3 -4 -5 -6 -7 -8 -9 -10 -11 -12 -13 -14 -15 -16 -17 -18 -19 -20 -21 -22 -23 -24 -25 -26 -27 -28 -29 -30 -31 -32 -33 -34
-1 0 1
Cumulated Displacement (cm)
18/02/2020
17/04/2020
19/05/2020
26/06/2020

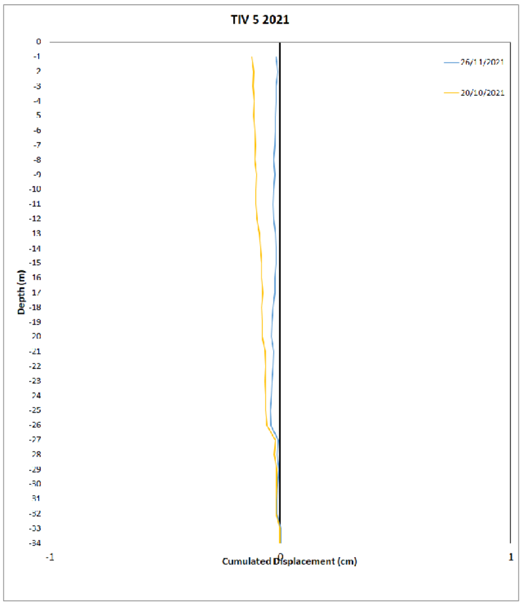
TIV 5 2021
Depth (m)
0 -1 -2 -3 -4 -5 -6 -7 -8 -9 -10 -11 -12 -13 -14 -15 -16 -17 -18 -19 -20 -21 -22 -23 -24 -25 -26 -27 -28 -29 -30 -31 -32 -33 -34
-1 0 1
Cumulated Displacement (cm)
26/11/2021
20/10/2021

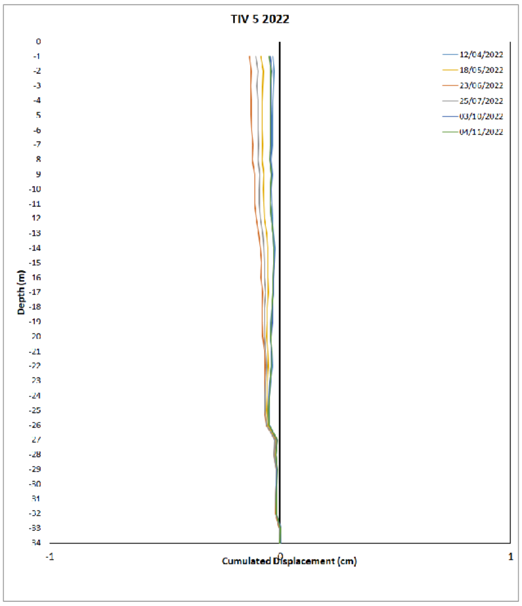
TIV 5 2022
Depth (m)
0 -1 -2 -3 -4 -5 -6 -7 -8 -9 -10 -11 -12 -13 -14 -15 -16 -17 -18 -19 -20 -21 -22 -23 -24 -25 -26 -27 -28 -29 -30 -31 -32 -33 -34
-1 0 1
Cumulated Displacement (cm)
12/04/2022
18/05/2022
23/06/2022
25/07/2022
03/10/2022
04/11/2022